HARMONIA
International network for harmonization of atmospheric aerosol retrievals from ground based photometers

HARMONIA CA21119

Deliverable 2.2

List of possible improvements on the quality of solar, lunar and stellar photometry

WG2 leaders: M. Campanelli, V. Estellés

Contributors: (By alphabetical order) Y. Aslanoglu, A. Barreto, M. Garcia-Suñer, P. González-Sicilia, P. Hrabčák, A. Karanikolas, S. Kazadzis, G. Kumar, S. Logothetis, F. Marenco, A. Masoom, V. Matos, D. Meloni, A. Papetta, S. Pulimeno, I. Steinberga, S. Zero

Date *9 November* 2024

COST EUROPEAN COOPERATION IN SCIENCE & TECHNOLOGY

Funded by the European Union

Introduction

According to the sixth Assessment Report (AR6) of Intergovernmental Panel on Climate Change, the observed human- caused earth system warming is dominated by the increasing atmospheric concentration of greenhouse gases, such as carbon dioxide (CO2) and methane (CH*4*), but it's partly masked by the aerosol cooling effect, whose quantification still represents one of the major challenges faced by the scientific community. Additionally, it has been proven that fine aerosol and particulate matter (PM) has serious implications on human health and can be assumed as a proxy indicator for air pollution. It is therefore essential to provide an accurate aerosol characterization to the scientific community, mostly focusing on the optical properties affecting absorption and scattering of the sunlight.

Aerosol Optical Depth (AOD), Single Scattering Albedo (SSA), refractive index and size distributions are the most important columnar optical properties typically used to describe the aerosol absorption and scattering capabilities and the size properties. They can be retrieved from sun and sky radiation measurements performed by international photometers networks (such as AERONET, SKYNET, and GAW-PFR) and radiative transfer modelling.

The main target of the HARMONIA COST action is to work on the homogenization and harmonization of the different international networks, the improvement of the techniques they rely on, and the synergy with other complementary techniques. The Working Group 2 of the HARMONIA COST action is specifically devoted to the improvement of aerosol products. The particular objective of the Deliverable 2.2 is to present a summary of proposals towards the improvement of the quality of solar, lunar and stellar photometers, and their relation with other instrumental and analysis techniques.

The report is structured as follows: section 1 focuses on the proposals of improvement of the solar based techniques, including the standard instruments of the AERONET, SKYNET and GAW-PFR networks, and the related data processing. Section 2 is devoted to the improvement and exploitation of lunar and stellar based techniques. Section 3 analyses the synergy with airborne techniques. Section 4 deals with the harmonization of low cost techniques and standard networks. Finally, section 5 presents different long term analysis of aerosol and radiation characteristics obtained with different instrumentation in different sites.

1. Improvements on the solar based techniques

1.1 The Cimel CE318 sunphotometer

Based on: "Assessing Sun-Photometer Performance: Insights from an Intercomparison Campaign in Valladolid, Spain" presented at the European Meteorological Society Annual Meeting, Barcelona 8-12

September 2024. Authors: Simone Pulimeno, Mauro Mazzola, Angelo Lupi, Vito Vitale, Carlos Toledano, Ramiro González, Natalia Kouremeti, and Stelios Kazadzis.

During May 2024, a photometer PREDE-POM02 was deployed on the roof of the Science Faculty building at the University of Valladolid for an inter-comparison campaign. The instrument was set up alongside a CIMEL CE318 and a PFR. However, weather conditions were unfavorable, with persistent cloud cover and below-average temperatures, delaying clear sky observations until May 24. The initial setup used a NUC PC and the Skyradiometer2013Pro software for data acquisition. However, the raw signals appeared unusual in magnitude, particularly due to cloud cover. Suspecting an issue with the acquisition system, a second system with a Lattepanda PC running Windows XP and an older version of the software (Skyradiometer_v4.11) was used. Still, it was unclear if the problem stemmed from the software or mechanical issues in the instrument, as clear sky observations were not possible until later in the month.

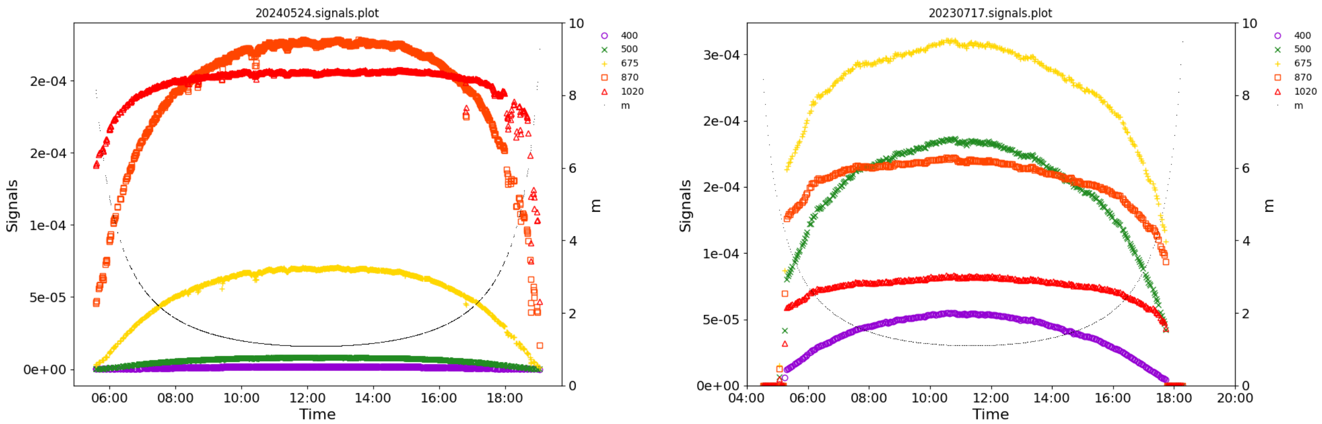

Figure 1.1.1. Raw signals (in mA) measured by PREDE POM02 at 5 Wavelengths. The left panel shows signals at Valladolid on May 24th, 2024; the right panel shows signals recorded at Bologna (Italy) during a field campaign on July 17th, 2023. Black box labeled as *m* represents the air mass.

On May 24, the first clear sky day, raw signals from the photometer were compared to similar data from Bologna in 2023 (Fig. 1.1.1). While differences were expected due to geographical factors, the 400, 500, and 675 nm channels showed significant signal loss, raising concerns about potential filter degradation. Channels at 870 and 1020 nm appeared more consistent with 2023 data. A log scale analysis confirmed that despite the signal loss, the channels still exhibited the typical bell-shaped irradiance curves when pointing at the Sun.

wl (nm)	Bol_23	Val_24	Val_corr_24
400	1.40e-04	4.1601075e-6	1.00e-04
500	3.58e-04	1.521544e-5	2.47e-04
675	4.32e-04	1.18048e-4	3.37e-04
870	2.80e-04	3.01672e-4	1.55e-04

cost EUROPEAN COOPERATION IN SCIENCE & TECHNOLOGY
Funded by the European Union

1020	1.99e-04	2.271926e-4	7.83e-03

Table 1.1.1 Calibration coefficients retrieved by applying the Langley method for the 2023 campaign in Bologna (Bol_23), the Valladolid campaign using raw signals (Val_24), and the Valladolid campaign with amplification applied to all wavelengths (Val_corr_2024).

Using the Langley method, calibration coefficients (V0) were calculated for the Valladolid data and compared to the Bologna 2023 values (see Table 1.1.1). Significant differences were observed in the 400, 500, and 675 nm channels, suggesting possible degradation. Correction factors were applied to adjust the irradiances, bringing the signals closer to expected values. After applying these corrections, recalculated calibration coefficients aligned better with those from the 2023 campaign. By using these corrected V0 values, we tried to understand if AOD can still be calculated from the raw irradiances, despite the signal degradation. Fig. 1.1.2 shows that the AOD values measured from the raw signals of the PREDE (and using the same signals to determine the calibration constants through the Langley method) are about six times higher than those calculated by AERONET (CIMEL instrument). Due to the significant degradation of the filter, it was not possible to obtain high-quality AOD retrievals from the raw irradiance signals acquired by the PREDE POM02.

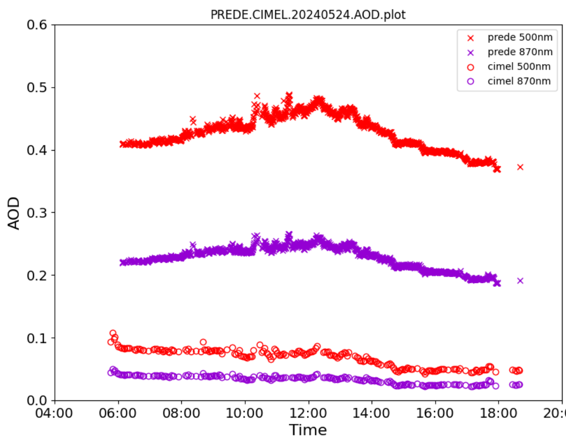

Figure 1.1.2. AOD retrieved at Valladolid the 24th of May 2024 at two different wavelengths (500 and 870 nm) from PREDE and CIMEL.

1.2 The Prede POM radiometer

Based on: "Upgrade and assessment of the on-site calibration methods used in SKYNET" presented at the European Meteorological Society Annual Meeting, Barcelona 8-12 September 2024. Authors: Gaurav Kumar, Masahiro Momoi, Monica Campanelli, Victor Estellés, and Meritxell Garcia.

The on-site calibration method with PREDE POM radiometers is widely used in the SKYNET network. This methodology, also known as the Improved Langley Plot (ILP), was first developed by Nakajima et al. in 1996 and Campanelli et al. in 2004. The PREDE POM radiometers are calibrated on the site without being sent to a high-altitude site to be calibrated using the standard Langley method. The advantage of this methodology over the standard Langley is its flexibility in working in relatively turbid atmospheres.

The basic idea of this methodology is to use the almucantar data collected using the PREDE POM instrument between the scattering angle of 3 to 30 degrees. Later, we use this data to invert them to retrieve volume size distribution. Once we retrieve the volume size distribution, we retrieve SSA with the help of Mie scattering coefficients. Finally, we find scattering AOD, and we see the fit of its logarithm against τ_{sct}/μ (μ is the cosine of zenith angle and τ_{sct} is the scattering optical depth of the AOD($\tau_{sct}=\tau_{ext}$ * Single scattering albedo of the aerosol)). In the last step, we perform a series of screening criteria to select the best days. After this, we find the monthly mean of the selected calibration values of the selected days. This method has worked nicely and has provided good results. But recent research has shown a seasonality while using POM-02. Uchiyama et al. 2018 first discussed this seasonality in their paper. They found that there was a systematic difference of up to 4% in the ILP calibration and the interpolated calibration transfer value. They found this difference after the temperature correction of the signal. Finally, they attributed this to the incorrect assumption of the refractive index. They used a different assumption to get the ILP (1.5 + i0.001).

This study investigates the sensitivity of the refractive indices whose values are assumed to retrieve the parameters. It attempts to address the inability to use a precise refractive index value, which can be indicative of the aerosol at the selected site.

The default values used in Skyrad4.2 are m+in=1.5+i0.005, and A=0.1, where m is real refractive index, n is the imaginary refractive index, A is ground albedo, and $\mu=\cos\theta$.

We chose m and n to do the sensitivity test. Ground albedo does not change as frequently, so we omitted it and left it as the default value in our test. However, we still tested Aosta to check for the effect of using the different ground albedo in other months. We chose the site because it is situated between hills at an altitude of 560 m and receives snowfall during winter. We hope this can change the ground albedo, and it could affect the radiative budget calculated by forward modelling in Skyrad4.2.

Table 1.2.1- Monthly averaged TROPOMI ground albedo for Aosta.

340	380	400	500	675	870	1020	
0.0918	0.0717	0.0603	0.0450	0.0617	0.1604	0.1406	Jan
0.0796	0.0625	0.0528	0.0414	0.0590	0.1712	0.1486	Feb
0.0682	0.0539	0.0457	0.0380	0.0565	0.1813	0.1560	Mar

COST EUROPEAN COOPERATION IN SCIENCE & TECHNOLOGY
Funded by the European Union

0.0560	0.0447	0.0382	0.0344	0.0538	0.1920	0.1637	Apr
0.0442	0.0358	0.0309	0.0309	0.0511	0.2023	0.1712	May
0.0320	0.0266	0.0234	0.0272	0.0483	0.2129	0.1788	Jun
0.0202	0.0177	0.0161	0.0237	0.0456	0.2231	0.1860	Jul
0.0164	0.0141	0.0132	0.0220	0.0422	0.2100	0.1767	Aug
0.0729	0.0577	0.0509	0.0419	0.0528	0.2026	0.1706	Sept
0.0893	0.0685	0.0593	0.0473	0.0609	0.1917	0.1626	Oct
0.1159	0.0899	0.0751	0.0522	0.0666	0.1388	0.1244	Nov
0.1040	0.0809	0.0678	0.0486	0.0642	0.1495	0.1324	Dec

Table 1.2.1. shows that the Ground Albedo has shown variation over different months. The standard deviation of the ground albedo varies from as high as 0.03 for 340 nm to as low as 0.007 for 675 nm.

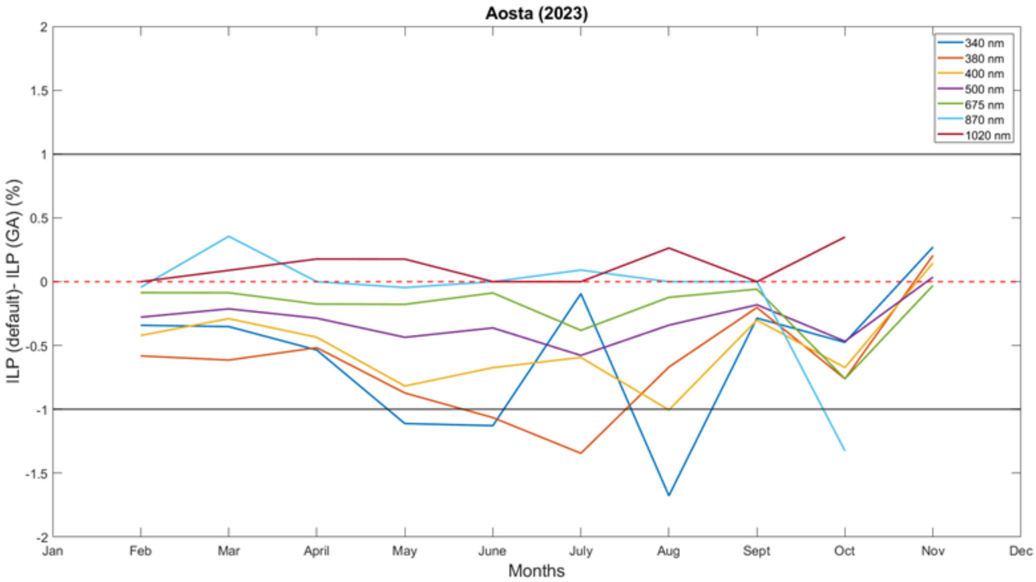

Figure 1.2.1.- Difference of calibration (in %) between default configuration and calculated using varying monthly mean ground albedo obtained from TROPOMI.

Figure 1.2.1. shows that the difference between the default ILP and ILP calculated using varying ground albedo is close to 0 for 870 and 1020 nm. For wavelengths 400 and 500 nm, the difference is within -0.5%. Only for 340 and 380 nm channels does the difference seem to have been > 1% for a few months.

Considering the tiny difference, we only did the sensitivity test for the refractive index.

Sensitivity test for refractive index

To choose the values of m and n, we used the values included in the kernel file from Skyrad4.2 version. Following are the values present in the Kernel file:
m= 1.35, 1.375, 1.4, 1.425, 1.45, 1.475, 1.5, 1.525, 1.55, 1.575, 1.6, 1.625, 1.65
n= 0.00, 1.00e-03, 2.00e-03, 3.00e-03, 5.00e-03, 1.00e-02, 2.00e-02, 3.00e-02, 5.00e-02
We run Skyrad4.2 systematically, choosing one value of m and running for all the values of n. For every m value, we have nine different calibrations (corresponding to nine different values of n) outputs. Thus, we get 117 different monthly calibration values for each set of assumed values of m and n. In the next step, we find the standard deviation of the monthly calibration values and calculate the error using the following expression.

$$U = \frac{F_{0std}}{F_{0mean}} \times 100$$

F_{0std} is the standard deviation of monthly calibration value, and F_{0mean} is the mean of monthly calibration value.

Sites and data

In the present study, we used data from the OUATRAM3 and Izana campaigns. We also used data from two permanent sites, Valencia and Aosta, for nine (October 2022 - June 2023) and eleven months (February 2023 - November 2023), respectively.

Results

Table 1.2.2.-Error estimation (in %) at Izana and Rome during Izana and QUATRAM3 (Q3) Campaign

340	**400**	**500**	**675**	**870**	**1020**	**Site**	**Duration of data**
0.221	0.110	0.074	0.055	0.069	0.269	Izana	Sep-22
0.709	0.466	0.324	0.120	0.094	0.123	CNR(Q3)	Sep-21
0.674	0.489	0.335	0.261	0.177	0.267	UV(Q3)	Sep-21

Table 1.2.3.-Error estimation (in %) at Aosta

340	**400**	**500**	**675**	**870**	**1020**		Aosta
0.777	0.651	0.412	0.266	0.212	0.140	February 2023	
0.816	0.588	0.280	0.177	0.253	0.173	March 2023	
0.368	0.219	0.129	0.047	0.066	0.259	April 2023	
1.343	1.069	0.745	0.402	0.213	0.171	May 2023	
1.301	0.506	0.280	0.241	0.187	0.372	June 2023	
0.405	0.243	0.178	0.114	0.102	0.079	July 2023	

0.772	1.077	1.434	1.512	0.591	0.951	August 2023	
0.451	0.312	0.275	0.300	0.236	0.193	September 2023	
0.861	0.654	0.719	0.707	0.695	0.504	October 2023	
0.422	0.234	0.142	0.130	-	-	November 2023	

Table 1.2.4.- Error (in %) estimation at Valencia

340	**400**	**500**	**675**	**870**	**1020**		
1.752	1.258	0.719	0.531	0.409	0.550	October 2022	Valencia
0.551	0.536	0.530	0.358	0.280	0.567	November 2022	
3.188	3.220	1.098	0.482	0.465	0.592	December 2022	
1.109	0.739	0.472	0.262	0.259	0.222	January 2023	
0.997	0.497	0.207	0.129	0.178	0.324	February 2023	
0.621	0.509	0.340	0.266	0.225	0.214	March 2023	
0.585	0.325	0.200	0.182	0.193	0.178	April 2023	

0.655	0.474	0.240	0.231	0.193	0.199	May 2023	
1.034	0.451	0.270	0.235	0.201	0.249	June 2023	

The above tables show the monthly errors associated with 117 calibration values obtained using 13 real and 9 imaginary refractive indices taken from the kernel file. This shows the variation of calibration value due to the choice of refractive index. The refractive index shows aerosol absorption and scattering properties. Ideally, this choice should not affect our retrieval much because we iterate until convergence. However, we realise that it is practically impossible to do this. An alternative approach is to calculate the error due to this assumption.

In Table 1.2.2., we see that the errors in Izana are small, while during the QUATRAM3 campaign, the errors are higher except for 1020 nm. This reflects that the airmass in Izana was relatively stable and did not show much variation. This is the reason the choice of assumption was almost insignificant. On the other hand, we have higher errors in the QUATRAM3 campaign and Valencia and Aosta. In the case of Valencia and Aosta, we see different errors during different months, going up to 1.75 and 1.4 % in Valencia and Aosta. Certain months showed peculiar values, such as December in Valencia and August in Aosta.

The results indicate that when we apply the ILP method in turbid sites, adding this error as a source of uncertainty is essential. We have seen some strange results in Valencia and Aosta in recent months. We are investigating the source of this peculiar behaviour. As a part of this study, we also plan to add more sites to the analysis in future.

References:

Campanelli, M., Nakajima, T., and Olivieri, B. "Determination of the solar calibration constant for a sun-sky radiometer: proposal of an in-situ procedure," Appl. Opt. 43, 651-659 (2004)

Uchiyama, A., Matsunaga, T., and Yamazaki, A.: The instrument constant of sky radiometers (POM-02) – Part 1: Calibration constant, Atmos. Meas. Tech., 11, 5363–5388, https://doi.org/10.5194/amt-11-5363-2018, 2018.

Nakajima, T., Tonna, G., Rao, R., Boi, P., Kaufman, Y., and Holben, B., "Use of sky brightness measurements from ground for remote sensing of particulate polydispersions," Appl. Opt. 35, 2672-2686 (1996)

1.4 Towards the harmonization of calibration techniques

Based on: "Harmonizing solar photometry calibration methods: A Cross-Network Calibration Study at Izaña Observatory" presented at the European Meteorological Society Annual Meeting, Barcelona 8-12 September

2024. Authors: Pablo González-Sicilia, Monica Campanelli, Víctor Estellés, África Barreto, Lionel Doppler, A. Fernando Almansa, Óscar Álvarez-Losada, Gaurav Kumar, and Rosa D. García.

Aerosol Optical Depth (AOD) is recognized by the World Meteorological Organization's Global Atmosphere Watch (WMO-GAW) as a key metric for understanding the role of atmospheric aerosols in Earth's radiative forcing. In response, several networks of ground-based sun photometers have been established over the years, with the most prominent being the AErosols RObotic NETwork (AERONET), the Sky Measurements Network (SKYNET), and the Global Atmosphere Watch's Precision Filter Radiometer (PFR). These networks, while sharing the common goal of measuring AOD, use different instruments, calibration techniques, and data retrieval methods, leading to variations in their AOD measurements. These differences highlight the need for thorough cross-network comparisons and harmonization efforts to ensure the integration of AOD data for global aerosol studies. This work leverages simultaneous measurements from May to November 2020 at the Izaña Observatory (Tenerife, Canary Islands, Spain), using a Prede-POM1 unit from the SKYNET network and a CIMEL CE318-T master instrument from the AERONET network. The observatory's high-altitude location (2,373 m above sea level) in the free troposphere provides ideal conditions for applying the Standard Langley Plot (SLP) calibration method (Shaw, 1983), which reduces atmospheric interference and significantly enhances the accuracy of solar and atmospheric measurements. First, an adaptation of the methodology described by Toledano et al., (2018) is presented to apply the Standard Langley Plot (SLP) calibration to the Prede-POM1 unit. The resulting calibration constants are used to calculate the Total Optical Depth (TOD), which is subsequently corrected for non-aerosol contributions to isolate the AOD. Finally, both the AOD values derived from the Standard Langley Plot (SLP) calibration and those obtained from SKYNET using the Improved Langley Plot (ILP) method (Campanelli et al., 2023) are compared to AERONET's AOD data (Giles et al., 2019), to evaluate the consistency and accuracy of the different calibration methods.

Standard Langley Plot Calibration:

To perform the Standard Langley Plot (SLP) calibration, a selection of suitable days was made by identifying cloud-free raw measurements using 1-minute collocated global and diffuse radiation measurements based on García et al. (2014). Measurements from the Prede POM1 unit were taken in the morning, focusing on optical air masses between 2 and 5. A mean AOD at 500 nm was calculated using AERONET data, and if the mean AOD was less than 0.025 and at least 10 valid points were available, a linear fit of the Beer-Lambert law ($I=I_0\exp(-m\tau)$) was applied to the data. Residuals greater than twice the RMSE were iteratively removed until the RMSE dropped below 0.2, or fewer than 10 points remained. A day was selected as suitable if the final RMSE was below 0.2, more than 33% of points remained, and the R^2 value exceeded 0.9. For each selected day, the fit was recalculated. If the RMSE exceeded 0.006, data points with residuals greater than twice the RMSE were iteratively removed until either fewer than 10 points remained or the RMSE dropped below 0.006. The calibration constant (F_0) was retained only if the RMSE was below 0.006, more than 33% of the data points remained, and the R^2 value exceeded 0.9. Finally, a manual selection of calibration periods was conducted by analyzing the ratios between the Prede POM1 and the AERONET master instrument at

Izaña. Groups of at least 10 days within a 30-day period were formed, and an automated method was applied to reduce the Coefficient of Variation (CV) for each period by iteratively removing outliers until either 10 calibration constants remained or the CV dropped below 0.5%.

Calibration Period	F0 500 nm [A]	CV 500 nm [%]	F0 675 nm [A]	CV 675 nm [%]	F0 870 nm [A]	CV 870 nm [%]	F0 1020 nm [A]	CV 1020 nm [%]
(1/5/2020, 21/5/2020)	2,75E-04	0,42	3,32E-04	0,33	2,22E-04	0,24	1,01E-04	0,40
(22/5/2020, 9/6/2020)	2,73E-04	0,43	3,30E-04	0,37	2,21E-04	0,37	1,00E-04	0,80
(18/6/2020, 29/6/2020)	2,63E-04	0,55	3,18E-04	0,54	2,12E-04	0,53	9,78E-05	1,06
(21/7/2020, 20/8/2020)	2,48E-04	0,59	3,01E-04	0,49	2,00E-04	0,54	9,31E-05	0,59
(30/9/2020, 19/10/2020)	2,35E-04	0,64	2,87E-04	0,47	1,91E-04	0,46	8,75E-05	0,89

Table 1.4.1: Mean calibration constants (F_0) with associated CV values obtained for each channel and each calibration period.

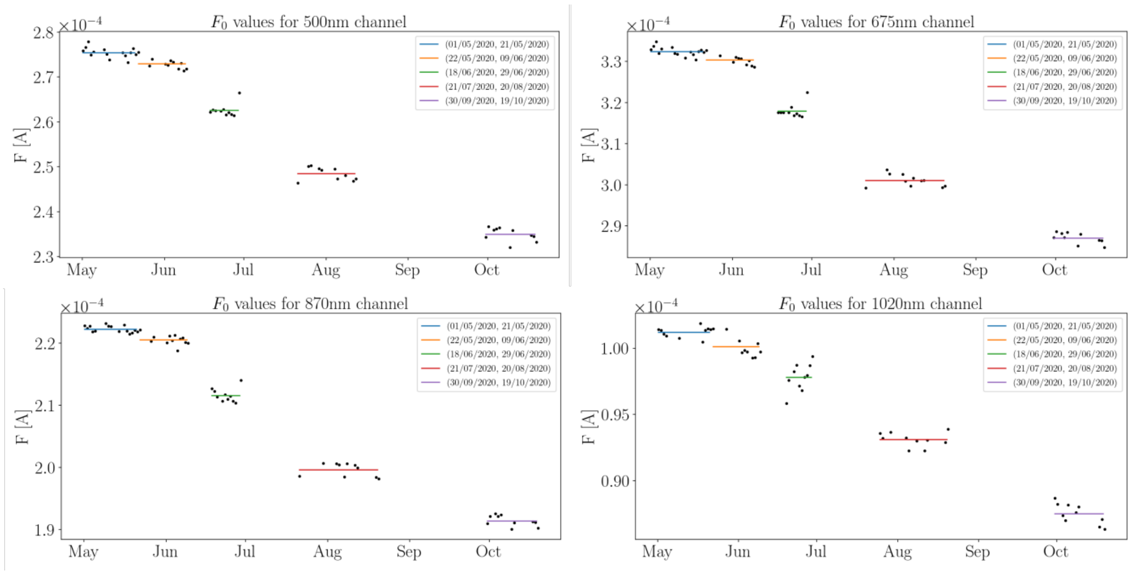

Figure 1.4.1: Mean calibration constants (F_0) with associated CV values obtained for each channel and each calibration period.

Using this approach, calibration constants were obtained for the 500, 675, 870, and 1020 nm channels over five selected periods (Table 1.4.1). For the 500, 675, and 870 nm channels, the calibration constants exhibited CV values below 0.7%, with a clear trend of decreasing CV from shorter to longer wavelengths. However, the 1020 nm channel was affected by temperature, and due to the absence of coincident temperature measurements, it was not possible to apply the necessary corrections. As a result, the CV values for this channel were relatively high and inconsistent across the different periods. Figure 1.4.1 presents the calibration constants determined for each day, as well as the mean value for each calibration period. Over the measurement period, the Prede POM1 signal decreased by approximately 25% across all channels, suggesting that dust accumulation on the lenses occurred during typical summer dust intrusions at Izaña.

AOD Comparison:

The AOD for all cloud-free data points was calculated at wavelengths of 500, 675, and 870 nm using the obtained calibration constants, following the same algorithms as in ESR.pack (Estellés et al., 2012). The 1020 nm channel was excluded due to calibration issues related to the lack of temperature characterization. To compare the AOD values from SKYNET using the SLP with those from AERONET, a daily 3-standard deviation filter was applied to both data sets. The comparison was performed with a joint tolerance of ±30 seconds. Traceability was evaluated according to WMO guidelines, which stipulate that 95% of the differences between AOD measurements must fall within ±(0.005 + 0.01/m), where 'm' denotes the optical airmass.

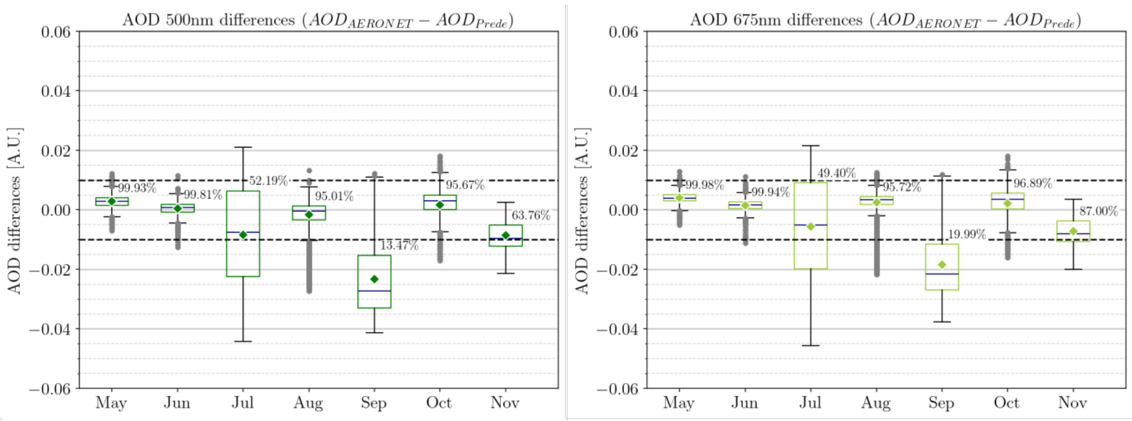

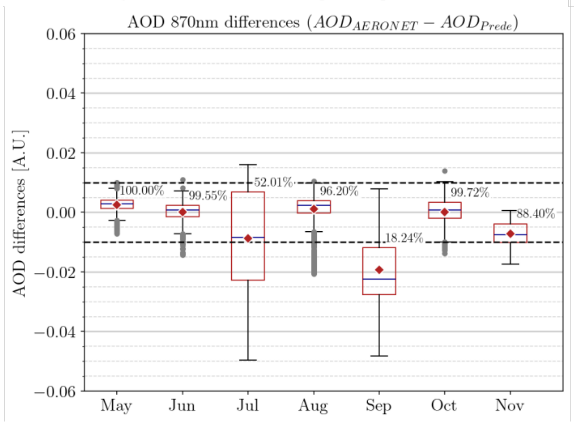

Figure 1.4.2: AOD differences between AERONET and Prede POM1 (AOD_AERONET - AOD_Prede) obtained through Standard Langley Plot method (SLP) for the 500, 675, and 870 nm channels. The rhombus represents the mean difference, and the blue line within each box indicates the median difference. The percentage next to each box shows the proportion of values within WMO limits, while gray circles denote outliers. The black dashed lines represent the ±0.01 limits.

Figure 1.4.2 shows the AOD differences between AERONET and the Standard Langley Plot (SLP) method for the 500, 675, and 870 nm channels. SLP AOD values generally align well with AERONET in May, June, August, and October, meeting WMO traceability criteria, but discrepancies arise in July and September due to signal changes in the Prede instrument, leading to overestimations. Figure 1.4.3 compares AOD differences between AERONET and SKYNET for the same channels. SKYNET data (available from June to November) show less consistent agreement, meeting WMO criteria only in selected months and channels. However, SKYNET's Improved Langley Plot calibration better accounted for instrument signal changes, leading to improved accuracy in July and September. When comparing AOD values, the Standard Langley Plot (SLP) method shows greater dispersion and more outliers, especially in July and September, and generally produces lower AOD values than AERONET. In contrast, SKYNET ILP method tends to yield higher AOD values compared to AERONET and shows less consistency with AERONET than the SLP method.

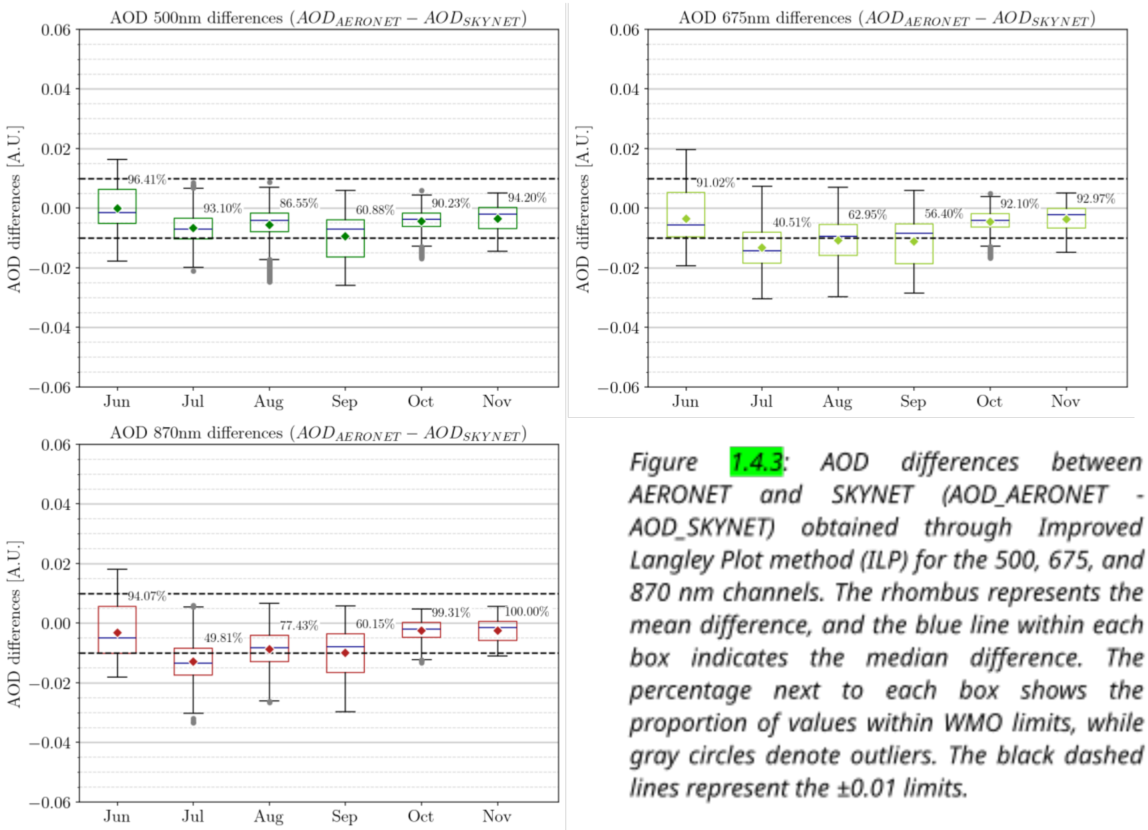

Figure 1.4.3: AOD differences between AERONET and SKYNET (AOD_AERONET - AOD_SKYNET) obtained through Improved Langley Plot method (ILP) for the 500, 675, and 870 nm channels. The rhombus represents the mean difference, and the blue line within each box indicates the median difference. The percentage next to each box shows the proportion of values within WMO limits, while gray circles denote outliers. The black dashed lines represent the ±0.01 limits.

References:

Campanelli, Monica, Victor Estelles, Gaurav Kumar, Teruyuki Nakajima, Masahiro Momoi, Julian Gröbner, Stelios Kazadzis, et al.: Evaluation of “on Site” Calibration Procedures for Sun-Sky Photometers.: Atmospheric Measurement Techniques Discussions, 15th of December 2023, 1-26. https://doi.org/10.5194/amt-2023-165, 2023.

Estellés, V., M. Campanelli, T. J. Smyth, M. P. Utrillas, y J. A. Martínez-Lozano.: Evaluation of the New ESR Network Software for the Retrieval of Direct Sun Products from CIMEL CE318 and PREDE POM01

Sun-Sky Radiometers.: Atmospheric Chemistry and Physics 12, n.º 23 5th of December 2012: 11619-30. https://doi.org/10.5194/acp-12-11619-2012, 2012.

García, R.D., O.E, García, E. Cuevas, V.E. Cachorro, P.M. Romero-Campos, R. Ramos and A.M. de Frutos.: Solar radiation measurements compared to simulations at the BSRN Izaña station. Mineral dust radiative forcing and efficiency study.: JGR-Atmospheres, Vol 119, 1-16, https://doi.org/10.1002/2013JD020301, 2014.

Giles, David M., Alexander Sinyuk, Mikhail G. Sorokin, Joel S. Schafer, Alexander Smirnov, Ilya Slutsker, Thomas F. Eck, et al.: Advancements in the Aerosol Robotic Network (AERONET) Version 3 Database – Automated near-Real-Time Quality Control Algorithm with Improved Cloud Screening for Sun Photometer Aerosol Optical Depth (AOD) Measurements.: Atmospheric Measurement Techniques 12, no. 1 (January 11, 2019): 169–209. https://doi.org/10.5194/amt-12-169-2019, 2019.

Toledano, Carlos, Ramiro González, David Fuertes, Emilio Cuevas, Thomas F. Eck, Stelios Kazadzis, Natalia Kouremeti, et al.: Assessment of Sun Photometer Langley Calibration at the High-Elevation Sites Mauna Loa and Izaña.: Atmospheric Chemistry and Physics 18, n.º 19 (11th of October 2018): 14555-67. https://doi.org/10.5194/acp-18-14555-2018, 2018.

Shaw, Glenn E.: Sun Photometry.: Bulletin of the American Meteorological Society 64, 1 (1983): 4-10, doi: https://doi.org/10.1175/1520-0477, 1983.

1.5 Application of Machine Learning and cloud computing

1.5.1. Machine Learning and Cloud Computing techniques applied to photometry

Based on the HARMONIA project #7: Machine Learning and Cloud Computing techniques applied to photometry. Authors: Iveta Steinberga, Akriti Masoon and Monica Campanelli.

Preliminary results. The study will be deepened in the third year of the COST action.

The use of machine learning algorithms in the classification of atmospheric aerosols, whether for determining potential climate impact or identifying the origin of potential aerosols, has seen a substantial increase in recent years. The variety of classification algorithms employed is extensive. However, a notable gap exists in the form of a lack of best practice recommendations for selecting the most suitable mode, depending on the nature of the data set or the objective pursued. The classification of aerosols in publications could be divided in 2 main parts: (1) a classification based on the composition of the particles and (2) a classification to determine the origin of the primary source of aerosols. And then, particle composition groups (e.g. coarse non-absorbing, black carbon high etc.) or pollution source groups are often identified depending on the target source (urban, biomass, desert etc.). In the form of a standardized approach, publications reveal 3-6 classifications of different particle compositions, while the number of pollution source classes in some cases reaches up to 20 classes. In general, about 20 publications have been analyzed.

For data analysis*,* measurements taken in Lampedusa (Italy) in the time period 1/1/2014-4/21/2020,were used. *From the AERONET sunphotometer, d*aily data *of the following* parameters *were* *considered*: AOD *at* different wavelengths, Angstrom Exponont (AE), Fine Mode Fract*ion (FMF) and the* chemical composition *from on* site *sampling*. Testing has been carried out for different classification algorithms (4 different approaches w*ere* analyzed*)* and also a mixed algorithms *scenario*, in order to avoid situations when classification couldn`t be performed or a lot of outliers detected. *Aerosol chemistry measurements were used for the validation of the results; the identification of sources has been performed based on aerosol chemical profiling.*

In addition to Lampedusa measurements, model testing has been carried out for AERONET-derived measurements in Rome (Italy), in the period 1/1/2019-12/31/2022, using the same parameters as for Lampedusa. Source apportionment classification was validated *using* data from the EU aerosol profiling database SPECIEUROPEhttps://source-apportionment.jrc.ec.europa.eu/Specieurope/index.aspx) and air quality monitoring data obtained within national monitoring network.

1.5.1.1 Results

The first classification method, *described in Annapurna et al. (2024) and* used for Lampedusa, was based on two parameters*:* AOD 550 nm *and* 440-870_Angstrom_Exponent*. This method* identified DESERT aerosols in around 3% of cases, MARINE in 24%, urban in 2%*. The other* cases could not be classified.

The result shows that *this* classification scheme is not robust.

Another method that is widely used is described in Stefan et al. (2020). The technique is similar to the above method and aerosols *are* classified according to their origin*:* MARINE, DUST, MIXED, URBAN/INDUSTRIAL, BIOMASS BURNING. Also in this method only two parameters (AOD 550 nm; Angstrom_Exponent-Total_500nm) are used as classification criteria. *The* results quite often were opposite (65% of cases) compared to the above method. For example, if Annapurna et al. (2024), classification result was MARINE, results *from* Stefan et al. 2020 was DUST/SAND.

A third method is described in Ozdemir et al. (2020), where AOD 550 nm and FineModeFraction_500nm *were used in the classification. Results provide* only three classes: MARINE, DESERT, and CONTINENTAL. Although the established classifier works well and there are no cases where classification is not possible, the result is too homogeneous. Almost 90% of the cases correspond to the MARINE class. A modified ver*sion of* Ozdemir et al. (2020) *uses* 5 classes: MARINE, DESERT, CONTINENTAL, BIOMASS BURNING and MIXED, with classifier criteria*:* AOD_870nm; Aod_440nm; *and* 440-870_Angstrom_Exponent. However for *L*ampedusa it was not possible to classify aerosol sources in at least 50% of the cases, indicating deficiencies in the method.

*G*round-level aerosol chemistry measurements and the SPECIEUROPE chemical profiles *provided that sea* aerosols are strongly prevalent in Lampedusa for the whole observation period based on sodium and sulfate ion proportions, while specific proportions of sulfates, calcium, aluminum, and iron pointed to Saharan dust dominance. Therefore an advanced aerosol classification algorithm was developed that considers the interdependence between photometric parameters (statistically relevant parameters have been identified) and chemical composition measurements with specific parameter limits. The algorithm developed includes the following parameters: AOD_500nm. 440-870_Angstrom_Exponent; Finemodefraction_500nm Extinction_angstrom_exponent_440-870 nm-Total; aerosol classes obtained — MARINE, VERY MARINE, DUST/DESERT, clear configurations/LOW AEROSOL, urban/INDUSTRIAL, BIOMASS, mixed.

Based on the established classification, the dataset uses a machine learning algorithm to train the classifier and use it for other datasets. The Random Forest algorithm was used in this case, and training was conducted in a JASP 0.18.3 environment (R-based). The learning accuracy of the resulting algorithms reaches 83.3%, a good enough indicator. A higher rate could be achieved by increasing the dataset. In addition, in test mode, the algorithm was also used for the Roman dataset. The data set used was more complete, less data gaps, and the resulting algorithm machine learning performance rate was significantly higher. The test accuracy, an impressive 96%, showcases the algorithm's robust performance.

Annapurna et al. (2024) https://doi.org/10.1016/j.asr.2023.09.068
Stefan et al. (2020) https://doi.org/10.1016/j.apr.2020.04.007
Ozdemir et al. (2020) https://doi.org/10.1016/j.apr.2020.06.008

1.5.2. Aerosol optical depth retrieval using ground-based solar irradiance measurements and machine learning

Based on: "Aerosol optical depth retrieval using ground-based solar irradiance measurements and machine learning" presented at the European Meteorological Society Annual Meeting, Barcelona 8-12 September 2024. Authors: Stavros-Andreas Logothetis, Vasileios Salamalikis, Georgios Kosmopoulos, and Andreas Kazantzidis.

1.5.2.1 Introduction

Reference instruments for measuring solar radiation face limitations in terms of fine temporal resolution and worldwide spatial coverage. Consequently, alternative techniques for solar resource assessment are under scrutiny, with a primary focus on radiative transfer modeling. An accurate assessment of solar resources necessitates a comprehensive understanding of aerosol properties. Integrating these properties into radiative transfer models enables the simulation of long-term solar irradiances under cloud-free conditions (Javadnia et al., 2017; Gueymard et al., 2018) as well as evaluating the aerosol radiative effects (García et al., 2012).

There are two primary methods for monitoring atmospheric aerosols. The first method involves the use of ground-based instruments, such as sun photometers (e.g., AERONET; Holben et al., 1998). The second method involves utilizing sensors aboard satellites (e.g., MODerate resolution Imaging Spectroradiometer, MODIS). In general, ground-based and satellite-based aerosol retrievals complement each other. Ground-based retrievals excel in accuracy and temporal resolution but face limitations in spatial coverage, particularly in desert areas, which are significant natural sources of suspended aerosol particles in the atmosphere. Considering the spatial and temporal constraints of both satellite and ground-based aerosol retrievals, other techniques have recently emerged, with a predominant focus on Aerosol Optical Depth (AOD).

Various alternative techniques for AOD retrieval reported in the literature fall into four primary categories: (1) backward solving radiative transfer or clear-sky models using solar radiation measurements (Salmon et al., 2021), (2) methodologies based on sunshine duration (SD) measurements (Sanchez-Romero et al.,2016), (3) image processing techniques using sky radiances from all-sky imagers (Logothetis et al., 2023), and (4) machine learning (ML) and deep learning algorithms employing various independent parameters as input features (Huttunen et al., 2016).

In this study, we proposed a machine learning methodology (referred to as “MLA-AOD” hereafter) to retrieve AOD for cloud-free conditions at the high temporal resolution of radiometric instruments. The MLA-AOD approach is evaluated using either pyrheliometer (DNI) or pyranometer (GHI) measurements, presenting different retrieval performances. The selection of the applied solar irradiance component relies on the instrument's availability. Even though AERONET sun photometers are established and measured every 5–15 min, it is very common for them to present gaps of hours, days, or weeks or to be inactive for years. This study proposes that the MLA-AOD methodology could be used (a) to fill the AOD gaps in the AERONET sites and (b) to expand the already existing temporal capabilities, regardless of the underlying climate and aerosol conditions.

1.5.2.2 Data

Aerosol optical properties, solar radiation, and total column water vapor data were acquired from AERONET, the Baseline Surface Radiation Network (BSRN), and Copernicus Atmosphere Monitoring Service Reanalysis (CAMSRA), respectively. AERONET’s Direct Sun Algorithm (DSA) derives AOD at seven wavelengths spanning from 340 nm to 1020 nm. DSA relies on spectral solar irradiance measurements directly on the solar disk, captured from the CIMEL Electronique CE318 multiwavelength sunphotometer. For subsequent analyses, cloud-screened AOD at 550 nm (AOD_{550nm}) rounded to the nearest minute are employed, meeting quality criteria established by pre-field and post-field calibrations (Level 2.0 data from Version 3; L2V3).

BSRN provides comprehensive data on the various components of incoming solar radiation, namely global horizontal irradiance (GHI), direct normal irradiance (DNI), and direct horizontal irradiance (DHI). The network delivers quality-assured measurements at a 1 min temporal resolution. Each BSRN radiometric station employs a first-class pyranometer and a pyrheliometer to measure GHI and DNI, respectively. The raw observations from BSRN undergo quality control (Yang et al., 2018) using the procedures outlined in the SolarData R package (Yang, 2019). For subsequent analysis, only the 1-minute quality-assured DNI and GHI measurements from BSRN are utilized.

CAMSRA represents the latest global dataset for atmospheric composition, created by the European Centre for Medium-Range Weather Forecasts (ECMWF). This dataset consists of 3-D9 time-consistent fields of atmospheric composition, incorporating aerosols and various chemical species (Innes et al., 2019). CAMSRA was generated through 4DVar data assimilation within CY42R1 of ECMWF’s Integrated Forecast System (IFS), in which meteorological modeling is incorporated. The 4DVar analysis applies IFS dynamics and physics to produce a sequence of atmospheric states that closely align with the available observations. CAMSRA data have been provided at approximately 80 km resolution and on a 3 h basis. In this study, TCWV retrievals are acquired.

1.5.2.3 Methodology

The proposed methodology (MLA-AOD) for retrieving AOD_{550nm} at 1 min resolution is illustrated in Figure 1.5.2.1, including primarily two steps: data acquisition and preprocessing. The raw data obtained from ground-based measurements are cloud-screened to isolate clear sky conditions. Although L2V3 AERONET retrievals are described as cloud-screened, the temporal merging of

AERONET and BSRN data may introduce cloud-contaminated cases, attributed to the smaller aperture of sun photometers compared to pyrheliometers.

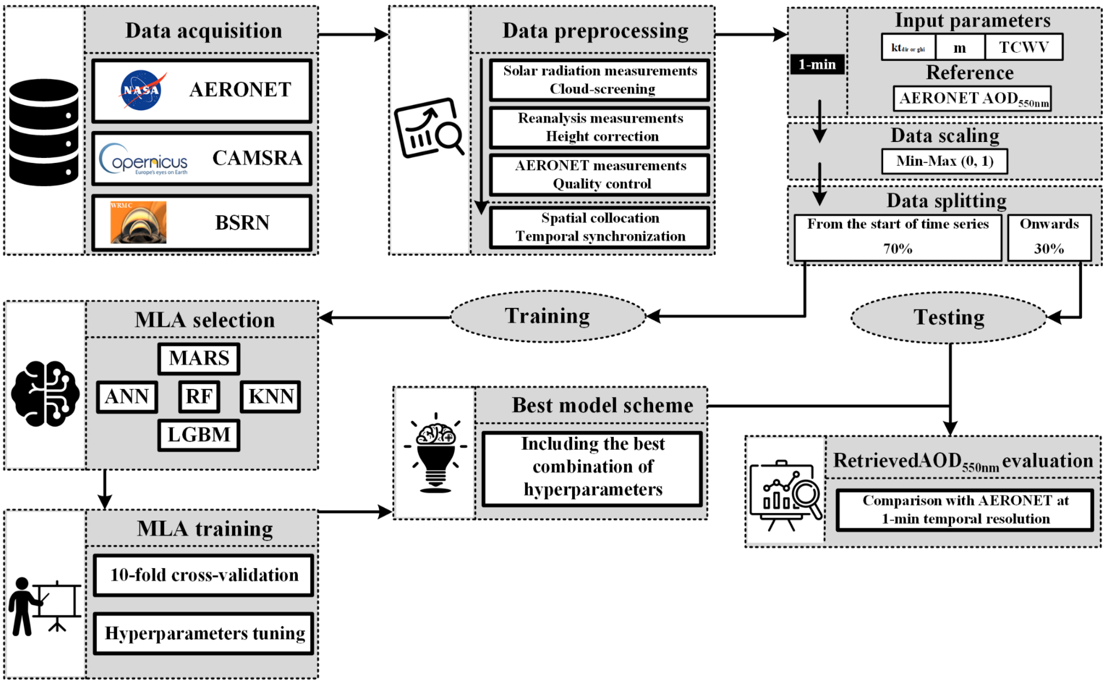

Figure 1.5.2.1. Flowchart of the MLA-AOD retrieval methodology.

To ensure clear-sky conditions, two distinct filters were applied—one for DNI and one for GHI. Concerning DNI, within one hour around each BSRN measurement, the standard deviation is calculated. If it is above 20% of the corresponding BSRN DNI measurement, the data point is detected as cloudy and removed. In addition, even though the sun's disk could be cloudless, the rest of the sky can contain sparse clouds that affect the GHI measurements. Therefore, to avoid possible cloud contamination, the Reno and Hansen clear-sky detection methodology (Reno and Hansen, 2016) is applied to the GHI measurements. The TCWV data are extracted at the ground-based stations through nearest-neighbour interpolation. Then, the 3-hourly TCWV is linearly interpolated at 1 min temporal resolution, aligning with the AERONET and BSRN datasets.

Subsequently, the preprocessed dataset is divided into two subsets, namely the training and testing datasets, which include four (three input and one output) parameters: 1) AOD_{550nm}, 2) global (kt_{glob}) and direct (kt_{dir}) clearness indexes, 3) TCWV, and 4) optical air mass (m). The splitting strategy follows a 70/30 approach without using a random-sampling approach. The first 70% of the time series represents the training set, and the remainder represents the test set. The independent (input) features undergo normalization between 0 and 1 using the Min-Max normalization method.

Five different ML algorithms (MLAs) were used, namely: Light Gradient Boosting Machine (LGBM: tree-based), Random Forest (RF: tree-based), Multivariate Adaptive Regression Splines (MARS: linear-based), K-Nearest Neighbors (KNN: distance-based), and Artificial Neural Network (ANN: linear-based). The MLA structure is determined through several internal parameters called hyperparameters. The optimal configuration for these hyperparameters for each MLA is determined through a randomized search procedure during training. The randomized search involves a 10-fold cross-validation process, with MSE serving as the fitness function. The “optimal” hyperparameter combination for each MLA is determined based on the minimum of total scores. The MLA-AOD methodology is applied for each collocated AERONET-BSRN station in Figure. 1.5.2.2. It is significant to evaluate the proposed methodology in diverse environments to assess its resilience to potential changes in climate and aerosol types.

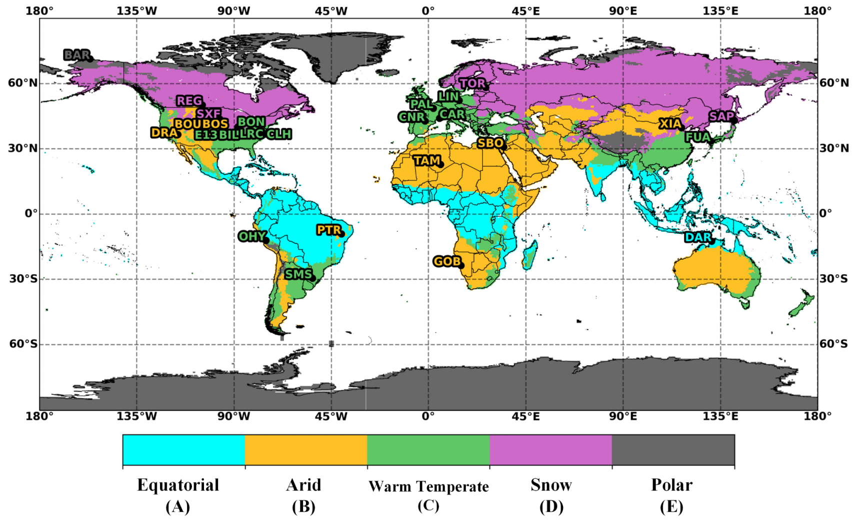

Figure 1.5.2.2. Spatial distribution of the AERONET-BSRN stations. The five different colours correspond to the five climate classes based on the Köppen-Geiger climate classification.

1.5.2.3 Results

Two distinct scenarios are examined: Scenario 1 considers the three input parameters, using Kt_{dir} as a solar irradiance component. Conversely, in Scenario 2, kt_{dir} is substituted by kt_{glob}. Figure 1.5.2.3 depicts the mean absolute error (MAE) and the relative MAE between scenarios 1 and 2, using solely the retrievals of the “optimal” MLA compared to AERONET measurements. More specifically, the “optimal” MLA is jointly assessed using the MAE, root mean square error (RMSE), and correlation coefficient (R), assuming an equal contribution for each statistical metric.

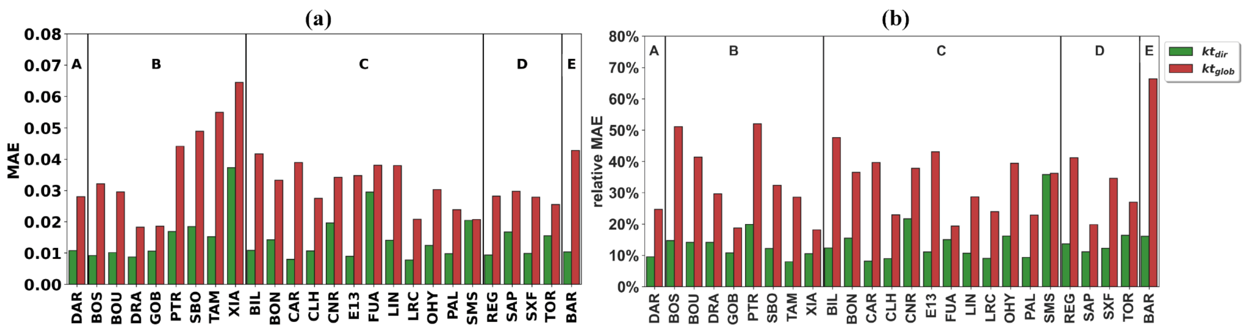

Figure 1.5.2.3. (**a**) Mean absolute error (MAE) and (**b**) relative MAE between MLA-AOD and AERONET AOD for Scenario 1 (kt_{dir}) and Scenario 2 (kt_{glob}). For the MLA-AOD, the “optimal” algorithm is applied. The horizontal lines

separate the stations based on the KG classes (A = Equatorial, B = Arid, C = Warm Temperate, D = Snow, and E = Polar).

The selection of solar irradiance type as an input feature significantly affects the model performance, with Scenario 1 constantly outperforming Scenario 2. The MAE (relative MAE) values ranges are 0.007–0.037 (7.9–35.9%) and 0.018–0.64 (18.1–66.3%) for Scenario 1 and 2, respectively, with the corresponding metrics for each station and Scenario 2 being approximately twice as high (Figure 1.5.2.3). Both scenarios show that the highest MAEs are recorded for XIA. This can be attributed to the high aerosol variability in that area due to the high air pollution levels due to local fossil fuel burning from automobiles, the transported polluted plumes from nearby regions, and the transport of dust particles. Despite the relatively high RMSE values in XIA, the relative errors are lower than 10%. The difference in the observed performance between the two scenarios is primarily attributed to the impact of aerosol load on GHI and DNI. DNI is highly sensitive to aerosol burden, improving the performance of MLAs when it is used as an input parameter.

The performance among MLAs is quite similar at each station, highlighting the model's versatility (Figure 1.5.2.4). Nevertheless, for both scenarios, ANN shows the highest number of appearances. For Scenario 1, the majority of the stations had the lowest MAE values for ANN (12/26), followed by MARS (6/26) and LGBM (5/26). The "best" MLA at each station is presented above each station in Figure 1.5.2.4.

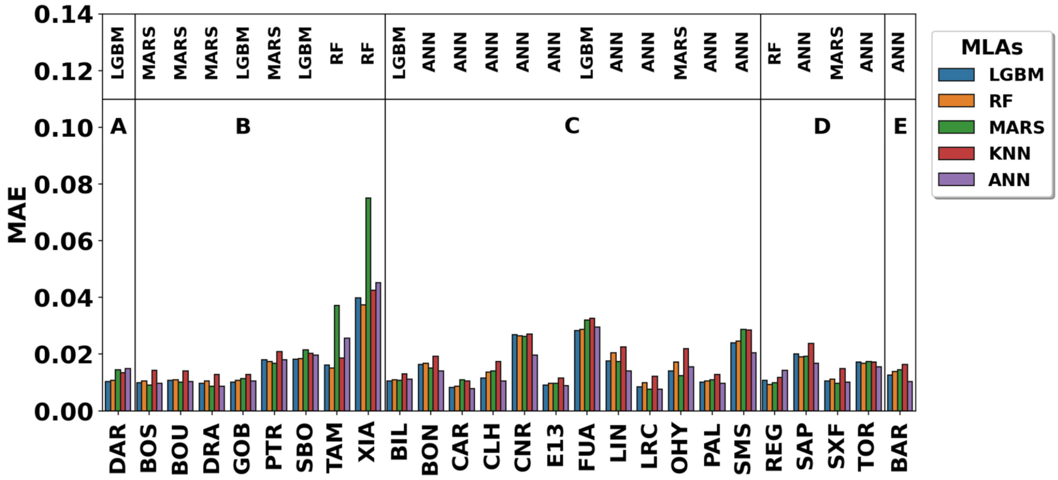

Figure 1.5.2.4. Mean absolute error (MAE) for Scenario 1 for each machine learning algorithm (MLA). The horizontal lines separate the stations based on the KG classes (A = Equatorial, B = Arid, C = Warm Temperate, D = Snow, and E = Polar). The MLA with the best performance is added above each station.

An interesting finding of the presented methodology is the adequate performance of MLAs at various climates, regions, and aerosol types (Figures 1.5.2.3 & 1.5.2.4). For example, at Tamanrasset (TAM) station, located in Southern Algeria, the main aerosol composition consists of mineral dust particles originating from the Sahara Desert, with a relatively high average AOD over time (here, AOD_{550nm} = 0.17). Those aerosol particles are quite absorbing. Although the applied methodology is blind regarding the aerosol size or absorptivity, it can retrieve AOD_{550nm} with reasonable accuracy (Scenario 1; MAE = 0.015–0.037). On the other hand, Carpentras, France (CAR), is placed near industrial and urban areas with fine-mode particles as the primary aerosol size. According to Logothetis et al. (2020), CAR is mainly affected by fine-absorbing (black carbon) and non-absorbing (sulfate and nitrate) particles. The applied methodology proved to be adequate for accurately retrieving AOD_{550nm} (Scenario 1; MAE = 0.007–0.011) over CAR.

MLA-AOD retrieval performance is also investigated for stations with mixed aerosol conditions, including both fine and coarse aerosol modes. For example, Sede Boker (SBO), Israel, is frequently affected by mineral dust particles emitted by nearby desert areas and fine-mode absorbing aerosols from local sources. The relevant errors in AOD_{550nm} range from 0.018 to 0.021.

The overall performance of MLA-AOD retrievals, including the "optimal" MLA and Scenario 1, is investigated against AERONET in Figure 1.5.2.5. MLAs document a high coefficient of determination (R^2 = 0.97), MAE of 0.01, and RMSE of 0.02 (Figure 1.5.2.5), highlighting the adequate performance of MLA-AOD methodology compared to AERONET. The majority of the AOD values were lower than 0.5, with the MLA-AOD performance being adequate (see the second plot in Figure 1.5.2.5). For high AOD values (>0.5), the MLA-AOD retrievals have the tendency to underestimate the AERONET measurements.

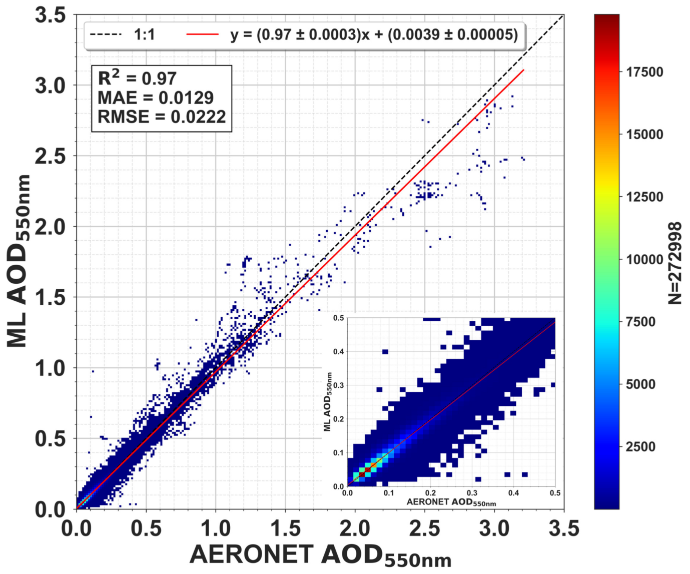

Figure 1.5.2.5. Density scatter plots of MLA-AOD and AERONET AOD retrievals. The black dashed line is the identical line, and the red solid line corresponds to the linear regression fit. On each plot, a second plot is presented, zoomed in for AOD values ranging between 0 and 0.5.

References

García, O.E.; Díaz, J.P.; Expósito, F.J.; Díaz, A.M.; Dubovik, O.; Derimian, Y.; Dubuisson, P.; Roger, J.-C. Shortwave radiative forcing and efficiency of key aerosol types using AERONET data. *Atmos. Chem. Phys.* **2012**, *12*, 5129–5145.

Gueymard, C.A.; Habte, A.; Sengupta, M. Reducing Uncertainties in Large-Scale Solar Resource Data: The Impact of Aerosols. *IEEE J. Photovolt.* **2018**, *8*, 1732–1737.

Holben, B.N.; Eck, T.F.; Slutsker, I.; Tanré, D.; Buis, J.P.; Setzer, A.; Vermote, E.; Reagan, J.A.; Kaufman, Y.J.; Nakajima, T.; et al. AERONET—A Federated Instrument Network and Data Archive for Aerosol Characterization. *Remote Sens. Environ.* **1998**, *66*, 1–16.

Huttunen, J.; Kokkola, H.; Mielonen, T.; Mononen, M.E.J.; Lipponen, A.; Reunanen, J.; Lindfors, A.V.; Mikkonen, S.; Lehtinen, K.E.J.; Kouremeti, N.; et al. Retrieval of aerosol optical depth from surface solar radiation measurements using machine learning algorithms, non-linear regression and a radiative transfer-based look-up table. *Atmos. Chem. Phys.* **2016**, *16*, 8181–8191.

Inness, A.; Ades, M.; Agustí-Panareda, A.; Barré, J.; Benedictow, A.; Blechschmidt, A.-M.; Dominguez, J.J.; Engelen, R.; Eskes, H.; Flemming, J.; et al. The CAMS reanalysis of atmospheric composition. *Atmos. Chem. Phys.* **2019**, *19*, 3515–3556.

Javadnia, E.; Abkar, A.; Schubert, P. Estimation of High-Resolution Surface Shortwave Radiative Fluxes Using SARA AOD over the Southern Great Plains. *Remote Sens.* **2017**, *9*, 1146.

Logothetis, S.-A.; Salamalikis, V.; Kazantzidis, A. Aerosol classification in Europe, Middle East, North Africa and Arabian Peninsula based on AERONET Version 3. *Atmos. Res.* **2020**, *239*, 104893.

Logothetis, S.-A.; Giannaklis, C.-P.; Salamalikis, V.; Tzoumanikas, P.; Raptis, P.-I.; Amiridis, V.; Eleftheratos, K.; Kazantzidis, A. Aerosol Optical Properties and Type Retrieval via Machine Learning and an All-Sky Imager. *Atmosphere* **2023**, *14*, 1266.

Reno, M.J.; Hansen, C.W. Identification of periods of clear sky irradiance in time series of GHI measurements. *Renew. Energy* **2016**, *90*, 520–531.

Salmon, A.; Quiñones, G.; Soto, G.; Polo, J.; Gueymard, C.; Ibarra, M.; Cardemil, J.; Escobar, R.; Marzo, A. Advances in aerosol optical depth evaluation from broadband direct normal irradiance measurements. *Sol. Energy* **2021**, *221*, 206–217.

Sanchez-Romero, A.; Sanchez-Lorenzo, A.; González, J.A.; Calbó, J. Reconstruction of long-term aerosol optical depth series with sunshine duration records. *Geophys. Res. Lett.* **2016**, *43*, 1296–1305.

Yang, D.; Yagli, G.M.; Quan, H. Quality Control for Solar Irradiance Data. In Proceedings of the 2018 IEEE Innovative Smart Grid Technologies—Asia (ISGT Asia), Singapore, 22–25 May **2018**; pp. 208–213.

Yang, D. SolarData package update v1.1: R functions for easy access of Baseline Surface Radiation Network (BSRN). *Sol. Energy* **2019**, *188*, 970–975.

1.6 Post-processing improvements of solar measurements

1.6.1. Retrieval of AOD_fine and AOD_coarse for PFR - AERONET - SKYNET - BTS

Authors: Angelos Karanikolas, Benjamin Torres, Marcos Herreras Giralda, Masahiro Momoi, Natalia Kouremeti, Julian Gröbner, Lionel Doppler and Stelios Kazadzis.

Introduction

Columnar aerosol properties such as size distribution and single scattering albedo are retrieved mainly using sky radiance scans in the almucantar geometry by sun and sky photometers mainly belonging to the AErosol RObotic NETwork (AERONET) (Dubovik and King 2000) and SKYNET. The almucantar scans are limited during the daily schedules and are further limited by clouds even if they do not cover the solar disk. On the other hand, direct sun scans are performed every 1 to 15 minutes depending on the instrument and the operator's schedule leading to substantially larger data availability. The direct solar irradiance measured by filter radiometers is regularly used to retrieve the aerosol optical depth (AOD). The homogeneity long-term AOD between different networks is regularly assessed in short-term campaigns (Kazadzis et al., 2018; Kazadzis et al., 2023; Doppler et al., 2023; Karanikolas et al., 2024) and long-term comparisons (Cuevas et al., 2019; Karanikolas et al., 2022).

One of the output parameters provided by AERONET almucantar scans is the separation of AOD to the corresponding AOD for fine (AOD_f) and coarse (AOD_c) mode at 4 wavelengths (440, 675, 870 and 1020 nm). AERONET provides this separation also at 500 nm using the direct sun scans and spectral deconvolution algorithm (SDA) (O'Neill et al., 2003). More recently methodologies were developed for the retrieval of aerosol size properties using only AOD at more than one wavelength (Kazadzis et al., 2013; Torres et al., 2017). The Generalized Retrieval of Atmosphere and Surface Properties-Aerosol Optical Depth (GRASP-AOD) is a flexible model that provides aerosol size properties separately for each mode of the aerosol size distribution and the separation of AOD to AOD_f and AOD_c at all wavelengths in which AOD is provided as input parameter. The methodology was validated in a large scale study for retrievals using AERONET AOD against the AERONET standard products (almucantar scans and SDA) (Torres & Fuertes, 2021).

Instruments, sites and methodology

In this work, we retrieved AOD_f and AOD_c from AOD by different instruments and present comparisons between them and the AOD_f-AOD_c provided by AERONET. AERONET uses for retrievals of aerosol properties the CIMEL CE318 sunphotometer (Holben et al., 1998). It provides AOD at 8 wavelengths in the range of 340-1640 nm every ~5-15 minutes and includes the largest number of stations worldwide (above 400 stations). Global Atmospheric Watch-Precision Filter Radiometer (GAW-PFR) network uses the Precision Filter Radiometer (PFR) (Wehrli, 2000), which provides AOD every minute at 4 wavelengths in the range of 368-862 nm . It includes 16 core and 14 associated stations worldwide and the PFR triad providing the WMO world reference for AOD.

AERONET and GAW-PFR include a number of common stations. 4 of them include continuous parallel measurements for several years and frequently significant aerosol loads (e.g. AOD at 500 nm above 0.1-0.2) or episodes of specific aerosol types (e.g. dust), namely Davos in Switzerland, Izana in Tenerife, Spain, Hohenpeissenberg and Lindenberg in Germany. Davos is an Alpine station at 1588 m with mostly pristine conditions, where larger quantities of aerosols may be transported by the surrounding urban and industrial areas, Sahara desert and biomass burning. Izana station is at 2371 m showing mainly very low AOD. However, there are several dust episodes every year due to the proximity to the Sahara desert. Hohenpeissenberg is a station with similar characteristics as Davos, but at a lower altitude (990 m). Finally, Lindenberg is at 128 m altitude close to the Berlin urban area. The GRASP-AOD retrievals of aerosol properties were validated against the AERONET products after a procedure to filter the data to ensure the quality of the comparisons. The reference datasets are cloud-screened by the AERONET algorithm and correspond to AERONET level 2.0 data. The PFR datasets are cloud-screened by the GAW-PFR algorithm. We also rejected all data corresponding to large AOD, AOD_f and AOD_c differences between AERONET inversions from almucantar scans and retrievals by the AERONET SDA according to the following empirically defined thresholds:

1. Coincident AOD, AOD_f and AOD_c differences at 500 nm <0.03.

2. Common daily AOD median differences <0.015 for AOD and <0.018 for AOD_f and AOD_c.

3. 80th-20th percentile of daily AOD, AOD_f and AOD_c difference <0.055.

The synchronisation threshold between inversions and spectral deconvolution algorithm was 7.5 minutes.

Regarding GRASP-AOD inversions, we removed all data not satisfying a modified version of the conditions in Torres & Fuertes 2021 for the inversion residuals (fitting of AOD between the forward and inversion model):

1. Absolute inversion fitting error < 0.01 if AOD at 412 nm is < 0.5 and < AOD412×0.011 + 0.007 if AOD at 412 is >0.5

2. AOD at 500 nm absolute error <0.01+0.005×AOD500

Additionally, we rejected data corresponding to large differences of synchronous AOD (30 seconds threshold) between GAW-PFR and AERONET according to the following thresholds required to keep the data:

1. Coincident AOD differences <0.09 for 380 and 440 nm, <0.06 for 500 nm and 0.04 for 870 nm.

2. Common daily AOD median differences <0.05 for 380 and 440 nm, <0.014 for 500 nm and <0.009 for 870 nm.

3. 80th-20th percentile of daily AOD difference <0.09 for 380 and 440 nm, <0.03 for 500 nm and <0.02 for 870 nm.

Finally, for all intercomparisons we keep only data corresponding to AOD>0.03 at 500 nm. For fine mode properties we keep only data corresponding additionally to AOD_f>0.02 and AE>0.3. For coarse mode the thresholds are AOD_c>0.02 and AE<1.8. These thresholds will be 'filters 1' hereafter.

The comparisons of AOD_f and AOD_c between PFR and AERONET SDA output are point-by-point with a synchronisation threshold of 30 seconds. For the comparisons between PFR and AERONET inversions (from almucantar scans), we use the median of the PFR retrievals during 5-minute intervals. The 5-minute intervals start up to 30 seconds earlier or later than the starting time of the almucantar scans.

Results

In Figure 1.6.1.1 we show the intercomparison of AOD_f between the GRASP retrievals using PFR AOD and the 2 AERONET products (sky radiance inversions and SDA) that satisfy the conditions described above. Both comparisons show excellent correlation (R>0.98) similar root mean square error (RMSE) and similar behaviour for either low and high aerosol loads (linear fit slope>0.97, intercept<0.01). The median differences are 0.001/0.005 and the standard deviations 0.011/0.01 for the comparisons with sky radiance inversions/SDA. The uncertainties of AOD_f and AOD_c vary for each case, but typically in the selected locations they are approximately 0.01-0.03 (available in the AERONET SDA data).

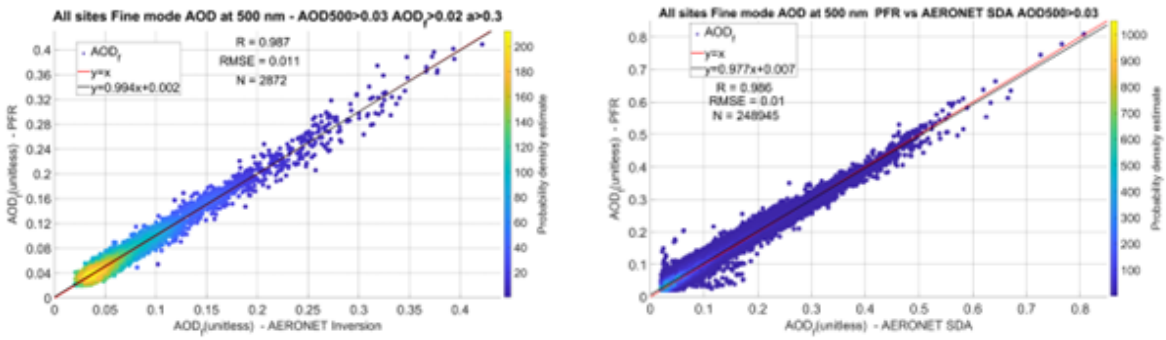

Figure 1.6.1.1: Scatter plot of the AOD_f from the AERONET inversions (left) or from the SDA (right) (X-axis) and the GRASP inversions using PFR AOD (Y-axis).

The AOD_c in general shows similar results as long as we make sure to remove inversions with large fitting errors as described earlier, since theoretically AOD_c=AOD-AOD_f. The validation of AOD_c however, shows differences from site to site as in 3 of the used locations most of the AOD corresponds to the fine mode, while in Izana the AOD is very low except the cases of Sahara dust episodes. During those episodes the coarse mode dominates the aerosol load. In Figure 1.6.1.2 we show the validation of AOD_c for Izana and Lindenberg, without the thresholds AOD>0.03 at 500 nm, AOD_c>0.02 and AE<1.8. Despite the presence of very low aerosol loads, the validation for Izana shows excellent results. On the other hand, in Lindenberg where the data availability of AOD_c>0.02-0.04 is substantially lower, we found lower correlation and large variance. For all sites AOD_c comparison satisfying the conditions mentioned in methodology, R=0.99, median difference is 0.003 and standard deviation 0.007.

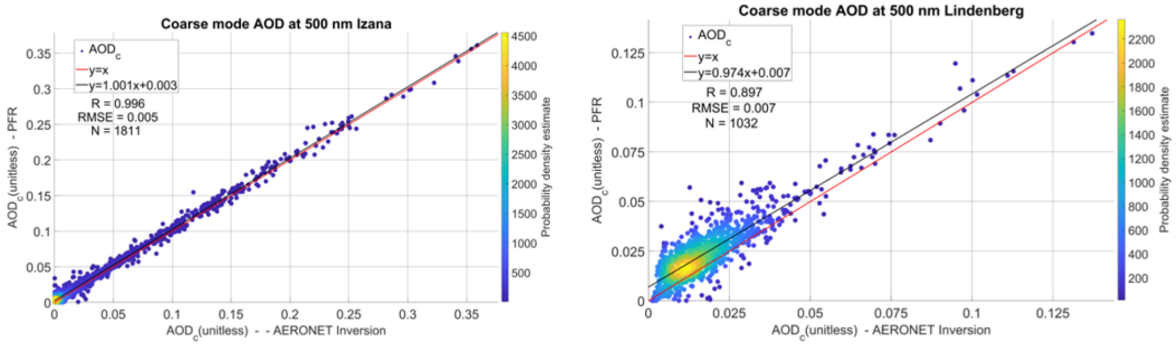

Figure 1.6.1.2: Scatter plot of the AOD_c for Izana (left) and Lindenberg (right) from the AERONET inversions (X-axis) and the GRASP inversions using PFR AOD (Y-axis).

The retrievals of aerosol properties using GRASP-AOD require the aerosol complex refractive index as input. As it is not known for most measurements, we used the AERONET climatology for each station. However, in most GAW-PFR stations this information is not available. Therefore, we repeated a subset of the retrievals at all 4 stations (1 year for Davos and Hohenpeissenberg, 2 years for Izana and Lindenberg) using either climatology for the refractive index or a fixed value for all months and sites to 1.45 for the real part and 0.003 for the imaginary part. In figure 1.6.1.3 we show the comparisons between AOD_f from AERONET and GRASP-AOD using each refractive index selection. Although the indicators show better values when using the climatology, in both cases the results are very similar. The median difference between AOD_f from GRASP-AOD and AERONET inversions is 0.003 for both cases of refractive index selection. The standard deviation 0.009 for climatological refractive index and 0.013 for fixed.

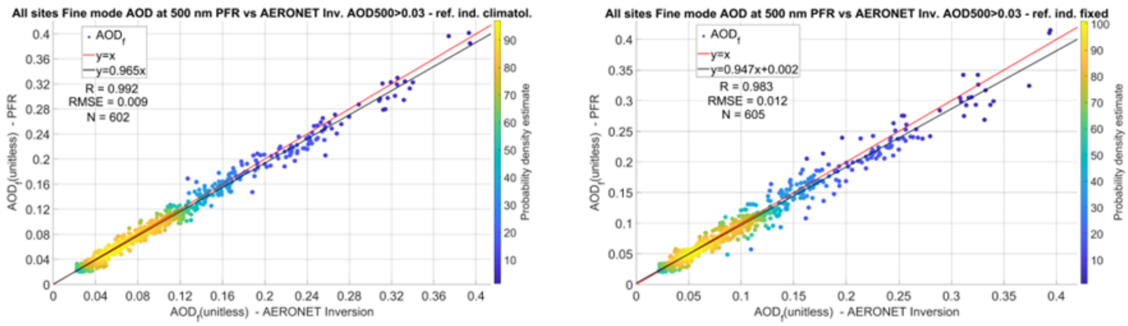

Figure 1.6.1.3: Scatter plot of the AOD_f from the AERONET inversions (X-axis) and the GRASP inversions using PFR AOD (Y-axis) for all sites using climatology for the refractive index (left) and fixed value (right).

The PFR and CIMEL measure at different wavelengths and their AOD at the common wavelengths is not the same. As a result the AOD_f and AOD_c retrieved by AOD from PFR and CIMEL are expected also to be different. In Figure 1.6.1.4 we show the CIMEL-PFR AOD comparison and AOD_f retrieved from GRASP-AOD using either AOD datasets. AOD_f shows lower R and larger RMSE, but linear fit slope closer to 1. However, all indicators show similar values. The separate effect of AOD difference and spectral range or resolution are not clarified yet as either may affect the retrievals.

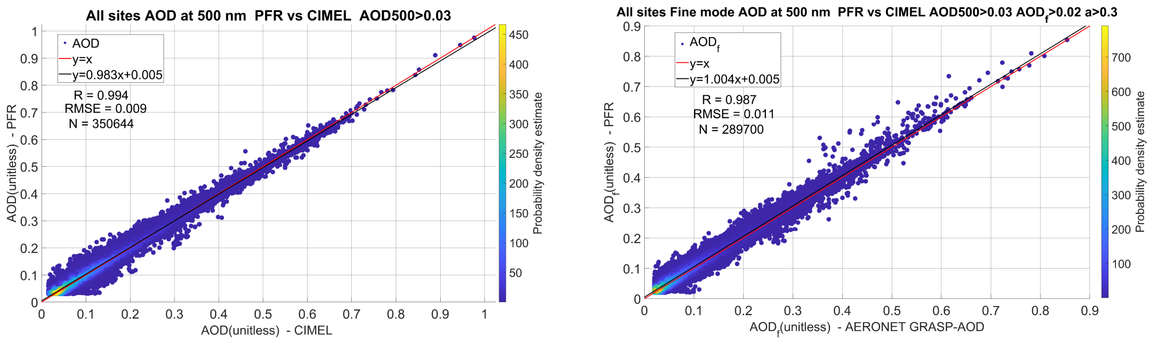

Figure 1.6.1.4: Scatter plot of the AOD (left) and AOD_f (right) the GRASP inversions using CIMEL (X-axis) and PFR AOD (Y-axis) for all sites.

Conclusions and outlook

In this work, we used the GRASP-AOD model to retrieve AOD_f and AOD_c from AOD datasets at 4 common locations of the GAW-PFR and AERONET networks. We also used the AERONET products (sky radiance inversions and SDA) as reference to validate the GRASP-AOD output.

The separation of AOD to fine and coarse mode using GRASP-AOD and AOD from PFR, shows excellent correlation with both AERONET products (R>0.98) and differences (median and standard deviation) within the AOD_f uncertainties of the SDA product. Using different refractive index selections as input to GRASP-AOD we saw no significant differences in the comparisons. Finally, the intercomparison from PFR and CIMEL AOD separation using GRASP-AOD showed similarly good results.

More work is intended (and already in progress) during the following period to compare the AOD_f and AOD_c retrievals from SKYNET and spectroradiometers with the AERONET and GAW-PFR retrievals. Common data from AERONET, GAW-PFR and SKYNET are available from the intercomparison campaigns Quality and Traceability of Atmospheric Aerosol Measurements or QUATRAM I, II and III) during the 2017 – 2021 period in Davos and Rome (Campanelli et al., 2024; Karanikolas et al., 2024), but also in Lindenberg for several years. Davos and Lindenberg also include the Precision Spectroradiometers (PSR) and BTS spectroradiometers (BTS), which measure the direct spectral irradiance >1000 wavelengths in the 300-1020 nm range for the PSR and >2000 wavelengths in the 2155 nm range for the BTS. The calibration of these spectroradiometers is absolute (W/m^2) and they are used to provide high spectral resolution AOD.

References

Campanelli, M., Estellés, V., Kumar, G., Nakajima, T., Momoi, M., Gröbner, J., Kazadzis, S., Kouremeti, N., Karanikolas, A., Barreto, A., Nevas, S., Schwind, K., Schneider, P., Harju, I., Kärhä, P., Diémoz, H., Kudo, R., Uchiyama, A., Yamazaki, A., Iannarelli, A. M., Mevi, G., Di Bernardino, A., and Casadio, S.: Evaluation of on-site calibration procedures for SKYNET Prede POM sun–sky photometers, Atmos. Meas. Tech., 17, 5029–5050, https://doi.org/10.5194/amt-17-5029-2024, 2024.

Cuevas, E., Romero-Campos, P. M., Kouremeti, N., Kazadzis, S., Räisänen, P., García, R. D., Barreto, A., Guirado-Fuentes, C., Ramos, R., Toledano, C., Almansa, F., and Gröbner, J.: Aerosol optical depth comparison between GAW-PFR and AERONET-Cimel radiometers from long-term (2005–2015) 1 min synchronous measurements, Atmos. Meas. Tech., 12, 4309–4337, https://doi.org/10.5194/amt-12-4309-2019, 2019.

Doppler, L., Akriti Masoom, A., and Karanikolas, A.: Create a list of existing and foreseen campaigns or experiments needed for night and day aerosol measurements and report on the data collection and analysis of the data/measurements, https://harmonia-cost.eu/wp-content/uploads/2023/10/COST_CA21119_HARMONIA-WG1_Deliverable-D11.pdf, 2023.

Dubovik, O. and King, M.: A flexible inversion algorithm for retrieval of aerosol optical properties from Sun and sky radiance measurements, J. Geophys. Res., 105, 20763–20696, 2000.

Holben, B. N., Eck, T. F., Slutsker, I., Tanré, D., Buis, J. P., Setzer, A., Vermote, E., Reagan, J. A., Kaufman, Y. J., Nakajima, T., Lavenu, F., Jankowiak, I., and Smirnov, A.: AERONET – A Federated Instrument Network and Data Archive for Aerosol Characterization, Remote Sens. Environ., 66, 1–16, https://doi.org/10.1016/s0034-4257(98)00031-5, 1998.

Karanikolas, A., Kouremeti, N., Gröbner, J., Egli, L., and Kazadzis, S.: Sensitivity of aerosol optical depth trends using long-term measurements of different sun photometers, Atmos. Meas. Tech., 15, 5667–5680, https://doi.org/10.5194/amt-15-5667-2022, 2022.

Karanikolas, A., Kouremeti, N., Campanelli, M., Estellés, V., Momoi, M., Kumar, G., Nyeki, S., and Kazadzis, S.: Intercomparison of aerosol optical depth retrievals from GAW-PFR and SKYNET sun photometer networks and the effect of calibration, Atmos. Meas. Tech., 17, 6085–6105, https://doi.org/10.5194/amt-17-6085-2024, 2024.

Kazadzis, S., Veselovskii, I., Amiridis, V., Gröbner, J., Suvorina, A., Nyeki, S., Gerasopoulos, E., Kouremeti, N., Taylor, M., Tsekeri, A., and Wehrli, C. (2014): Aerosol microphysical retrievals from precision filter radiometer direct solar radiation measurements and comparison with AERONET, Atmos. Meas. Tech., 7, 2013–2025, https://doi.org/10.5194/amt-7-2013-2014.

Kazadzis, S., Kouremeti, N., Diémoz, H., Gröbner, J., Forgan, B. W., Campanelli, M., Estellés, V., Lantz, K., Michalsky, J., Carlund, T., Cuevas, E., Toledano, C., Becker, R., Nyeki, S., Kosmopoulos, P. G., Tatsiankou, V., Vuilleumier, L., Denn, F. M., Ohkawara, N., Ijima, O., Goloub, P., Raptis, P. I., Milner, M., Behrens, K., Barreto, A., Martucci, G., Hall, E., Wendell, J., Fabbri, B. E., and Wehrli, C.: Results from the Fourth WMO Filter Radiometer Comparison for aerosol optical depth measurements, Atmos. Chem. Phys., 18, 3185–3201, https://doi.org/10.5194/acp-18-3185-2018, 2018
.

Kazadzis, S., Kouremeti, N., and. Gröbner, J.: Fifth WMO Filter Radiometer Comparison (FRC-V) 27 September to 25 October 2021, Davos, Switzerland, WMO GAW report 280, https://library.wmo.int/records/item/66263-fifth-wmo-filter-radiometer-comparison-frc-v?offset=5, (last access: 1 February 2024), 2023.

Torres, B., Dubovik, O., Fuertes, D., Schuster, G., Cachorro, V. E., Lapyonok, T., Goloub, P., Blarel, L., Barreto, A., Mallet, M., Toledano, C., and Tanré, D.: Advanced characterisation of aerosol size properties from measurements of spectral optical depth using the GRASP algorithm, Atmos. Meas. Tech., 10, 3743–3781, https://doi.org/10.5194/amt-10-3743-2017, 2017.

Torres, B. and Fuertes, D. (2021): Characterization of aerosol size properties from measurements of spectral optical depth: a global validation of the GRASP-AOD code using long-term AERONET data, Atmos. Meas. Tech., 14, 4471–4506, https://doi.org/10.5194/amt-14-4471-2021.

Wehrli, C.: Calibrations of filter radiometers for determination of atmospheric optical depth, Metrologia, 37, 419–422, https://doi.org/10.1088/0026-1394/37/5/16, 2000.

1.6.2. NO_2 effects on AOD retrievals

Based on the HARMONIA project #12: NO_2 effects on AOD retrievals. Authors: Stelios Kazadzis, Akriti Masoom.

An analysis was performed for the investigation of NO_2 absorption effect on aerosol optical depth (AOD) and Ångström exponent (AE) retrievals from Aerosol Robotic Network (AERONET) sun photometers (which use OMI (Ozone Monitoring Instrument) climatology for NO_2 representation) by the synergistic use of accurate NO_2 characterization for optical depth estimation from co-located ground-based measurements (Pandonia Global Network (PGN) Pandora spectroradiometer) at several sites worldwide by Masoom et al. (2024). It was found that the AOD bias was the most affected at 380 nm by NO_2 differences between AERONET OMI climatological NO_2 representation and PGN NO_2 measurements, followed by 440, 340, and 500 nm, respectively and AERONET AOD was overestimated in half of the cases, while also underestimated in other cases due to the differences between the NO_2 “real” (PGN NO_2) values and AERONET OMI climatological NO_2 representation. For about one-third of these stations (total 33 co-located stations), the mean difference in NO_2 and AOD (at 380 and 440 nm) was observed to be above 0.5×10^{-4} mol m^{-2} and 0.002, respectively that can be considered a systematic contribution by NO_2 differences to the uncertainties in the AOD measurements that are reported to be of the order of 0.01. At highly urbanized/industrialized locations and during extreme NO_2 loading scenarios (i.e. 10 % highest differences), the AOD differences were found to be even higher that were at the limit of or higher than the reported 0.01 uncertainty in the AOD measurement (some examples are shown in Fig. 2.1). The AOD-derivative product, AE, was also affected by the NO_2 correction on the spectral AOD. The normalized frequency distribution of AE (at 440–870 and 340–440 nm wavelength pair) was found to be narrower for a broader AOD distribution for some stations, and vice versa for other stations. A higher relative error at the shorter wavelength (among the wavelength pairs used for AE estimation) led to a shift in the peak of the AE difference distribution towards a higher positive value, while a higher relative error at a lower wavelength shifted the AE difference distribution to a negative value for the AOD overestimation case, and vice versa for the AOD underestimation case. For rural locations, the mean NO_2 differences were found to be mostly below 0.50×10^{-4} mol m^{-2}, with the corresponding AOD differences being below 0.002, and in extreme NO_2 loading scenarios, it went above this value and reached above 1.00×10^{-4} mol m^{-2} for some stations, leading to higher AOD differences but below 0.005.

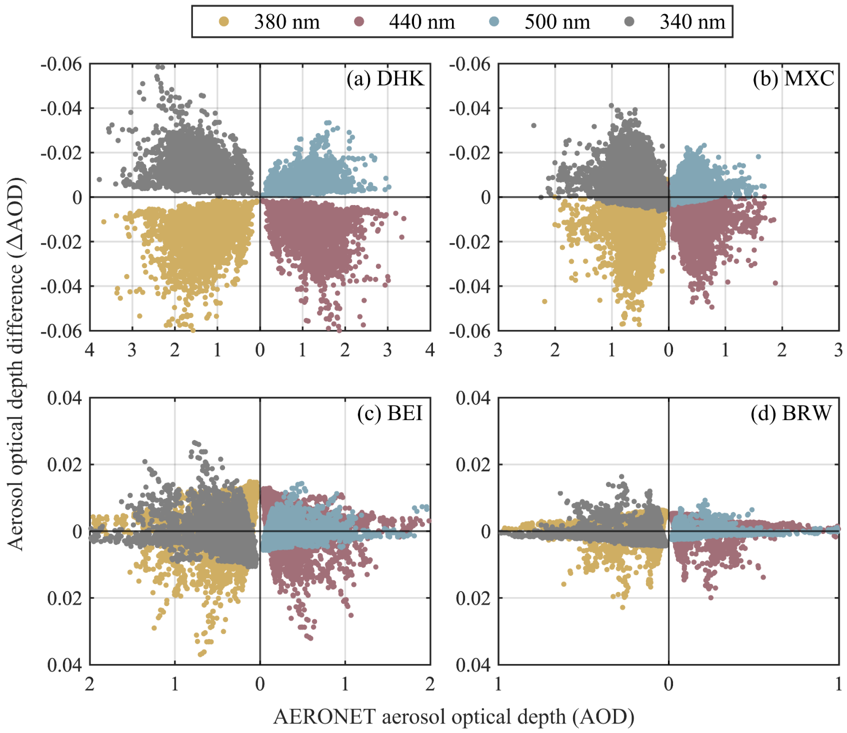

Figure 1.6.2.1.: Variation of AOD differences calculated as original AERONET AOD minus Pandora NO_2 correction based AOD differences as a function of AOD at 340, 380, 440, and 500 nm for stations with a mean NO_2 offset of more than 0.5×10^{-4} mol m^{-2} and a mean AOD difference offset above 0.002. For NO_2 underestimation cases (a, b) below 0 for 340 and 500 nm and AOD above 0 for 380 and 440 nm represent positive AOD differences. For NO_2 overestimation cases (c, d), AOD below 0 for 340 and 500 nm and AOD above 0 for 380 and 440 nm represent negative AOD differences. (Figure credit: Masoom et al., 2024)

A similar analysis but more focussed on one site (Rome, Italy) performed by Drosoglou et al. (2023) dealt with the NO_2 absorption effect on AOD, AE and single scattering albedo (SSA) for both the AERONET and SKYNET networks where it was found to systematically overestimate AOD and AE (an example of one day of the analysis is shown in Fig. 1.6.2.1.). The average AOD bias found for Rome was relatively low for AERONET (~0.002 at 440 nm and ~0.003 at 380 nm) compared to the retrieval uncertainties but quite a bit higher for SKYNET (~0.007). On average, an AE bias of ~0.02 and ~0.05 was estimated for AERONET and SKYNET, respectively, while for the cases of relatively high NO_2 levels (> 0.7 DU), the mean AOD bias was found within the range 0.009–0.012 for AERONET, depending on wavelength and location, and about 0.018 for SKYNET. Finally, the uncertainty in assumptions on NO_2 on the retrieved values of SSA at 440 nm lead to an average positive bias of about 0.02 (2 %) in both locations for high NO_2 loadings (> 0.7 DU).

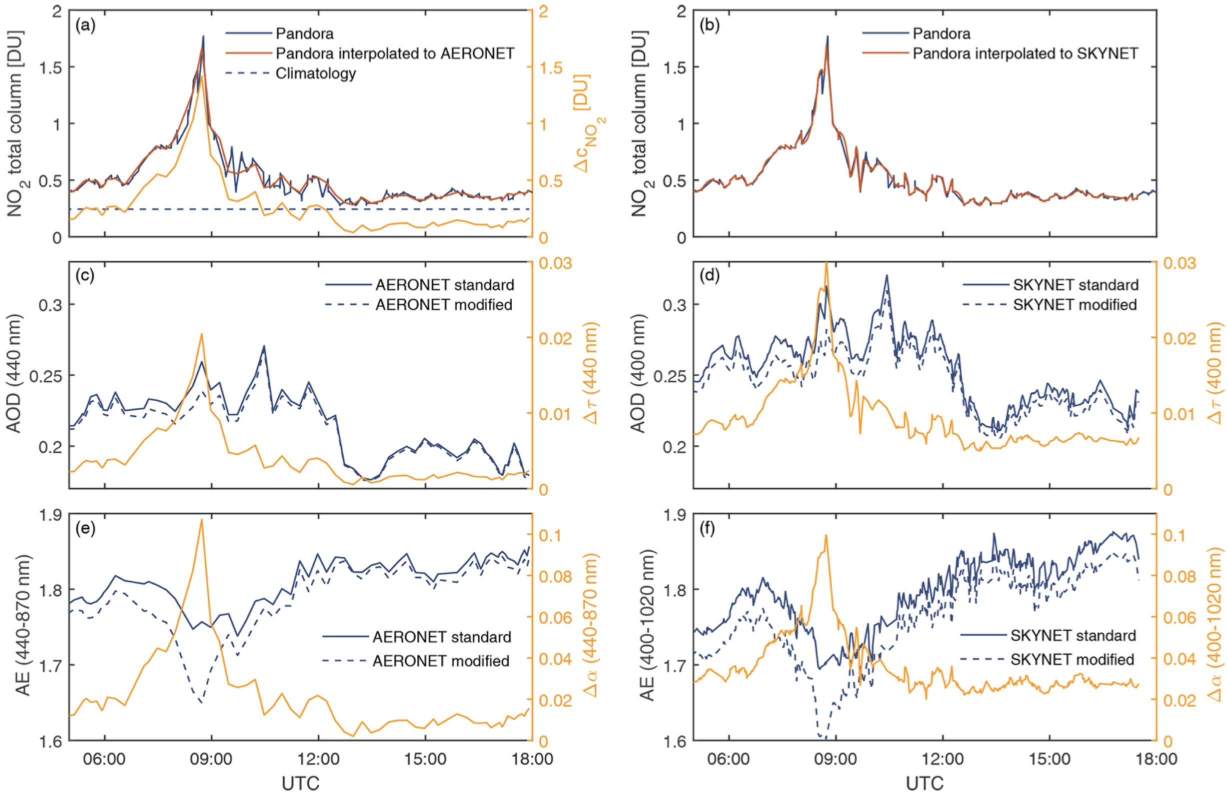

Figure 1.6.2.2.: Analysis of a specific day i.e., 25 June 2020 for Rome from both AERONET and SKYNET for (a, b) deviation of climatology from Pandora total NO_2 column measurements, (c, d) AOD (solid blue line), its improvement using Pandora NO_2 (dashed blue line), and the magnitude of improvement (light orange line and right y-axis) and (e, f) similar to panels (c) and (d) but for AE retrievals. (Figure credit: Drosoglou et al., 2023)

NO_2 induced differences in AOD values that were found to be close to the limit or higher than the reported 0.01 uncertainty reported by Giles et al. (2019) and Eck et al. (1999) for AERONET AOD measurements can be considered relatively significant taking into account that this 0.01 uncertainty is a result of various aspects such as calibration (primarily), post processing, and instrument/measurement uncertainty. Moreover, some AOD measuring networks (e.g. SKYNET, Nakajima et al., 2020; GAW-PFR, Kazadzis et al., 2018) do not officially account for NO_2 optical depth contribution to AOD measurements, and therefore, NO_2 correction in this case will be considered as a systematic AOD overestimation.

References:

Masoom, A., Kazadzis, S., Valeri, M., Raptis, I.-P., Brizzi, G., Papachristopoulou, K., Barnaba, F., Casadio, S., Kreuter, A., and Niro, F.: Assessment of the impact of NO2 contribution on aerosol-optical-depth measurements at several sites worldwide, Atmos. Meas. Tech., 17, 5525–5549, https://doi.org/10.5194/amt-17-5525-2024, 2024.

Drosoglou, T., Raptis, I.-P., Valeri, M., Casadio, S., Barnaba, F., Herreras-Giralda, M., Lopatin, A., Dubovik, O., Brizzi, G., Niro, F., Campanelli, M., and Kazadzis, S.: Evaluating the effects of columnar

NO2 on the accuracy of aerosol optical properties retrievals, Atmos. Meas. Tech., 16, 2989–3014, https://doi.org/10.5194/amt-16-2989-2023, 2023.

Giles, D. M., Sinyuk, A., Sorokin, M. G., Schafer, J. S., Smirnov, A., Slutsker, I., Eck, T. F., Holben, B. N., Lewis, J. R., Campbell, J. R., Welton, E. J., Korkin, S. V., and Lyapustin, A. I.: Advancements in the Aerosol Robotic Network (AERONET) Version 3 database – automated near-real-time quality control algorithm with improved cloud screening for Sun photometer aerosol optical depth (AOD) measurements, Atmos. Meas. Tech., 12, 169–209, https://doi.org/10.5194/amt-12-169-2019, 2019.

Eck, T. F., Holben, B. N., Reid, J. S., Dubovik, O., Smirnov, A., O'Neill, N. T., Slutsker, I., and Kinne, S.: Wavelength dependence of the optical depth of biomass burning, urban, and desert dust aerosols, J. Geophys. Res., 104, 31333–31349, https://doi.org/10.1029/1999JD900923, 1999.

Nakajima, T., Campanelli, M., Che, H., Estellés, V., Irie, H., Kim, S.-W., Kim, J., Liu, D., Nishizawa, T., Pandithurai, G., Soni, V. K., Thana, B., Tugjsurn, N.-U., Aoki, K., Go, S., Hashimoto, M., Higurashi, A., Kazadzis, S., Khatri, P., Kouremeti, N., Kudo, R., Marenco, F., Momoi, M., Ningombam, S. S., Ryder, C. L., Uchiyama, A., and Yamazaki, A.: An overview of and issues with sky radiometer technology and SKYNET, Atmos. Meas. Tech., 13, 4195–4218, https://doi.org/10.5194/amt-13-4195-2020, 2020.

Kazadzis, S., Kouremeti, N., Nyeki, S., Gröbner, J., and Wehrli, C.: The World Optical Depth Research and Calibration Center (WORCC) quality assurance and quality control of GAW-PFR AOD measurements, Geosci. Instrum. Method. Data Syst., 7, 39–53, https://doi.org/10.5194/gi-7-39-2018, 2018.

2. Improvements on the lunar/stellar based techniques

2.1 Current status of the stellar and lunar techniques

Based on the HARMONIA project #3: "State of the art research on Stellar and lunar photometers measurements intercomparison". Authors: Yeser Aslanoglu, Monica Campanelli.

Daytime measurements of AOD are routinely conducted using sun radiometers. Solar photometry is considered a robust passive technique and it is also used to validate satellite retrievals. The solar photometry technique has its limitations, particularly because it cannot be used at night due to the significantly weaker light reflected by the moon compared to sunlight. This limitation is especially significant for studying AOD climatology in polar regions, where the Sun is absent for several months during the polar night. For example, at Ny-Ålesund (Svalbard, Norway), the Sun remains below 5° of elevation from October 10 to March 4, restricting the period available for conventional photometric measurements. To address this issue and fill historical gaps in AOD climatology, measuring irradiance from stars or reflected moonlight has been proposed. The main differences between stellar and lunar photometry lie in their simplicity, costs, and maintenance operations. Generally, lunar photometry can be considered an adaptation of the sun-photometry technique, while stellar photometry is a more complex and sophisticated method requiring specialized astronomical instruments and personnel dedicated to routine operation.

Stellar photometry technique

Starlight is collected by a telescope and passes through a filter wheel with narrow band filters. A CCD camera is used as a detector because its linear response and high quantum efficiency make it ideal for this purpose. The system also includes an external wide-field CCD camera to ensure that the registered star is correctly centered (Pérez-Ramirez et al., 2007). The well-known Beer-Lambert law in term of the star photometer signal voltage is:

$$V_{(\lambda)} = V_{0_{(\lambda)}} e^{-m\tau_{atm(\lambda)}} \quad (1)$$

Where $V_{(\lambda)}$ is the voltage measured by the instrument, $V_{0(\lambda)}$ represent the extraterrestrial voltage measured at the top-of-atmosphere, m is the optical air masses and $\tau_{atm(\lambda)}$ is the total spectral atmospheric optical depth. For stellar photometry, the voltage registered by the camera is the number of counts ($CN_{(\lambda)}$) divided by the exposure time. The measurements can be expressed in terms of star magnitude, S, defined in Leiterer et al., 1995, so that eq.1 can be re-written as:

$$lnS_{(\lambda)} = lnS_{0(\lambda)} - 1.086m\tau_{atm(\lambda)} \quad (2)$$

Where $S_{(\lambda)}$ is the star magnitude at Earth's surface, and $S_{0(\lambda)}$ the extraterrestrial star magnitude.

The star magnitude was defined by Leiterer et al. 1995, as $S_{(\lambda)}$ = -2.5 log10($f_{(\lambda)}/f0_{(\lambda)}$) where $f_{(\lambda)}$ is the flux received at the Earth's surface and $f0_{(\lambda)}$ the standard reference flux. But, the flux is the number of counts divided by exposure time, so that the Beer-Lambert law for star photometry can be written like in eq.2 and the value of 2.5/log10 is approximately 1.086.

At this point, the spectral optical depth of the atmosphere can be obtained as:

$$\tau_{atm(\lambda)} = \frac{lnS_{0(\lambda)} - lnS_{(\lambda)}}{1.086m} \quad (3)$$

Herber et al., 2002 defined this last expression as a one-star method, which requires the extraterrestrial magnitudes of the considered star. The Langley method (Schmid and Wehrli, 1995), also used in solar photometry for the same calibration purpose, can be used. By using this method, $S_{0(\lambda)}$ can be obtained as the intercept in the plot of stellar photometer readings versus air masses. Because stable atmospheric conditions are required during the calibration process, high-mountain places represent an ideal location. Since moving the instrumental setup is a critical operation, Leiterer et al. (1995) proposed the use of the two-star method. Exposures of two different stars are now needed. In this case, stable atmospheric conditions are required only for a few minutes during the acquisition process. By assuming constant optical depth between two exposures, only the difference $S_{01(\lambda)}$-$S_{02(\lambda)}$ need to be known. The common atmospheric optical depth can be retrieved as:

$$\tau_{atm} = \frac{(lnS_{1(\lambda)} - lnS_{2(\lambda)}) - (lnS_{01(\lambda)} - lnS_{02(\lambda)})}{1.086(m_1 - m_2)} \quad (4)$$

Where $S_{1(\lambda)}$ and $S_{2(\lambda)}$ are the magnitudes measured by the photometer, and $S_{01(\lambda)}$ and $S_{02(\lambda)}$ are the extraterrestrial magnitudes. The subscripts stand for the stars considered. The two-star method allows the use of extraterrestrial star magnitudes obtained from star catalogue (Leiterer et al., 1995). In this way one can measure AOD without a previous instrument calibration.

Lunar photometry technique

In the last decades, many attempts have been made to use the Moon as a light source to retrieve aerosol properties. The stability of the lunar surface reflectance makes the Moon a nearly perfect calibration source. However, there are significant challenges due to the non-uniformity of the lunar surface albedo resulting from the presence of lunar maria and highlands, the brightness variation arising from lunar phase and libration, and the strong dependence of surface reflectivity on phase angle. The complexity of these dependencies effectively mandates the use of a lunar radiometric model to compare against spacecraft observations of the Moon.

The USGS in Flagstaff (Arizona, US) has acquired the observational data and proposed the RObotic Lunar Observatory (ROLO) model (Kieffer and Stone, 2005). This model can provide the exoatmospheric lunar irradiance for any given location and time. The model is based on fitting thousands of lunar measurements acquired over more than 8 years with the ground-based ROLO telescopes in 32 wavelength bands from 350 to 2450 nm. The ROLO model uses an empirically derived analytic equation to predict the lunar disk-equivalent reflectance (A_k) in the spectral band k using only geometric variables (Kieffer and Stone, 2005):

$$lnA_k = \sum_{i=0}^{3} a_{ik} g^i + \sum_{j=1}^{3} b_{jk} \Phi^{2j-1} + c_1\phi + c_2\theta + c_3\Phi\phi + c_4\Phi\theta + d_{1k} e^{-g/p_1} + d_{2k} e^{-g/p_2} + d_{3k} cos((g - p_3)/p_4) \quad (5)$$

Where g is the absolute phase angle, θ and ϕ are the selenographic latitude and longitude of the observer, and ϕ is the selenographic longitude of the Sun. The ROLO model provides exo-atmospheric lunar irradiance with relatively high precision. The band-average absolute residuals are about 1%, based on comparisons between ROLO empirical irradiances and hundreds of ROLO observations. This high precision makes the ROLO model a valuable tool for calibrating measurements and interpreting data for aerosol property retrievals. As always, for the retrieve of AOD during nighttime, the Beer-Lambert law can be used:

$$V_{(\lambda)} = V_{O(\lambda)} e^{-m(\theta)\tau_{(\lambda)}} \quad (6)$$

Where $V_{(\lambda)}$ is the output voltage, $V_{O(\lambda)}$ the extraterrestrial voltage which include lunar phase variations as well as Earth-Moon and Moon-Sun distances, m is the relative optical air mass (and function of the moon zenith angle θ), and $\tau_{(\lambda)}$ the spectral optical depth. To account for the change in lunar illumination during the course of the night, and for the distant effect on lunar irradiance, the V_O term of Eq. (6) can be modified as:

$$V_{0,j} = I_{0,j} k_j \quad (7)$$

Where $I_{0,j}$ is the extraterrestrial irradiance in a certain channel with a central wavelength at j, and k_j is a constant that depends on the instrument features such as the calibration coefficient and the instrument's solid view angle $I_{0,j}$ is calculated using the ROLO lunar disk-equivalent reflectances (A_k) in Eq. (5). The exact formula can be found in Barreto et al., 2013. In the same paper, Barreto et al. proposed the Lunar-Langley Method for the calibration of the instrument. Basically, the logarithmic form of Eq. (6) and Eq. (7), together with a least square fitting procedure are used to obtain the instrument's calibration constant (k_j) as the intercept of the fitting line. Once these constants are known, it is possible to retrieve AOD from an individual measurement:

$$\tau_{a,j} = \frac{ln(k_j) - ln\left(\frac{V_j}{I_{0,j}}\right) - m_{atm}(\theta)\, \tau_{atm,j}}{m_{a(\theta)}} \quad (8)$$

The subscript 'atm' accounts for air mass and optical depth of each atmospheric attenuator with the exception of aerosols. Román et al. (2020), proposed the use of the RIMO (ROLO Implementation for

Moon’s Observation) model to retrieve AOD during night-time, based on the assumption that the calibration constants for solar channels can be transferred to the Moon. Because authors found an underestimation of AODs retrieved by using this model (dependent on the optical air mass), they proposed a correction factor that, multiplied by the RIMO value, gives a more accurate extraterrestrial lunar irradiance that can be used for a more accurate retrieval of AODs during night. PREDE-POMs from Skynet network also measured the nocturnal aerosol optical depth by directly measuring the moon's irradiance (Uchiyama et al. 2019). They modified the POM sun model to adjust the amplification and sensor position, resulting in good measurements at 340 and 380 nm (the results in the SWIR range were not as good yet). A four-quadrant photodiode was added to account for the moon's phase angle. The reflectance at the nominal POM wavelengths was obtained by linearly interpolating between the two closest ROLO wavelengths. The innovation in the procedure adopted by Skynet, is in the development of an on-site calibration procedure that makes use of the solar calibration constant, obtained by an Improved Langley method, to retrieve moon calibration constant .

State of the art research on Stellar and lunar photometers measurements intercomparison

Only six (Fig. 2.1.1) are plenty devoted to routine aerosol monitoring. Five of these stellar photometers were developed by Dr. Schulz and Partner GmbH, and are located at four different places in Ny-Ålesund (Norway), Eureka and two instruments in Sherbrooke (Canada) and Lindenberg (Germany). The sixth one is the EXCALIBUR star photometer (EXtinction CAmera and LumIiance BackgroUnd Register), developed by Astronómica S.L., belonging to the Atmospheric Physics Group of the University of Granada (UGR), installed in Granada, Spain, but out of service since more than 5 years . All of them are co-located with AERONET sun -moon photomers (Figure 2.1.1).

The most recent is the SCILLA (Summer Campaign for Intercomparison of Lunar measurements of Lindenberg’s Aerosol) nocturnal AOD campaign, held in Lindenberg in Summer 2020, involving lunar photometers of all three types (Cimel, PFR, Prede), two stellar photometers, a Raman lidar, and some COBALD balloon-carried AOD radiosondes. The aim was to estimate the differences of AOD obtained with lunar photometers of the same type (Cimel CE318T in lunar modus) and compare them to AOD obtained from instruments of other types (Prede, PFR) and the two stellar photometers (Schuz & Partner SPST). Publications of results are not yet available. Also, a focus was set on the synergy total column measurements (AOD from photometers) with profiling measurements (LIDAR, COBALD). SCILLA was also an opportunity to validate the lunar reflectance model LIME versus the reference model RIMO. SCILLA was the unique campaign using an harmonized process of data inversion (ozone, NO2, trace gasses and rayleigh optical depth computed the same way for all the systems).

Parallel measurements of stellar/lunar photometers are still running *until* 2022 in Lindenberg .

The ANACC (Arctic Night Aerosol Characterization Campaign) campaign was held during the polar night (February 2020) in Ny Ålesund, involving two kinds of lunar photometers (Lunar PFR and Cimel CE318T in lunar modus), a stellar photometer and a Raman-Lidar. In addition to the instrument intercomparison, this campaign focused on Arctic Haze and Polar Stratospheric Clouds, whose optical properties could be investigated. The main benefit of this campaign was to confront in the polar night the two operating lunar photometers of this time (February 2020): Lunar PFR and Cimel CE318T in lunar modus. Also the synergy Lidar and stellar photometer was a great benefit to estimate the contribution of PSC (Polar Stratospheric Cloud) in the columnar aerosol+PSC optical depth measured with a photometer.

Since 2019 in Ny-Alesund, there are still parallel stellar/Lunar measurements at the station AWIPEV (Graßl et al 2024).

Another multi-instrument nocturnal intercomparison campaign, described in Barreto et al., 2019, was held in the high-mountain Izaña Observatory during June, 2017. Two types of lunar photometers and one stellar photometer have been involved. The quality of lunar measurements to the AOD stellar measurements and the lunar exo-atmospheric irradiance model have been evaluated. The nocturnal campaign was the first “big test” after four years of operational measurements with Cimel Photometer 318T in lunar modus in the AERONET network. 6 Cimel photometers in lunar modus were involved, allowing to estimate the spread between the Cimels. The lunar reflectance model could be improved (ROLO to RIMO), and pointing issues could be analyzed comparing the lunar PFR to the Cimel instruments. Particularly AOD comparative analysis was performed against the Cimel sun-moon-photometers at nominal wavelengths of 440, 500, 675 and 870 nm. In this analysis the stellar photometer can be considered to be an independent source of AOD at night, since its outputs do not depend on any lunar irradiance models. Differences within the expected AOD uncertainty for both photometric techniques (±0.02) were found alongside noticeable AOD fluctuations in star photometry. These fluctuations are associated with the effect of atmospheric turbulence, especially important for low AOD values. Fluctuations in moon photometry have been found to be considerably lower, therefore demonstrating the better capabilities of lunar photometry to measure low aerosol contents.

Former AOD comparisons in August 2014, by the Granada station, were published in Barreto et all 2016. During this period, stellar information in 880, 500 and 440 nm channels, close to CE318-T wavelengths, were extracted showing high regression coefficients for the three channels and reduced mean biases (MB) and root mean square (RMSD) deviations values in case of longer wavelength channels (≤ 0.001 for 870 nm and ≤ 0.013 for 500 nm). Higher discrepancies were found in the case of 440 nm channel (MB = -0.033 and RMSD = 0.018). This might be attributed to a calibration problem in the star photometer in this channel.

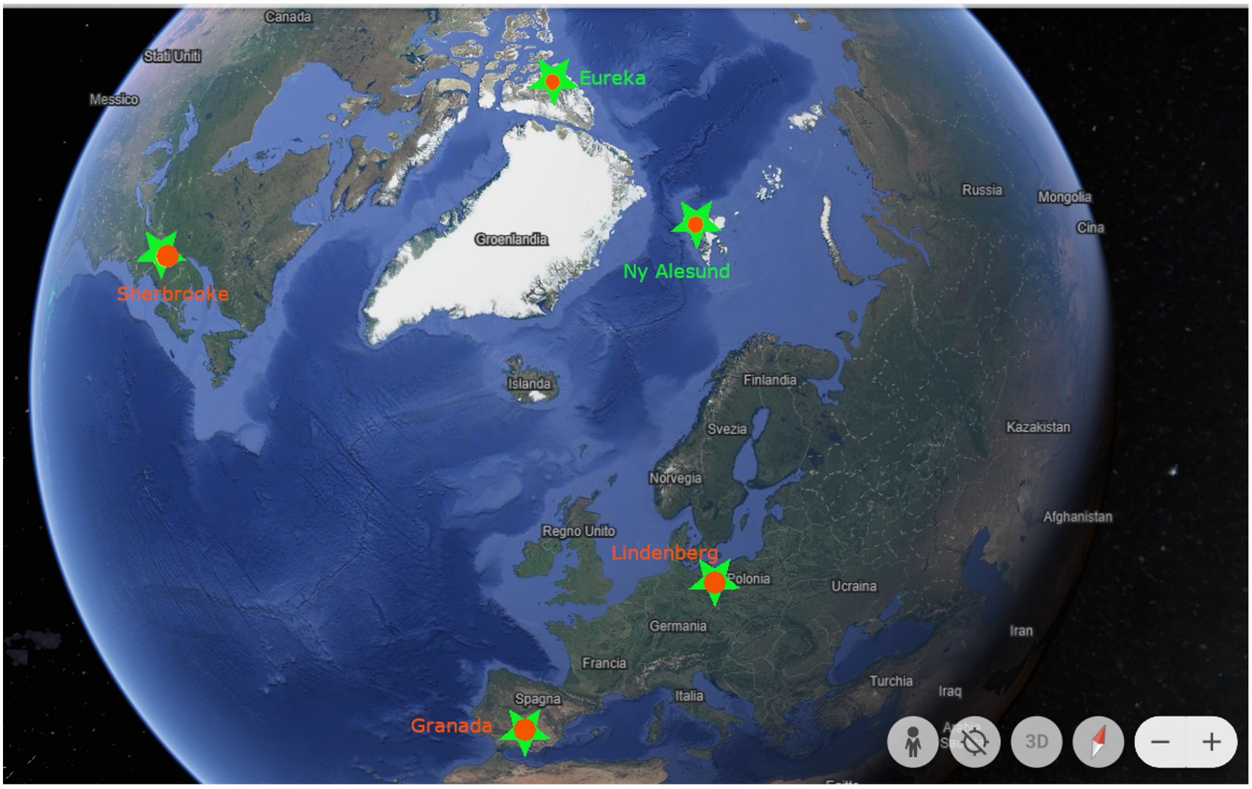

Figure 2.1.1 Maps of stellar photometers (star) and co-located moon Aeronet (red circle) photometers

Ivănescu et al., 2021, with the ultimate goal of improving starphotometry accuracy in the Eureka site, analysed a large variety of sources that could induce systematic (absolute) errors and classified them by their impact on each parameter involved in the AOD retrieval. The contamination from stellar and telluric gas absorption lines in ground-based collected spectra (due to the interaction of the light from astronomical objects with the constituents of the Earth's atmosphere) may induce large AOD errors. Such errors are, nevertheless, mitigated with proper channel allocation. Starphotometry reliability improvement is also pursued by characterizing the non-systematic, random errors, as well as those related to constant retrievals through Langley plot calibration. All the proposed improvements can be validated in intercomparison observation campaigns with other co-located instruments such as the Cimel moon photometer and the profiling backscatter lidar at the Eureka site.

References

Barreto et al., 2013. *A new method for nocturnal aerosol measurements with a lunar photometer prototype.* Atmospheric Measurement techniques, 585-598, doi:10.5194/amt-6-585-2013

Barreto, Á., Cuevas, E., Granados-Muñoz, M.-J., Alados-Arboledas, L., Romero, P. M., Gröbner, J., Kouremeti, N., Almansa, A. F., Stone, T., Toledano, C., Román, R., Sorokin, M., Holben, B., Canini, M., and Yela, M.: The new sun-sky-lunar Cimel CE318-T multiband photometer – a comprehensive performance evaluation, Atmos. Meas. Tech., 9, 631–654, https://doi.org/10.5194/amt-9-631-2016, 2016.

A. Barreto, R. Román, E. Cuevas, D. Pérez-Ramírez, A.J. Berjón, N. Kouremeti, S. Kazadzis, J. Gröbner, M. Mazzola, C. Toledano, J.A. Benavent-Oltra, L. Doppler, J. Juryšek, A.F. Almansa, S. Victori, F. Maupin, C. Guirado-Fuentes, R. González, V. Vitale, P. Goloub, L. Blarel, L. Alados-Arboledas, E. Woolliams, S. Taylor, J.C. Antuña, M. Yela, Evaluation of night-time aerosols measurements and lunar irradiance models in the frame of the first multi-instrument nocturnal intercomparison campaign, Atmospheric Environment,Volume 202, 2019, Pages 190-211,ISSN 1352-2310, https://doi.org/10.1016/j.atmosenv.2019.01.006.

Doppler, L., Kazadzis, S., Kouremeti, N., Masoom, A., Barreto, A., Cuevas, E., Toledano, C., Roman, R., Campanelli, M., and Ritter, C.: Learnings of measurement campaigns in photometry instrumentation and inversion methods, a COST/HARMONIA study, EMS Annual Meeting 2023, Bratislava, Slovakia, 4–8 Sep 2023, EMS2023-656, https://doi.org/10.5194/ems2023-656, 2023.

Doppler, L., Masoom, A., Karanikolas, A.: Create a list of existing and foreseen campaigns or experiments needed for night and day aerosol measurements and report on the data collection and analysis of the data/measurements. Deliverable D1.1 of COST Action HARMONIA, Working Group 1., 2023.

Graßl, S.; Ritter, C.; Wilsch, J.; Herrmann, R.; Doppler, L.; Román, R. From Polar Day to Polar Night: A Comprehensive Sun and Star Photometer Study of Trends in Arctic Aerosol Properties in Ny-Ålesund, Svalbard. Remote Sens. 2024, 16, 3725. https://doi.org/10.3390/rs16193725

Herber et al., 2002. *Continuous day and night aerosol optical depth observations in the Artic between 1991 and 1999*. Journal of Geophysical Research 107 (D10), 4097 doi:10.1029/2001JD000536.

IPCC, 2021: *Climate Change 2021: The Physical Science Basis. Contribution of Working Group I to the Sixth Assessment Report of the Intergovernmental Panel on Climate Change*. Cambridge University Press, Cambridge, United Kingdom and New York, NY, USA, In press, doi:10.1017/9781009157896.

Kieffer, H. H. and Stone, T. C.: *The spectral irradiance of the moon*, Astronom. J., 129, 2887–2901, 2005.

Ivănescu, L., Baibakov, K., O'Neill, N. T., Blanchet, J.-P., and Schulz, K.-H.: Accuracy in starphotometry, Atmos. Meas. Tech., 14, 6561–6599, https://doi.org/10.5194/amt-14-6561-2021, 2021

Leiterer et al., 1995. *A new star photometer developed for spectral aerosol optical thickness measurements in Lindenberg*. Contributions to Atmospheric Physic s 68, 133–141.

Pérez-Ramirez et al., 2007, *Development and calibration of a star photometer to measure the aerosol optical depth: Smoke observations at a high mountain site*. Atm.Env 42, 2733-2738, doi:10.1016/j.atmosenv.2007.06.009

Román et al., 2020, *Correction of a lunar-irradiance model for aerosol optical depth retrieval and comparison with a star photometer.* Atmospheric Measurement Techniques, 13, 6293-6310, doi:10.5194/amt-13-6293-2020

Schmid, B., Wehrli, C., 1995. *Comparison of sun photometer calibration by use of the Langley technique and the standard lamp*. Applied Optics 34, 4500–4512.

Uchiyama et al., 2019, *Nocturnal aerosol optical depth measurements with modified sky radiometer POM-02 using the moon as a light source*, Atmos. Meas. Tech., 12, 6465–6488, https://doi.org/10.5194/amt-12-6465-2019, 2019.

2.2 The Cimel CE318 lunar model

Based on: "Nocturnal Aerosol Monitoring at Roque de los Muchachos high-altitude station: Lunar Product Comparison" presented at the European Meteorological Society Annual Meeting, Barcelona 8-12 September 2024. Authors: África Barreto, Roberto Román, Andrea Balotti, Claudia Frangipani, Miguel Ángel Gamonal, Daniel González-Fernández, Pablo González-Sicilia, Angelos Karanikolas, Simone Pulimeno, Cedric Busschots, and Stelios Kazadzis.

Lunar photometry is an emerging technique capable of filling the gaps in aerosol monitoring at night-time. This is particularly crucial in high latitudes and polar regions due to the prolonged absence of solar illumination. One of the most principal obstacles we encounter in monitoring aerosols at night-time using the Moon as a light source is the need for accurate extraterrestrial lunar irradiance due to the fast change of the Moon's illumination over time. The RIMO (ROLO Implementation for Moon's Observation; Barreto et al., 2019) model is an implementation of the ROLO (RObotic Lunar Observatory) model. RIMO was performed by the polar aerosol community to estimate the AOD at night-time, transferring the calibration of the solar channels to nocturnal measurements by means of the Sun-Moon gain factor method. A further correction of the RIMO model, the so-called RIMO correction factor (RCF), has served to improve the accuracy of the lunar product (Román et al., 2020). Similar approaches to correct the ROLO or RIMO biases have been developed by AERONET and SKYNET teams (Uchiyama et al., 2019).
In this study, we have used an 11-month dataset of day- and night-time photometric measurements taken with the CE318-TS photometer at Roque de Los Muchachos (RMO, La Palma, Canary Islands, Spain, 28.76°N, 17.89°W). This high-altitude observatory (2396 m above sea level) is an excellent location for astronomy and atmospheric observations. This site is characterized by pristine atmospheric conditions, with yearly mean Aerosol Optical Depth (AOD) at 500 nm <0.075. These conditions make RMO an excellent site for calibration and instrumental/product comparisons.

Lunar Algorithms
Accurate knowledge of extraterrestrial lunar irradiance is needed in lunar photometry to account for the complex illumination variations over the lunar cycle. The ROLO (RObotic Lunar Observatory, Kieffer and Stone, 2005) and the RIMO (ROLO Implementation for Moon's Observation; Barreto et al., 2019) models are the most widely used in the literature. Currently, two different methodologies have been developed specifically to retrieve the AOD at night with the CE318-TS, aiming to correct the inaccuracies observed in the previously mentioned lunar irradiance models concerning the Moon Phase Angle (MPA) over the lunar cycles:

- The RIMO correction factor (RCF) method: This method, published by Román et al. (2020), was developed using 98 pristine day-night-day transitions observed at the Izaña Observatory (Tenerife, Spain) as a second-order correction factor (dependent on MPA). When multiplied by the expected RIMO irradiance (E_{RIMO}) , it provides a more accurate extraterrestrial lunar irradiance ($E_{RIMO,corrected}$, Eq. -1).

  $$E_{RIMO,corrected,\lambda} = RCF_\lambda * E_{RIMO,\lambda} \qquad -1$$

  where,

  $$RCF_\lambda = a_\lambda + b_\lambda * MPA + c_\lambda * MPA^2 \qquad -2$$

- AERONET Lunar Product: This product was developed using pristine day-night-day transitions during the period 2015-2019 at Mauna Loa Observatory (Hawaii, USA) as a correction factor δ (linearly dependent on MPA or using a spline function) included in the Gain factor term (G, nominal value of 4096), which accounts for the difference in amplification between Sun and Moon measurements. This method is currently implemented in AERONET Version 3 (provisional product).

  $$G = Sky\ (Moon)/Sun\ = 4096 * (1 + \delta(MPA)) \ -3$$

Results

Coincident AERONET and RCF AOD lunar products at RMO corresponding to the time period between May 2023 and February 2024 were compared. Low mean AOD differences (AERONET vs RCF) were observed over the entire time period, with maximum values of -0.003 in the 500 nm spectral band, as observed in Table 2.2.1. These differences indicate that RCF provides systematically higher lunar AODs than the AERONET product.

Table 2.2.1: Averaged lunar AOD differences between AERONET and RCF.

Spectral Band (nm)	**1020**	**1640**	**870**	**675**	**440**	**500**
AOD difference	-0.002	-0.002	0.001	-0.001	-0.002	-0.003

Figure 2.2.1 shows the comparison of the two lunar AOD products during the lunar cycle in January 2024. Low AOD differences are observed in this specific lunar cycle, showing some spectral and lunar phase angle dependence. Higher differences are observed in the 1640, 1020, and 675 nm spectral bands during the first quarter, with minor deviation in the rest of the bands and MPAs.

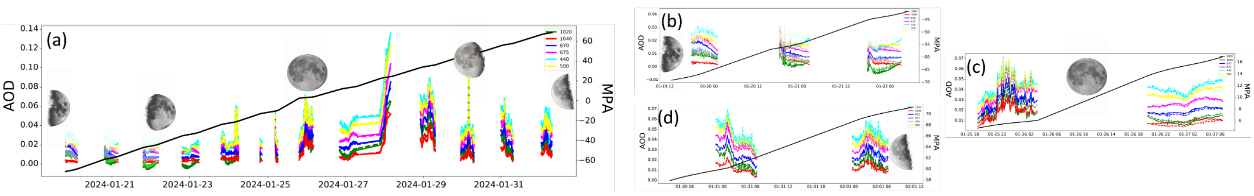

Figure 2.2.1: (a) Lunar AOD evolution with MPA for each CE318-TS spectral band (AERONET in solid colline or and RCF in ligh line) during the lunar cycle in January 2024, (b) near first quadrant, (c) during full Moon and (d) near last quarter.

A detailed analysis based on MPA over the entire period is shown in the boxplot in Figure 2.2.2. In this Figure, lower and upper boundaries for each box are the 25th and 75th percentiles; the solid line is the median value; the crosses indicate the outliers; and hyphens are the maximum and minimum values. Averaged differences greater than -0.004 are observed for all the spectral bands and MPA ranges, with the exception of maximum values up to -0.005 in the case of 1640, 1020, 500, and 440 nm at different MPA ranges. There is no clear dependence of these differences on the spectral band or the MPA.

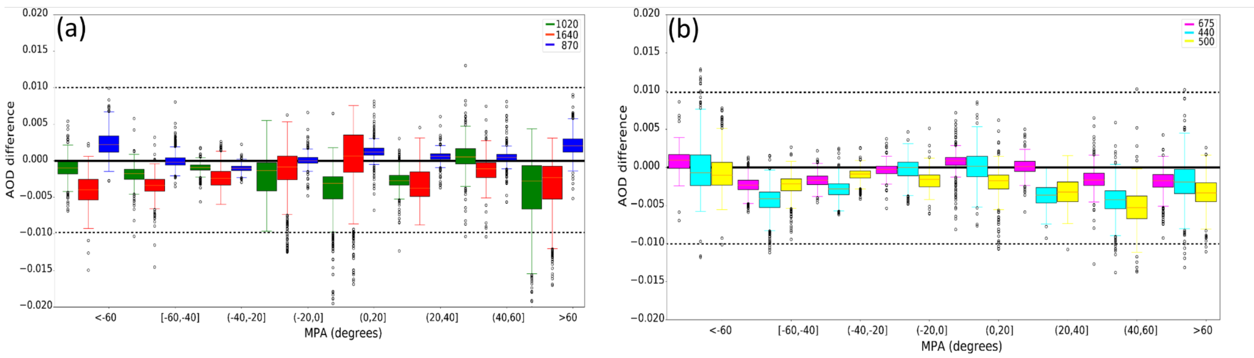

Figure 2.2.2: Boxplot of the AOD difference (AERONET versus RCF) with the MPA for the different CE318-TS spectral bands: (a) 1020, 1640 and 870nm, and (b) 675, 440 and 500nm.

Conclusions

We have shown that the two lunar AOD products (AERONET and RCF) provide similar information, with low differences within the accuracy limit of ±0.01 established in the AERONET network for daytime AOD in the visible spectral range. These results confirm that the two products are intercomparable despite the different approaches and datasets each one uses. These approximations involve a correction factor on ROLO/RIMO lunar irradiances linearly dependent on MPA in the case of AERONET and a second-order polynomial in the case of RCF as well as different versions of the lunar irradiance model (ROLO and RIMO, respectively).

References

Barreto, A., R. Román, E. Cuevas, D. Pérez-Ramírez, A.J. Berjón, N. Kouremeti, S. Kazadzis, J. Gröbner, M. Mazzola, C. Toledano, J.A. Benavent-Oltra, L. Doppler, J. Juryšek, A.F. Almansa, S. Victori, F. Maupin, C. Guirado-Fuentes, R. González, V. Vitale, P. Goloub, L. Blarel, L. Alados-Arboledas, E. Woolliams, S. Taylor, J.C. Antuña, M. Yela: Evaluation of night-time aerosols measurements and lunar irradiance models in the frame of the first multi-instrument nocturnal intercomparison campaign, Atmospheric Environment, Volume 202, Pages 190-211, ISSN 1352-2310, https://doi.org/10.1016/j.atmosenv.2019.01.006, 2019.

Uchiyama, A., Shiobara, M., Kobayashi, H., Matsunaga, T., Yamazaki, A., Inei, K., Kawai, K., and Watanabe, Y.: Nocturnal aerosol optical depth measurements with modified sky radiometer POM-02 using the moon as a light source, Atmos. Meas. Tech., 12, 6465–6488, https://doi.org/10.5194/amt-12-6465-2019, 2019.

Román, R., González, R., Toledano, C., Barreto, Á., Pérez-Ramírez, D., Benavent-Oltra, J. A., Olmo, F. J., Cachorro, V. E., Alados-Arboledas, L., and de Frutos, Á. M.: Correction of a lunar-irradiance model for aerosol optical depth retrieval and comparison with a star photometer,, Atmos. Meas. Tech., 13, 6293–6310, https://doi.org/10.5194/amt-13-6293-2020, 2020.

2.3 The Prede POM lunar model

Based on: "First AOD measurements obtained during night-time using lunar POM radiometer at Tor Vergata site (Italy)" presented at the European Meteorological Society Annual Meeting, Barcelona 8-12 September 2024. Authors: Gaurav Kumar, Monica Campanelli, Meritxell Garcia, Victor Estellés, Akihiro Uchiyama, Tsuneo Matsunaga, Akihiro Yamazaki, Annamaria Iannarelli, Stefano Casadio, Gabriele Mevi, and Nicola Ferrante.

Sun/sky radiometers have been used long and effectively to measure the aerosol radiative properties during daytime, using the sun as a powerful and stable light source. With the advancement in instrumentation, it has become possible to obtain data during nighttime using also the moon as a source of light. Although the moon's irradiance is not as powerful as the sun, it is very stable. Measurements at nighttime have advantages, but they also face some challenges. By using lunar photometers, we can obtain the data in places at higher latitudes, such as polar regions, where the sun does not appear for months. In regular places, where we can make daytime measurements, it helps us monitor the atmosphere during daytime and nighttime. Apart from this, during nighttime the temperature is relatively more stable and lower than during the daytime, which reduces the signal noise due to temperature changes. Some of the challenges, however, are proper calibration and low signal-to-noise ratio. Moon changes its phase every day, making the calibration calculation very challenging. Another problem is the low signal-to-noise ratio at short wavelengths. However, Uchiyama et al. (2019) have shown that the instrument can fully obtain good quality data during nighttime at wavelengths above 400 nm.

The present study, conducted at Tor Vergata site near Rome (Italy), aims to showcase the effectiveness of nighttime measurements in obtaining aerosol optical properties using a PREDE lunar radiometer model POM02L. In this study, we present the methodology of AOD calculation, calibration methodology, and validation during the Izana and QUATRAM3 field campaigns. Finally, we present the comparison analysis at Tor Vergata.

Methodology

The method of AOD retrieval during the nighttime is similar to that used for daytime measurement. We start with the Beer's law:

$T = T_0 exp(-\tau 1)$ -1

Since the sensor output (in A) is directly proportional to the transmittance T, we can write it as

$V = V_0 exp(-\tau 1)$ -2

Where V_0 is the calibration, and τ1 is the total optical depth.
The irradiance reached from the moon is reflected on its surface. Due to the bright and dark patches on its surface, the reflectance is not uniform. To get an uniform reflectance, we use the ROLO model. This model was developed by Kieffer and Stone (2005) using around 85000 high-resolution images of the moon taken for 8 years. However, as indicated by previous authors (Barreto et al. 2016, 2017, 2019; Jurysek and Prouza, 2017), an error is associated with using the ROLO reflectance. However, this error is due to ROLO reflectance being proportional to the ROLO reflectance; relative variation of the ROLO reflectance is assumed correct (Uchiyama et al 2019):
A_{ROLO}=CA_{ROLO} -3
After incorporating the corrected uniform reflectance, we get:

$$V = CA_{ROLO}\frac{V_{S0}}{\pi R_m^2 R_S^2}\Omega_M exp(-m\tau T_{gas}) \qquad -4$$

Where, A_{ROLO} is the ROLO reflectance and C is a proportionality constant (due to error in ROLO), R_S is the distance between the sun and the moon in astronomical units, R_m is the distance between the moon and the observer (normalised by 384400 km), V_{S0} is the calibration value obtained from direct sun measurements, T_{gas} is the transmittance due to gas absorption, m is the optical air mass, τ is the aerosol optical depth and Ω_M is the solid angle of the moon.

Algorithm

To retrieve the AOD from the raw signal, we have used the modified version of the Sunrad package (Estelles et al., 2012). The original package retrieves the AOD from the raw signal from the Sun/sky radiometer. The package has been modified to ingest the Lunar data format and retrieve the AOD. The cloud screening algorithm remains the same as the original Sunrad package (Smirnov et al., 2001; Estelles et al., 2012). Level 1.5 data from AERONET is still in the provisional stage. We do not have complete information about the specific algorithm used by AERONET to process the Lunar data.

Calibration

The calibration method for a Sun/sky radiometer is very straightforward. We take the instrument to a pristine environment at a high altitude and perform the method known as standard Langley. We can find the calibration by calculating the intercept of fit of Log F and 1/m, where F is the raw signal and m is the optical air mass. Alternatively, the Improved Langley Plot (ILP) method developed in the SKYNET network can also be used to calculate the calibration onsite. When it comes to Lunar data, the Langley method becomes difficult because of the changing phase of the moon. The ILP method cannot be applied because of the very low signal-to-noise ratio of sky radiance data. It is essential to get an alternative methodology to find the calibration accurately. Uchiyama et al. (2019) provided an alternative methodology for finding the calibration value onsite without using the Langley method. For this they sent a PREDE POM02L to the Mauna Loa observatory from 28th September to 7th November to get the Langley plots. They calculated the calibration using the following method:
Rewriting the equation 4 (assuming no gaseous absorption), we get:

$$ln(\frac{V\pi R_m^2 R_S^2}{A_{ROLO}\Omega_M}) = lnCV_{S0} - m\tau \qquad -5$$

We can calculate intercept as V_{m0}=CV_{s0} -6

$C = \frac{V_{m0}}{V_{S0}}$ -7

Later, they found the quadratic relationship between C and the phase angle of the moon (g, in degrees).

$C = A_c.g^2 + B_c$ -8

Then they found the fit parameters A_c and B_c by performing the fit between C and g^2. Since, these coefficients are proportional to square of moon phase angle, we believe these are nearly constant for all the PREDE instruments. Therefore, in a first approach we adopted the same coefficients and calculated the calibration value of our instrument.

Validation

We compared the AOD obtained from lunar data measured by a PREDE POM01L against the AERONET level 1.5 dataset to validate our retrievals for QUATRAM3 and Izana campaigns. The results are shown below. Data within 10 seconds between AERONET and PREDE data are used for this validation.

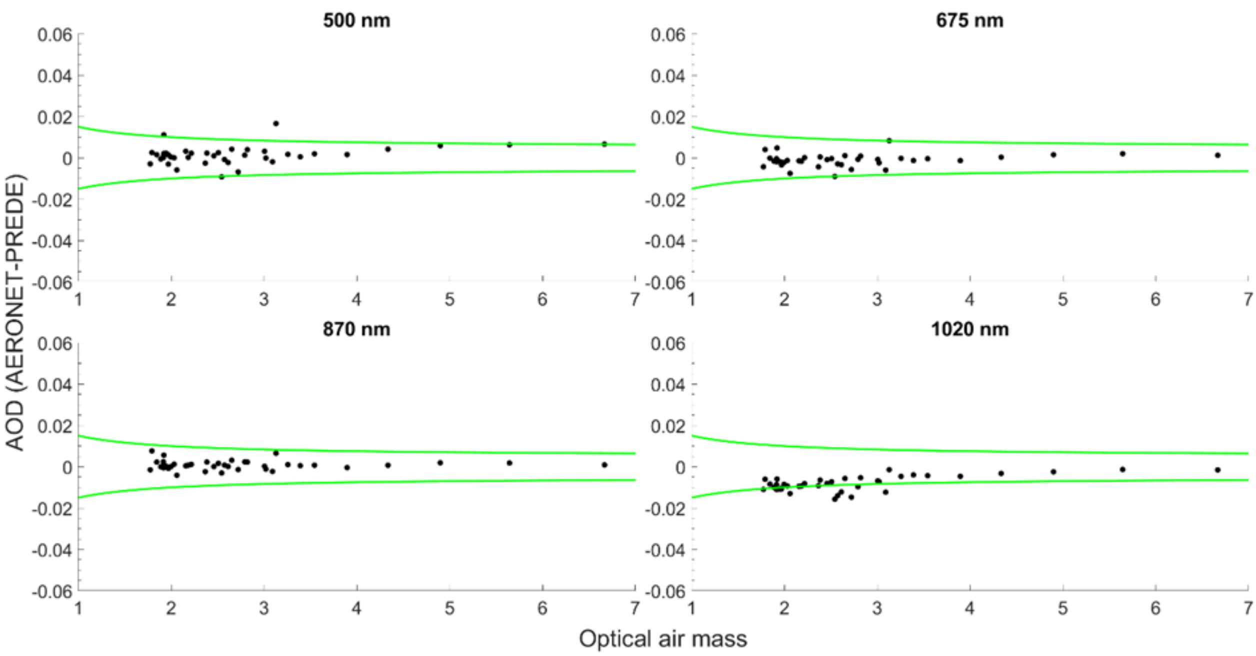

Figure 2.3.1- WMO Plot of differences between AERONET and PREDE during the QUATRAM3 campaign. The green lines show the WMO limits (0.01/m±0.005)

COST EUROPEAN COOPERATION IN SCIENCE & TECHNOLOGY
Funded by the European Union

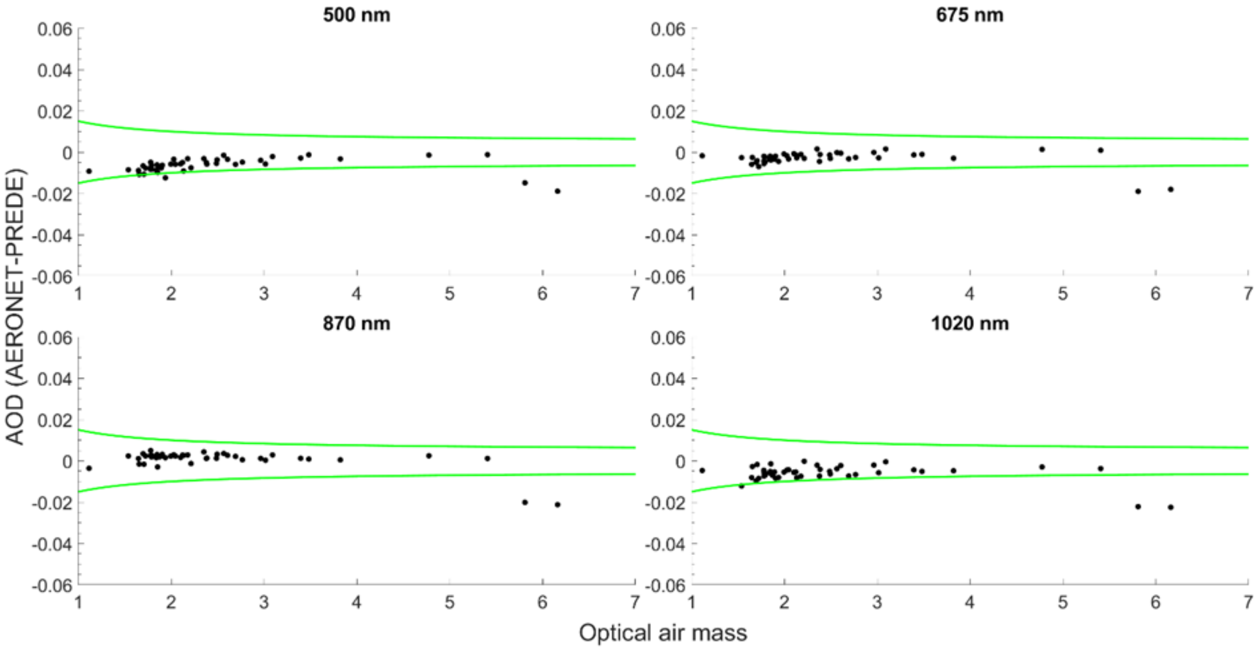

Figure 2.3.2 WMO Plot of differences between AERONET and PREDE during the Izana campaign. The green lines show the WMO limits (0.01/m±0.005)

The plots obtained from the Izana and the QUATRAM campaigns show very good agreement. A comparison for four wavelengths agrees with WMO guidelines (0.01/m±0.005, where m is the optical airmass) represented in the figure as green lines.

	Rome				Izana				
	500 nm	675 nm	870 nm	1020 nm	500 nm	675 nm	870 nm	1020 nm	
Mean	0.1762	0.1392	0.1189	0.1065	0.0414	0.0365	0.0344	0.0282	AERONET
Median	0.1448	0.1131	0.0943	0.0839	0.0359	0.0310	0.0282	0.0333	
STD	0.0877	0.0687	0.0597	0.0553	0.0232	0.0215	0.0214	0.0225	
Mean	0.1748	0.1404	0.1181	0.1146	0.0501	0.0416	0.0356	0.0359	PREDE

Median	0.1420	0.1144	0.0927	0.0916	0.0500	0.0407	0.0375	0.0388	
STD	0.0897	0.0702	0.0602	0.0576	0.0218	0.0203	0.0198	0.0217	
MBD	0.0014	-0.0012	0.0008	-0.0081	-0.0064	-0.0031	0.0007	-0.0061	
RMSD	0.0046	0.0033	0.0024	0.0089	0.0073	0.0049	0.0049	0.0074	

Table 2.3.1- Statistical analysis at Rome and Izana campaigns

The statistical analysis of the comparison also showed exceptional agreement with AERONET. Comparisons at both Izana and Rome are shown in Table 2.3.1. The maximum RMSD is 0.0089 at 1020 nm in Rome, and 0.0074 at 1020 nm in Izana. The standard deviation (STD), mean and median values of AOD in PREDE at all four common wavelengths (500, 675, 870 and 1020 nm) are almost identical to the values from AERONET.

Comparison at Tor Vergata

Tor Vergata is a permanent site in Rome, Italy. It is ~25 km from the Rome city centre. Because of its close proximity to Rome, we expect the AOD to be similar to that of Rome. A lunar PREDE POM02L is collocated with the Lunar CE318 Cimel from AERONET. Four channels, namely 500, 675, 870, and 1020 nm, are common for comparison. Both the instruments rely on the ROLO model to obtain uniform reflectance from non-uniform lunar surfaces. A period of 7 months is used to perform the comparison. PREDE level 2 data within 30 seconds is used for the comparison analysis.

Results

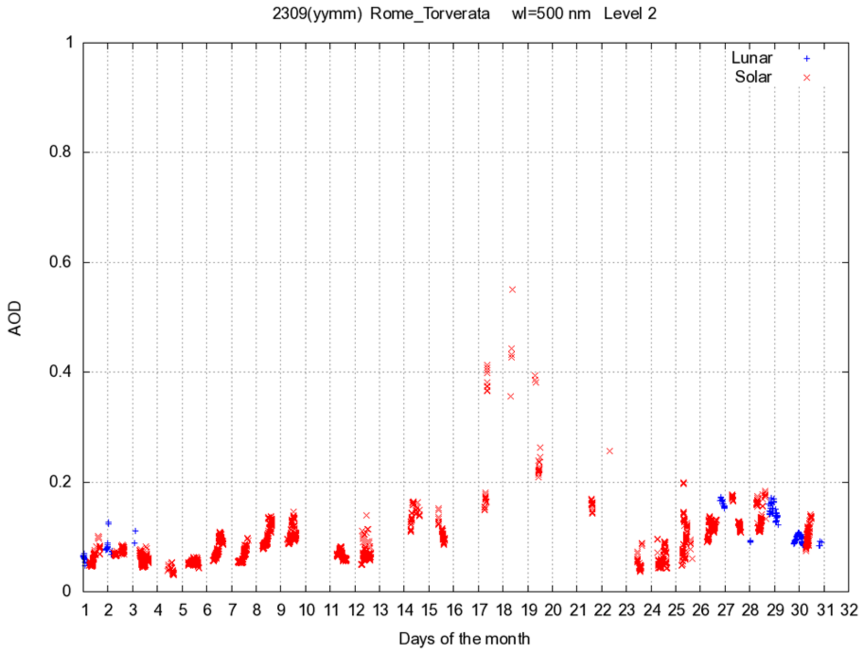

Figure 2.3.3 Overlay plot of solar and lunar data in Tor Vergata. The blue stars show the lunar data and the red star shows the solar data at the site on different days.

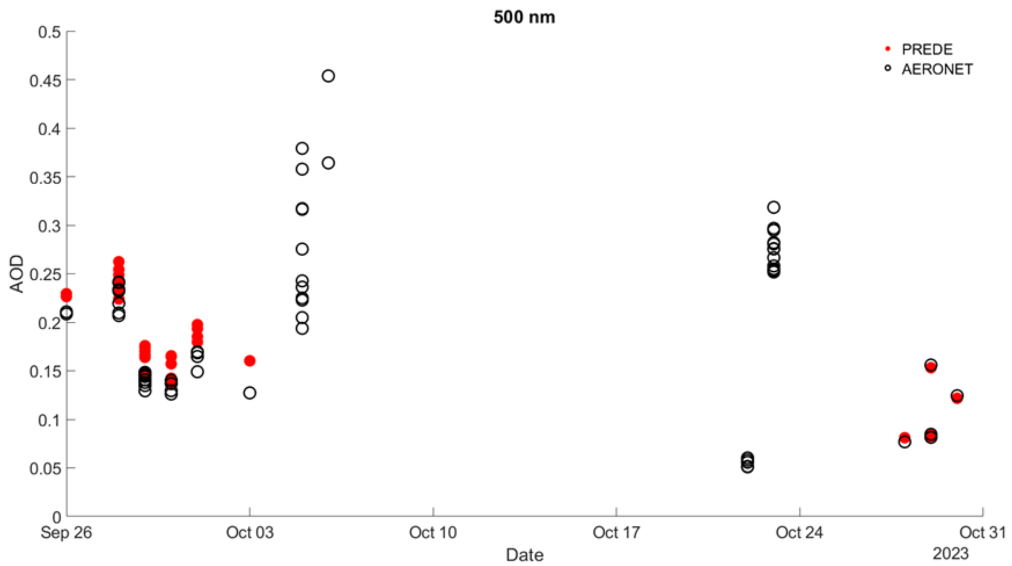

Figure 2.3.4 AOD comparison of AERONET and PREDE from August 2023 to February 2024 at Tor Vergata. The open circles represent AERONET data and the red circles represent PREDE data.

Table 2.3.2. Statistics of the comparison at the Tor Vergata

	500 nm	675 nm	870 nm	1020 nm

Mean	0.1768	0.1157	0.0844	0.0797
STD	0.0096	0.0062	0.0048	0.0086
RMSD	0.0036	0.0026	0.0018	0.0038

Figure 2.3.3 shows the overlay plot of both solar and lunar AOD at Tor Vergata site. This plot shows the continuity of the solar data and the lunar data. It also shows the effectiveness in filling the data gap during nighttime. Figure 2.3.4 is the time series of the AOD of PREDE and AERONET. We see that the AOD calculated by PREDE is close to AERONET lunar AOD.

Table 2.3.2 shows the standard deviation (STD), root mean square deviation (RMSD) and mean AOD. In Table 2.3.1, we can see a good comparison between the data retrieved from the two instruments. The RMSD is as low as 0.0018 at 870 nm, and the maximum is 0.0038 at 1020 nm, which is a good comparison. For the comparison months (September 2023 and October 2023), we obtained the mean and standard deviation of AOD at 500 nm from the climatology tables provided by AERONET website: the mean and STD of AOD at 500 nm during daytime during September and October are 0.182, 0.170 and 0.103, 0.100. These values are almost similar to those measured by the PREDE radiometer (0.1768 and 0.0096 respectively) during nighttime at 500 nm.

Conclusions

This study is the first to compare the lunar AOD between PREDE and AERONET at Tor Vergata site. Low RMSD and identical mean and standard deviation of the lunar data from PREDE to Solar data of AERONET shows very good agreement.

So far, we are using similar cloud screening for solar and lunar data, although we expect to update the cloud screening method for lunar data in the future. We also plan to investigate the calibration coefficients given by Uchiyama et. al (2019) in the future.

References

A. Smirnov, B.N. Holben, T.F. Eck, O. Dubovik, I. Slutsker, Cloud-Screening and Quality Control Algorithms for the AERONET Database, Remote Sensing of Environment, Volume 73, Issue 3, 2000, Pages 337-349, ISSN 0034-4257, https://doi.org/10.1016/S0034-4257(00)00109-7.

Barreto, Á., Cuevas, E., Granados-Muñoz, M.-J., Alados- Arboledas, L., Romero, P. M., Gröbner, J., Kouremeti, N., Almansa, A. F., Stone, T., Toledano, C., Román, R., Sorokin, M., Holben, B., Canini, M., and Yela, M.: The new sun-skylunar Cimel CE318-T multiband photometer – a comprehensive performance evaluation, Atmos. Meas. Tech., 9, 631–654, https://doi.org/10.5194/amt-9-631-2016, 2016.

Barreto, Á., Román, R., Cuevas, E., Berjón, A. J., Almansa, A. F., Toledano, C., González, R., Hernández, Y., Blarel, L., Goloub, P., Guirado, C., and Yela, M.: Assessment of nocturnal aerosol optical depth from lunar photometry at the Izaña high mountain observatory, Atmos. Meas. Tech., 10, 3007–3019, https://doi.org/10.5194/amt-10-3007-2017, 2017.

Barreto, A., Román, R., Cuevas, E., Pérez-Ramírez, D., Berjón, A. J., Kouremeti, N., Kazadzis, S., Gröbner, J., Mazzola, M., Toledano, C., Benavent-Oltra, J. A., Doppler, L., Juryšek, J., Almansa, A. F., Victori, S., Maupin, F., Guirado-Fuentes, C., González, R., Vitale, V., Goloub, P., Blarel, L., Alados- Arboledas, L.,Woolliams, E., Taylor, S., Antuña, J. C., and Yela, M.: Evaluation of night-time aerosols measurements and lunar irradiance models in the frame of the first multi-instrument nocturnal intercomparison campaign, Atmos. Environ., 202, 190–211, https://doi.org/10.1016/j.atmosenv.2019.01.006, 2019.

Estellés, V., Campanelli, M., Utrillas, M. P., Expósito, F., and Martínez-Lozano, J. A.: Comparison of AERONET and SKYRAD4.2 inversion products retrieved from a Cimel CE318 sunphotometer, Atmos. Meas. Tech., 5, 569–579, https://doi.org/10.5194/amt-5-569-2012, 2012.

Juryšek, J. and Prouza, M.: Sun/Moon photometer for the Cherenkov Telescope Array – first results, Proceedings of Science, 35th International Cosmic Ray Conference-ICRC2017, 10–20 July, 2017 Bexco, Busan, Korea, 2017.

Kieffer, H. H. and Stone, T. C.: The spectral irradiance of the moon, Astronom. J., 129, 2887–2901, 2005.

Uchiyama, A., Shiobara, M., Kobayashi, H., Matsunaga, T., Yamazaki, A., Inei, K., Kawai, K., and Watanabe, Y.: Nocturnal aerosol optical depth measurements with modified sky radiometer POM-02 using the moon as a light source, Atmos. Meas. Tech., 12, 6465–6488, https://doi.org/10.5194/amt-12-6465-2019, 2019

2.4 Evaluation of current lunar techniques: application to Valencia (Spain) site

Based on the HARMONIA project #21: "Solar and lunar AOD comparison at Valencia during years 2015-2024". Authors: Meritxell Garcia-Suñer and Víctor Estellés.

The emerging field of photometric measurements employing the Moon as a light source has attracted the interest of a considerable number of researchers. In particular, the potential of this technique lies in its usefulness in ensuring near-continuous monitoring of aerosol properties when coordinated with a sun photometer. Indeed, lunar photometers can provide irradiance measurements in regions where long periods of darkness are common, especially in the Arctic region.

A brief study focused on the analysis of the Aerosol Optical Depth at 440 nm (AOD_{440}), the Ångström Exponent ($\alpha_{440-870}$) and the columnar water vapor (CWV) from the solar and lunar photometers installed at the AERONET site in Burjassot (Valencia) is performed. In particular, the nocturnal Level 1.5 (July 2015 to May 2024) and diurnal Level 2.0 (July 2015 to October 2023) retrievals from AERONET are analysed. This analysis can be divided into two parts.

First, a climatological study of both solar and lunar retrieved AOD_{440}, $\alpha_{440-870}$ and CWV is carried out. In particular, their corresponding hourly, daily, monthly and annual solar and lunar means are computed and plotted over time. Then, the inter-annual behaviour of these magnitudes is studied. For completeness, the evolutions of the annual AOD_{440}, $\alpha_{440-870}$ and CWV medians are examined so as to identify possible increasing/decreasing trends. Finally, the continuity of the instantaneous nocturnal and diurnal measurements of AOD_{440} is tested based on some case studies.

Then, the discrepancies between nearests solar and lunar retrievals are analyzed. For this purpose, several quality filters are applied in order to determine to what extent the agreement between the two data sets improves.

The most relevant results are summarized hereafter.

1.1 Climatological study.

- Determination of AOD_{440}, $\alpha_{440-870}$ and CWV means

AOD_{440} and CWV means present a similar seasonal pattern, as shown in Figures 2.4.1a and 2.4.1b, respectively. Indeed, these magnitudes reach their maximum in summer months, whereas minimums are found in winter. Conversely, this behaviour cannot be distinguished for $\alpha_{440-870}$. The maxima in CWV can be attributed to the fact that solar irradiance is more intense in summer than in winter, thus increasing air temperature and favouring evaporation and storage. On the other hand, these higher solar irradiance intensities, together with the characteristic absence of rainfall and the increased occurrence of dust intrusions affecting the region, favour particle stagnation and growth, and therefore higher turbidities. The mixing of coarse particles conveyed by dust outbreaks with anthropogenic fine particles from local emissions could explain the non-existence of a clear seasonal pattern for $\alpha_{440-870}$. It is important to notice the agreement between solar and lunar means, especially in the case of the CWV, although the consistency between them will be assessed later.

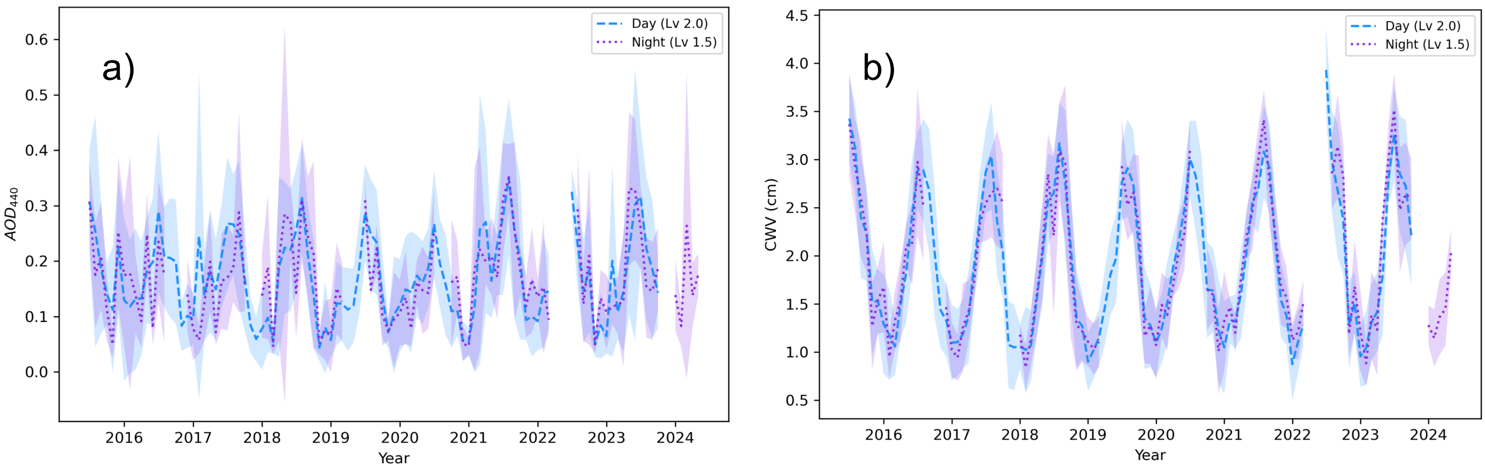

Figure 2.4.1: Evolution of monthly a) AOD_{440} and b) CWV means over time, based on solar (blue) and lunar (purple) data. The shadows depict the standard deviation of data points. Note the data gap in 2022, which is due to instrumentation problems.

o <u>Inter-annual behaviour</u>

The seasonal patterns of AOD_{440} and CWV discussed in the previous section are more clearly identified when the intra-annual evolution of these magnitudes is studied, as seen in Figures 2.4.2a and 2.4.2b. The maximum values of AOD_{440} and CWV are found in July, although secondary maxima can be identified in February and April (solar)/May (lunar). These maxima may be related to the occurrence of occasional but intense dust outbreaks that usually occur in spring.

Regarding the $\alpha_{440-870}$, as it has been previously mentioned, no pattern can be identified, probably because the presence of fine particles is dominant throughout the year.

In general, retrievals from lunar irradiance describe more dispersion than those using the Sun as light source. This is clearly shown in Table 2.4.1, especially when comparing the standard deviation associated with the obtained AOD_{440}. This higher dispersion could be explained by the difficulties encountered in lunar photometry (the lunar irradiance is not stable throughout the night, the Moon's surface is not uniform, and the cloud screening algorithm still needs to be optimised, Román et al. (2020)), as well as the fact that there are fewer lunar measurements, since these are only collected when the irradiance is high enough (i.e. from the first to the three quarters of the Moon).

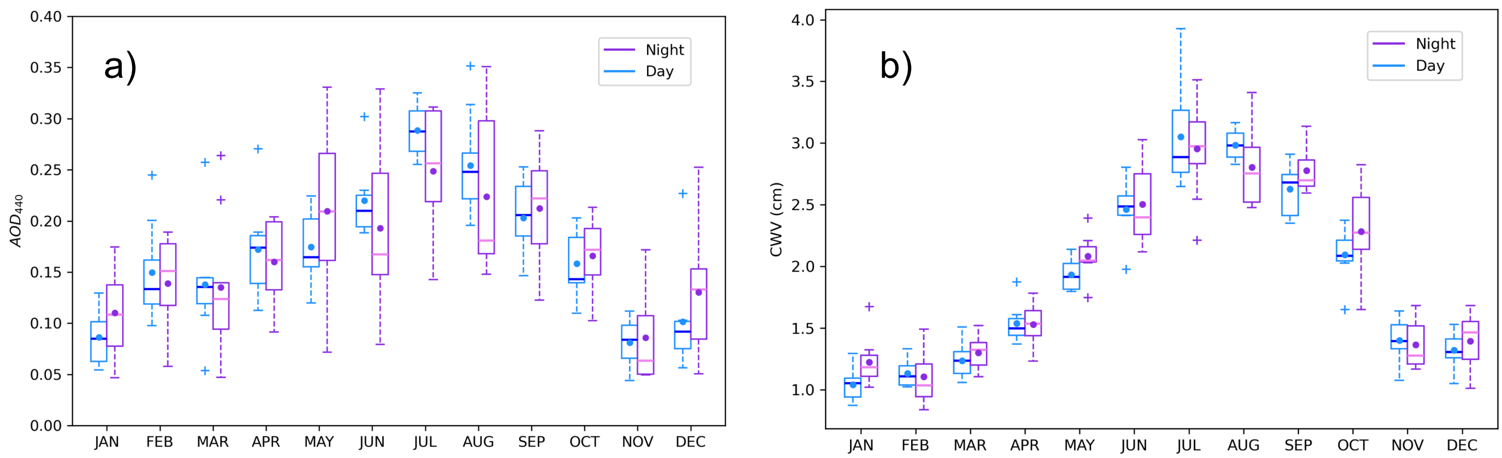

Figure 2.4.2: Boxplots showing a) $AOD_{440}$and b) CWV means for each month computed using the data from July 2015 to May 2024 (lunar data, in blue colour) and from July 2015 to October 2023 (solar data, in purple colour).

Table 2.4.1: Statistic parameters that quantify the inter-annual day/night behaviour for AOD_{440}. AOD_{440} represents the mean, σ the corresponding standard deviation, $< AOD_{440} >$ the median, U5 and U95 the

5th and 95th percentiles, respectively, N the number of days and M the number of months with available data.

	AOD_{440}	$\sigma(AOD_{440})$	$< AOD_{440} >$	$U5$	$U95$	N	M
JAN	0.09 / 0.11	0.03 / 0.04	0.08 / 0.11	0.06 / 0.05	0.13 / 0.16	190 / 80	8 / 9
FEB	0.15 / 0.14	0.05 / 0.05	0.13 / 0.15	0.10 / 0.07	0.23 / 0.19	164 / 58	8 / 9
MAR	0.14 / 0.14	0.06 / 0.07	0.14 / 0.12	0.07 / 0.06	0.22 / 0.25	198 / 82	8 / 9
APR	0.17 / 0.16	0.05 / 0.04	0.17 / 0.16	0.12 / 0.10	0.25 / 0.20	216 / 79	7 / 7
MAY	0.17 / 0.21	0.04 / 0.09	0.16 / 0.21	0.13 / 0.09	0.22 / 0.32	243 / 74	7 / 7
JUN	0.22 / 0.19	0.04 / 0.09	0.21 / 0.17	0.19 / 0.09	0.28 / 0.31	213 / 73	7 / 6
JUL	0.29 / 0.25	0.02 / 0.06	0.29 / 0.26	0.26 / 0.15	0.32 / 0.31	190 / 68	9 / 8
AUG	0.25 / 0.22	0.05 / 0.08	0.25 / 0.18	0.20 / 0.15	0.34 / 0.34	174 / 67	9 / 8
SEP	0.20 / 0.21	0.04 / 0.06	0.21 / 0.22	0.15 / 0.13	0.25 / 0.28	154 / 67	9 / 7
OCT	0.16 / 0.17	0.03 / 0.04	0.14 / 0.17	0.12 / 0.11	0.20 / 0.21	175 / 101	9 / 8
NOV	0.08 / 0.09	0.03 / 0.05	0.08 / 0.06	0.05 / 0.05	0.11 / 0.16	170 / 101	8 / 6
DEC	0.10 / 0.13	0.05 / 0.07	0.09 / 0.13	0.06 / 0.06	0.18 / 0.23	187 / 108	8 / 7
TOTAL	0.17 / 0.17	0.04 / 0.06	0.16 / 0.16	0.13 / 0.09	0.23 / 0.25	2274 / 958	97 / 91

- Temporal evolution

Although a proper analysis of the evolution of a given quantity over time requires at least 10 years of data, in this section a brief study on the evolution of AOD_{440}, $\alpha_{440-870}$ and CWV is carried out in order to identify possible trends for these quantities. This analysis is based on the annual medians (as they are less sensitive to variations with respect to the means) of these magnitudes computed for the daytime (~8 years) and nighttime (~9 years) data set. These data points are fitted based on the linear regression method, so that the sign and magnitude of the slope of the fitted line provide information on the nature of the trend. A more robust analysis, based on the seasonal Mann-Kendall test and Sen's slope (Mann (1945), Kendall (1975), Sen (1968)), can be employed in order to assess the significance of trends and quantify them, respectively. However, these methods require at least 10 data samples (i.e. years) to be performed reliably. Therefore, they are applied but the corresponding results are considered preliminary.

The results of the linear regression analysis are shown in Tables 2.4.2a and 2.4.2b for the solar and lunar data, respectively. In general, all three magnitudes show a decreasing behaviour in both cases. This is in agreement with the significant decrease of AOD and α found by Li et al. (2014) in Europe. According to the Mann-Kendall test, the decrease in $\alpha_{440-870}$ is statistically significant at 5 (solar)/4 (lunar) over the 12 months. However, it is important to remark that these results are not definitive, as a larger dataset is required. Indeed, as can be seen in Tables 2.4.2a and 2.4.2b, the R^2 are generally $<< 1$, thus indicating the poorness of the fit and the need for further research based on more sophisticated methods.

Table 2.4.2: Parameters resulting from the linear regression analysis ($y = ax + b$) of the annual AOD_{440}, $\alpha_{440-870}$ and CWV medians computed from the a) day and b) night retrievals. The values of the slope are expressed as a · 10^3 (units/year).

a)

	AOD_{440}			$\alpha_{440-870}$			CWV		
Seas	**a**	**b**	**R²**	**a**	**b**	**R²**	**a (cm/year)**	**b (cm)**	**R²**
SPR	4	-8	0.15	-40	80	0.4	0.16	1.4	$4\cdot10^{-6}$
SUM	3	-6	0.09	-18	40	0.3	20	-40	0.4
AUT	-0.07	0.2	$6\cdot10^{-5}$	- 60	110	0.4	40	-80	0.3
WIN	-5	9	0.18	-20	40	0.3	-30	60	0.4
TOT	-0.5	1.1	0.003	-40	70	0.6	-20	40	0.05

b)

	AOD_{440}			$\alpha_{440-870}$			CWV		
Seas	**a**	**b**	**R²**	**a**	**b**	**R²**	**a (cm/year)**	**b (cm)**	**R²**
SPR	5	-11	0.2	-80	160	0.6	60	-130	0.2
SUM	1.5	-3	0.01	-20	40	0.7	20	-40	0.05
AUT	5	-9	0.17	-40	80	0.19	100	-190	0.3
WIN	-8	16	0.12	13	-30	0.03	-20	40	0.13
TOT	-2.6	5	0.09	-53	100	0.6	-30	60	0.05

- <u>Day-night continuity of AOD_{440} based on instantaneous measurements</u>

An immediate way to graphically visualise the continuity of daytime and nighttime retrievals is to plot instantaneous data points and observe their behaviour at the day-night transition. Figure 2.4.3 depicts instantaneous AOD_{440} from 10 to 20 August 2022. This time period is chosen according to a reported dust intrusion event. These phenomena are generally associated with a higher AOD_{440}, which facilitates the comparison. As can be observed, the day-night transition is rather smooth (see, for example, 12-13, 14-15, 15-16, 17-18 August). However, some discrepancies can be detected (12-13, 19-20 August). Further research is needed to assess the cause of these inconsistencies. However, it can be hypothesised that these discrepancies could be related to the presence of clouds. This hypothesis will be analysed in the near future, as there are instruments installed at the Burjassot station able to monitor the passage of clouds.

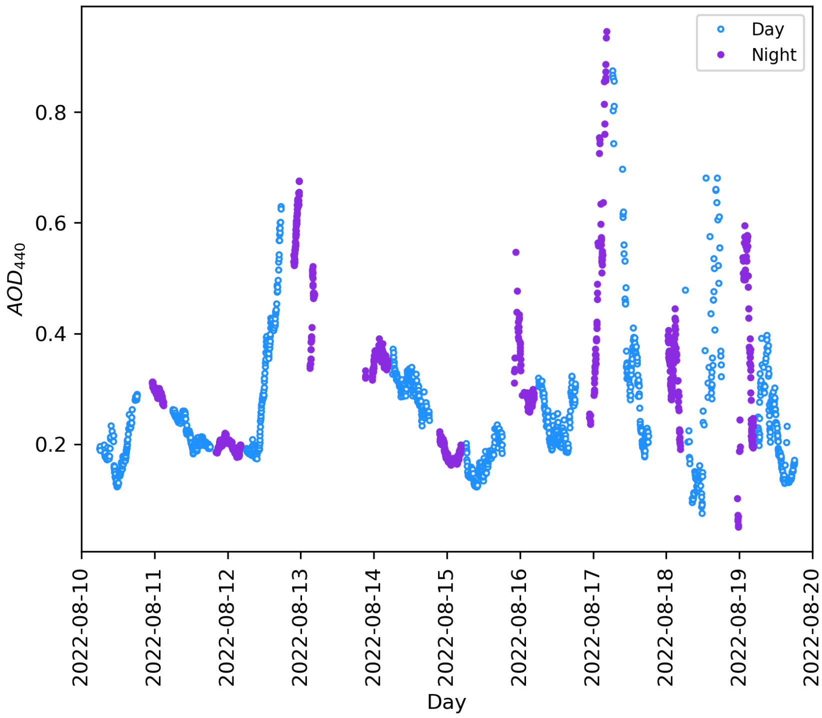

Figure 2.4.3: Instantaneous daytime and nighttime AOD_{440} measurements from 10 to 20 August 2022, when a dust intrusion episode occurred.

1.2 Solar and lunar measurements consistency.

In this section, the agreement between simultaneous daytime and nighttime measurements of AOD_{440}, $\alpha_{440-870}$ and CWV is evaluated. The aim of this analysis is to gain a better understanding of the characteristics of the dataset. For this purpose, the measurements of AOD_{440}, $\alpha_{440-870}$ and CWV are filtered according to different criteria. Then, the means of daytime and nighttime data points differing less than 30 minutes from the day-night transition are computed. The resulting pairs are included in a scatter plot in order to assess the day-night correlation, as shown in Figure 2.4.4. The most relevant criteria that have been applied are:

- Time difference:

This criterion works on the basis of the nocturnal data set by finding the minimum time difference for each edge night measurement (defined as both the first and the last measurements collected for each night) with respect to the edge values from the diurnal set of data. Then, if this minimum time difference is $\Delta t \leq 2.5\,h = 9000\,s$, measurements corresponding to this day will be kept for both data sets. Hence, for a certain day, the time difference between diurnal and nocturnal measurements must be less than 2.5 hours. This filter ensures data continuity and helps to avoid sharp variations in the magnitudes related to their evolution over time. Thus, it contributes to eliminating data dispersion. Compared to the other filters applied, it is the one that provides the greatest data consistency.

- Data dispersion:

It consists of setting a threshold value of 0.02 for the standard deviation of both daytime and nighttime AOD_{440} measurements. This filter sets a better scenario for the comparison by selecting relatively stable days and nights, without large variations of AOD_{440}. This way, it removes the largest values of AOD_{440} and CWV, as well as the largest dispersions in the interval $0.1 \leq AOD_{440} \leq 0.2$.

- Moon phases:

A filter considering Moon phases is also applied to the nocturnal data set. The aim is to select only those data points that have been measured under large enough lunar irradiances, in an attempt to reduce the uncertainties associated with the measurement. Hence, only those data points that correspond to a time period ranging from 4 days after the first quarter to 4 days before the last quarter are kept. In addition, those days when eclipses took place are also removed. This criterion discards data points associated with higher dispersion, especially those $AOD_{night} > AOD_{day}$ in the interval $0 < AOD_{440} < 0.6$. Moreover, it removes measurements corresponding to the highest nocturnal $\alpha_{440-870}$. Thus, the correlation between daytime and nighttime $\alpha_{440-870}$ is greatly improved, as this criterion eliminates AOD_{440} measurements performed under low lunar irradiances, resulting in larger uncertainties. Furthermore, the largest divergences in $\alpha_{440-870}$ correspond to notably larger nocturnal $\alpha_{440-870}$, generally associated with low AOD_{440} values.

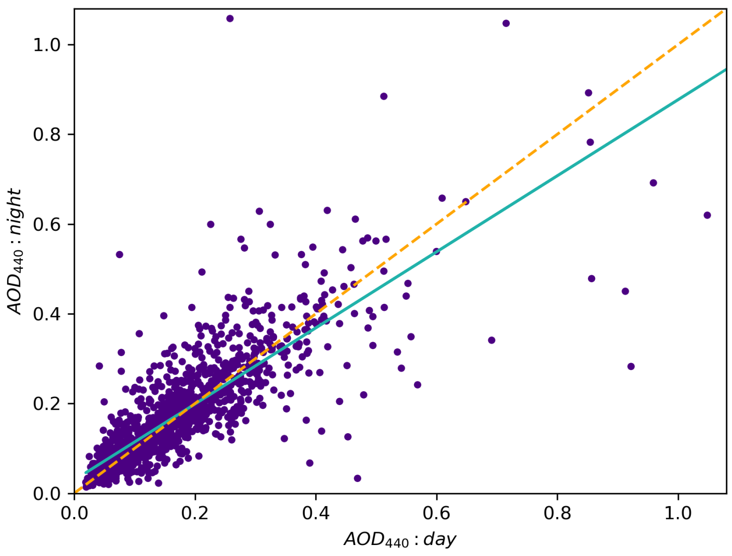

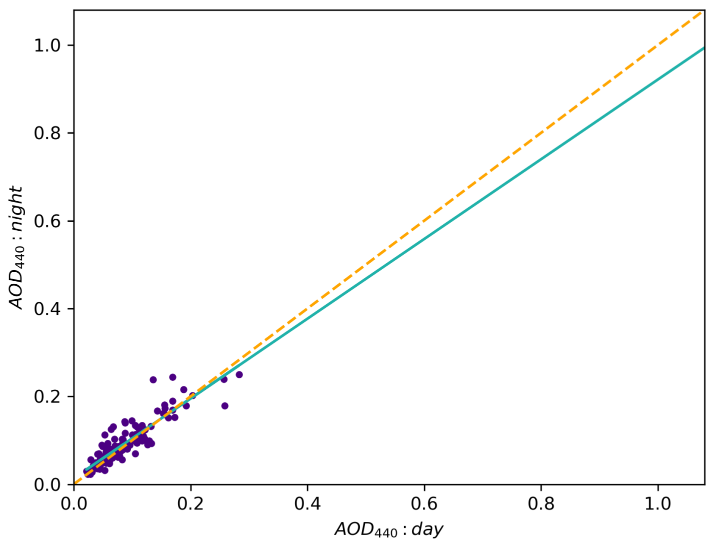

cost
EUROPEAN COOPERATION
IN SCIENCE & TECHNOLOGY
Funded by
the European Union

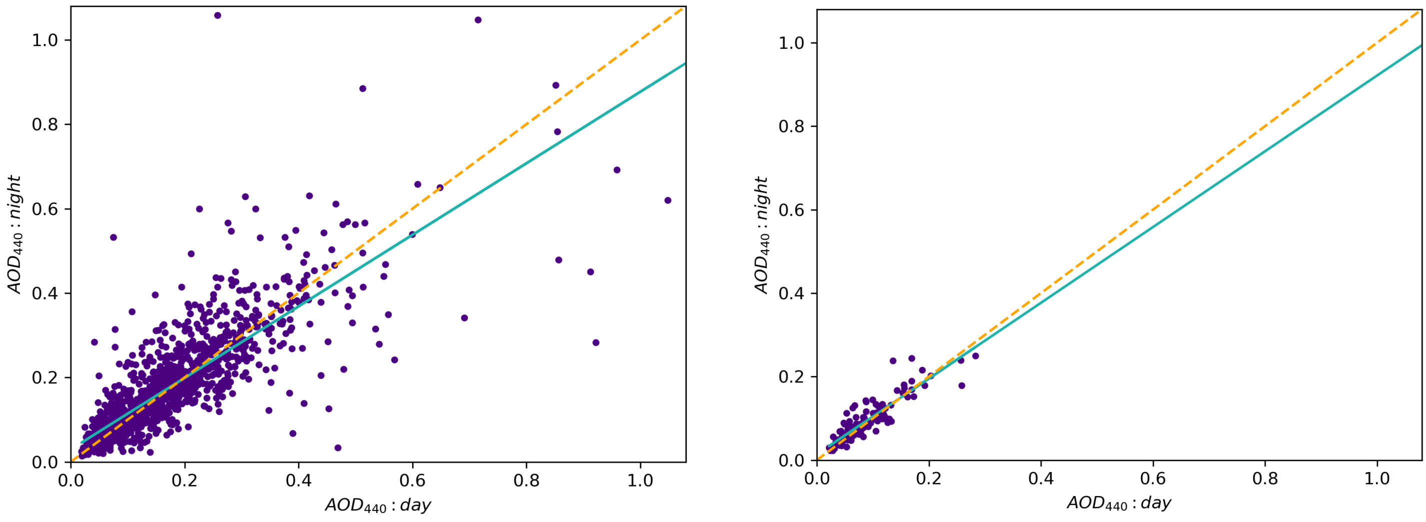

Figure 2.4.4: Day-night validation of AOD_{440}. Dots represent $\Delta t = 30\ min$ means. The scatter plot on the left corresponds to the case when no filters are applied (N = 1402), being $AOD_{night} = 0.85\ AOD_{day} + 0.03$ ($R^2 = 0.69$) the equation corresponding to the linear fit of the points. On the right, the scatter plot that results when the time difference and the data dispersion criteria are jointly applied (N = 130). The corresponding linear fit is described by the equation $AOD_{night} = 0.91\ AOD_{day} + 0.01$ ($R^2 = 0.80$).

To sum up, climatological studies performed from diurnal and nocturnal measurements yielded similar conclusions. In particular, summer months show the highest AOD_{440} (due to particle stagnation and dust intrusions) and CWV (related to highest irradiances). However, the difficulties related to lunar irradiance measurements manifest themselves in a larger dispersion and fewer available data points. What is more, based on the performance of the Moon phase criterion, it appears that lower lunar irradiances imply larger measurement uncertainties. This, in addition to the larger uncertainty in the retrieval of $\alpha_{440-870}$ for the lower AOD_{440} could be responsible for the larger divergences observed in the comparison of daytime and nighttime $\alpha_{440-870}$. On the other hand, the effect of the time differences criterion is also remarkable when comparing both data sets, as it discards data pairs showing larger divergences.

References:

Kendall, M.G., 1975. Rank Correlation Methods. Griffin, London. URL. https://www.cambridge.org/core/journals/journal-of-the-institute-of-actuaries/article/abs/rank-correlation-methods-by-maurice-g-kendall-ma-pp-vii-160-london-charles-griffin-and-co-ltd-42-drury-lane-1948-18s/335FD9F4DDCBDF8A7167B4B66EE4DFB9?utm_campaign=shareaholic&utm_medium=copy_link&utm_source=bookmark

Li, J., Carlson , B.E., Dubovik , O., Lacis , A.A. (2014). Recent trends in aerosol optical properties derived from AERONET measurements . Atmos. Chem. Phys. 14 (22), 12271 12289. URL: https://acp.copernicus.org/articles/14/12271/2014/

Mann, H.B., 1945. Nonparametric tests against trend. Econometrica 13, 245. URL. http://danida.vnu.edu.vn/cpis/files/Refs/PCAs/Mann_1945_NONPARAMETRIC%20TESTS%20AGAINST%20TREND.pdf

Román, R., González, R., Toledano, C., Barreto, Á., Pérez Ramírez, D., Benavent Oltra , J. A., Olmo, F. J., Cachorro, V. E., Alados Arboledas, L., and de Frutos, Á. M . (2020): Correction of a lunar irradiance model for aerosol optical depth retrieval and comparison with a star photometer, Atmos. Meas. Tech, 13, 6293 6310. URL: https://amt.copernicus.org/articles/13/6293/2020/

Sen, P.K., 1968. Estimates of the regression coefficient based on Kendall's Tau. J. Am. Stat. Assoc. 63 (324), 1379–1389. URL: https://www.tandfonline.com/doi/abs/10.1080/01621459.1968.10480934

3. Synergy with airborne based techniques

3.1 Current status of airborne-based techniques

Based on the HARMONIA project #21: "State of the art research on airborne and sunphotometry measurements intercomparison". Authors: Alkistis Papetta, Franco Marenco, Meritxell Garcia-Suñer, Victor Estellés and Monica Campanelli.

Airborne platforms, ranging from large Atmospheric Research Aircraft (ARA) to small Unmanned Aerial Vehicles (UAVs), play an important role in atmospheric research. They complement ground-based remote sensing by providing a three-dimensional view of the atmosphere and they facilitate the calibration and validation of remote sensing measurements. Airborne systems enable detailed investigation of atmospheric processes that are otherwise difficult to observe, such as aerosol dynamics during extreme events like volcanic eruptions or dust storms.

The use of airborne platforms has grown significantly in recent years due to technological advancements, including the miniaturization of sensors and increased flight endurance. These advancements have made it possible to deploy various platforms—research aircraft, UAVs, and other platforms such as balloons —providing critical insights into the atmospheric composition, aerosol layers, and other key parameters. Drawing on the knowledge gained from previous campaigns with diverse objectives, instruments, and locations, (e.g. SAVEX-D, ASKOS, and others) this document consolidates best practices to ensure optimal planning and execution of future airborne and ground-based measurement campaigns.

- <u>**Objectives of Co-located Airborne and Ground-based Campaigns**</u>

An important goal of campaigns integrating airborne and ground-based remote sensing is to enhance the calibration and validation of data obtained from sunphotometers, lidars, and spaceborne sensors. The synergy of methods helps in providing vertically resolved observations, offering insights into particle size distribution (PSD), aerosol composition, and other properties that cannot be measured by ground-based remote sensing alone. Typical campaign objectives include:

1) Calibration and Validation: Airborne observations, including PSD, aerosol composition and refractive index measurements, are used to assess the accuracy of remote sensing measurements.
2) Vertically Resolved Observations: Instruments like sunphotometers provide columnar data, but airborne observations can offer vertical profiles of aerosols, improving understanding of aerosol vertical distribution.
3) Comprehensive Aerosol Studies: Airborne campaigns help study aerosol properties in greater detail during dust events or volcanic eruptions, providing a full picture of aerosol characteristics.

o **<u>Measurement Techniques and Sensors</u>**

1) Ground-Based Sensors: These include various types of lidars (Elastic Backscatter, High-Spectral-Resolution, Raman Lidar) and photometers (sun and lunar photometers). Lidar systems provide vertically resolved information on aerosols, measuring parameters such as backscatter, extinction coefficients, and aerosol optical depth. Photometers, on the other hand, derive aerosol and cloud optical properties from solar or lunar radiation.

2) Airborne Platforms and Sensors: Airborne observations are typically conducted using manned aircraft, UAVs or balloons. Manned aircraft have an endurance of several hours and can carry substantial payloads, making them ideal for extended missions. UAVs, particularly fixed-wing and multirotor types offer flexibility for rapid deployment in restricted or hazardous environments, but are often very limited in terms of payload and endurance.
   The airborne sensors include amongst others Optical Particle Counters (OPCs) for measuring PSD, backscatter sondes for atmospheric profiling, and methods for collecting aerosol samples on filters or impactors for subsequent laboratory analysis. These sensors provide valuable data for complementing ground-based remote sensing observations and validating model outputs.

o **<u>Quality Assurance and Measurement Uncertainties</u>**

To ensure the reliability of data collected during these campaigns, rigorous quality control protocols are essential. Airborne sensors also undergo pre-flight and in-laboratory calibrations to ensure data quality. For lidar systems, this includes background correction, depolarization calibration, and overlap correction. Similarly, photometers must be carefully calibrated, especially when deployed as mobile units in field campaigns.

o **<u>Campaign Planning</u>**

1) Pre-Planning Phase: The first step in planning a campaign is to establish what are its objectives and goals. These objectives will determine the selection of sensors, the choice of location, and the timing of the campaign. For example, a campaign focused on studying desert dust may choose a location in the dust belt and select a time period with low cloud cover and minimal rainfall to ensure optimal conditions for data collection.The location of the

campaign should allow for the co-location of ground-based sensors and airborne platforms within a reasonable distance.

2) Sensor Selection: The campaign objectives will dictate the choice of sensors. Both airborne and ground-based platforms must be equipped with sensors that can capture the desired measurements, such as aerosol optical depth, particle size distribution, or refractive index. It is also important to ensure that the airborne and ground-based sensors are compatible and can provide complementary data.

3) Flight Planning: Airborne operations are costly and often they are sporadic, so flight paths and altitudes must be carefully planned to optimize data collection. Weather forecasting plays a key role in determining whether a flight can proceed as planned. A system of possibility flags (high, medium, low) is used to assess the feasibility of flights based on meteorological conditions.

4) On the day of the flight, the mission scientist consults ground-based observations and weather forecasts to finalize the flight plan. Flexibility is crucial, as weather conditions may change rapidly, requiring adjustments to the flight schedule.

o **Conclusions**

The integration of airborne and ground-based remote sensing platforms offers unique advantages for atmospheric research. By combining the vertical resolution provided by airborne platforms with the columnar data from ground-based systems, researchers can achieve more accurate measurements of aerosol properties, particularly during extreme events. Effective campaign planning and stringent quality control measures are essential for the success of these integrated observation campaigns.

3.2 Use of UAV-based techniques for the improvement of vertical profiling

Based on: "Integrating UAV-Based In-Situ and Ground-Based Remote Sensing Observations for Enhanced Aerosol Profiling" presented at the European Meteorological Society Annual Meeting, Barcelona 8-12 September 2024. Authors: Alkistis Papetta, Maria Kezoudi, Chris Stopford, Troy Thornberry, Jean Sciare, and Franco Marenco.

Combined ground-based lidar and photometer setups are frequently employed, allowing for simultaneous collection of both columnar and vertical aerosol data. These two remote sensing methods provide complementary insights: lidar systems offer high-resolution vertical information through backscatter signals, while sunphotometers measure columnar aerosol optical depth (AOD), size distributions, and refractive indices (Ansmann et al., 2019; Lopatin et al., 2013).
Retrieval algorithms play a significant role in processing remote sensing data, utilizing sunphotometer measurements alongside lidar backscatter signals to derive vertically resolved

aerosol properties. The integration of these observations facilitates the estimation of aerosol concentration profiles (Mamouri and Ansmann, 2013).
Additionally, unmanned aerial vehicles (UAVs) equipped with in-situ sensors can provide vertically-resolved particle size distributions (PSDs). These UAV-based data serve as a valuable complement to the information gathered by lidar and sunphotometer systems. By collocating UAV observations with ground-based observations we aim to enhance the accuracy of aerosol vertical concentration assessments, utilizing Optical Particle Counters (OPCs) integrated into UAVs such as those operated by the Unmanned Systems Research Laboratory (USRL) ofThe Cyprus Institute (Kezoudi et al., 2021a).
To illustrate the potential of enhancing aerosol vertical PSD measurements we utilize observations from two campaigns. The ASKOS Campaign in Cape Verde (June 2022) aimed to validate Aeolus satellite aerosol products using advanced lidar systems, an AERONET sunphotometer (Sinyuk et al., 2020), and other instruments, with UAVs providing vertical profiles of aerosol characteristics in parallel. The Fall Campaign in Cyprus (October-November 2021) focused on the microphysical properties of transported mineral dust using UAVs equipped with OPCs, COBALDs, and impactors, alongside ground-based measurements from lidar, ceilometers, and sunphotometers. Both campaigns strategically utilized UAV-OPC flights near lidar and sunphotometers to collect detailed data on aerosol properties, including backscatter, extinction coefficients, AOD, and PSD, while also analyzing mineralogical composition.
Here we describe the methodology using two cases, June 24, 2022 during ASKOS campaign and October 25, 2021 during Fall Campaign 2021.

- <u>Lidar</u>

Lidar systems provided detailed vertically resolved data, including backscatter and extinction coefficients, as well as particle linear depolarization ratios (PLDR). Figure 3.2.1 presents the extinction and VDR profiles for the two demonstration cases. On June 24, 2022, we observed a dust layer starting above the marine boundary layer ~1.5km and extending up to 5.5 km. On November 15, 2021 the dust layer extended from ground up to 3.5 km.

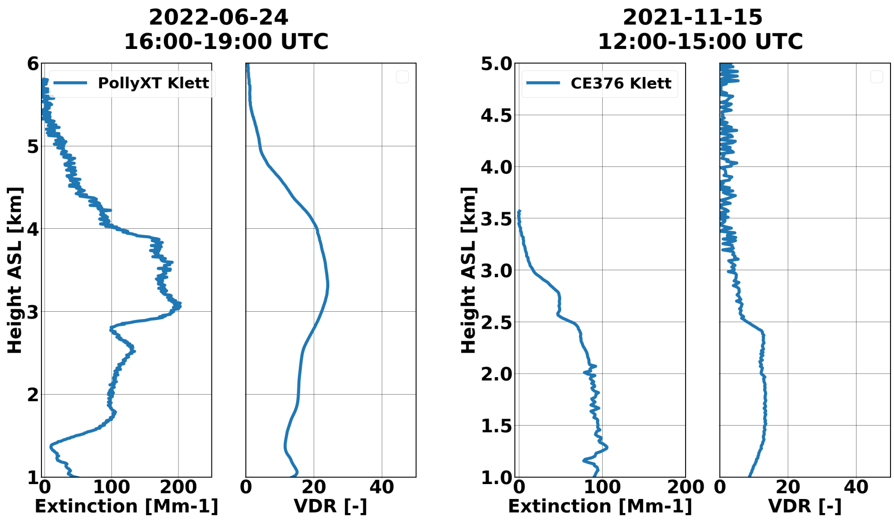

Figure 3.2.1.: Volume depolarization ratio and extinction as measured by PollyXT lidar in Mindelo, Cape Verde on 24/06/2022 (left) and Orounda, Cyprus on 15/11/2021 (right).

- <u>AERONET</u>

Sunphotometers were employed to measure AOD and PSD. On June 24, 2022, AERONET measurements in Mindelo, Cape Verde. indicated a consistent Aerosol Optical Depth (AOD) of 0.5 at 500 nm, with an Angstrom exponent (440-870 nm) of 0.1 throughout the day. These measurements suggest the presence of coarse-mode particles, typical of dust.

On November 15, 2021, AERONET measurements in Nicosia, Cyprus recorded an Aerosol Optical Depth (AOD) of ~0.3 at 500 nm, with an Angstrom exponent (440-870 nm) of ~1.0, indicating the dominanceof fine-mode particles even during the dust event. The PSDs from the two events are illustrated with a black line in Figure 3.2.2.

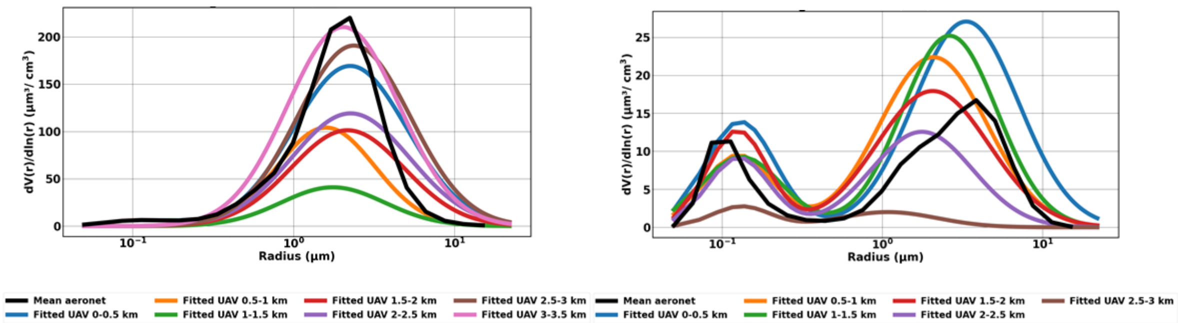

Figure 3.2.2.: UAV-based PSD vs AERONET PSD for 24/06/2022 (left) and 15/11/2021 (right).

- <u>UAV-based in-situ</u>

In the two cases considered, UAV-based in-situ observations using Optical Particle Counters (POPS and UCASS) (Gao et al., 2016; Smith et al., 2019) collected data on particle size distributions (PSD) and vertical aerosol concentrations, along with mineralogical composition analysis through SEM.

During the ASKOS campaign on June 24, 2022, two UAV flights were conducted in the afternoon. The first flight, equipped with POPS, reached 4.9 km and detected aerosols up to this altitude. The second flight, using UCASS, climbed to 4.5 km. These flights identified two distinct dust layers between 1.5-3.7 km.

Similarly, during the Fall Campaign on November 15, 2021, two UAV flights reached 4 km and identified a dust layer extending from the ground to 2.8 km, with a temperature inversion marking the top. The second flight, using POPS, confirmed the vertical aerosol distribution.

The POPS and UCASS data were combined to cover a broader range of particle sizes. Comparisons with AERONET PSDs, adjusted for dust layer depth, showed general agreement as seen in Figure 3.2.1. However these comparisons highlight the enhanced detail that UAV-based measurements provide in aerosol profiling. Interestingly, during ASKOS, coarse particles exist for all the observed heights, whilst during Fall Campaign there is a shift of the coarser to finer particles for increasing height.

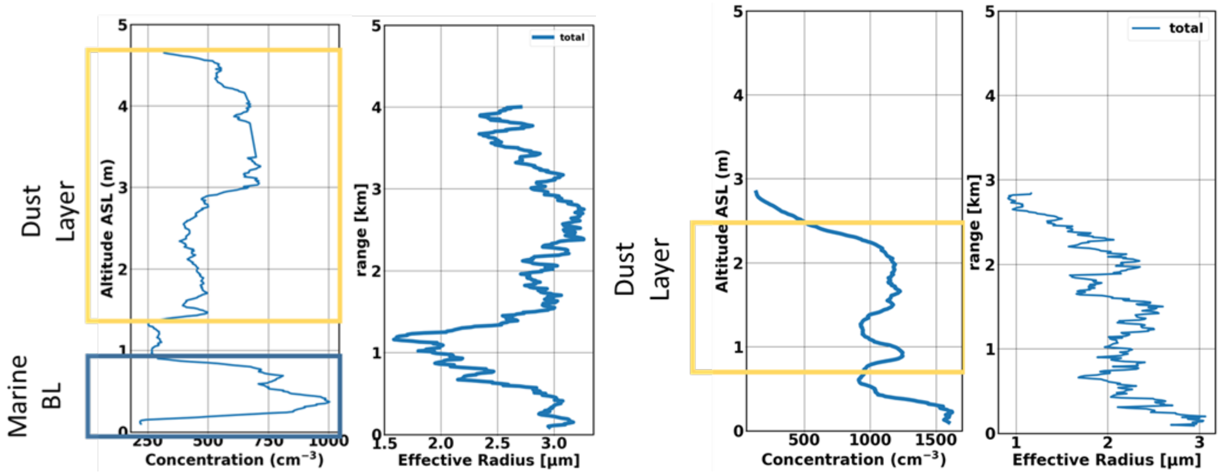

Figure 3.2.3.: Number concentration and effective radius from the combined POPS and UCASS observations on 24/06/2022. for 24/06/2022 (left) and 15/11/2021 (right).

- <u>MOPSMAP</u>

To convert lidar observations of optical properties into height-resolved particle concentrations, the extinction-to-volume parameter is crucial. This can be derived using various techniques. For instance, AERONET uses measurements of total column effective AOD and retrievals of size distributions to determine extinction-to-volume values. The POLIPHON (Gao et al., 2016; Sinyuk et al., 2020) algorithm employs this parameter along with vertical observations of PLDR to distinguish between mineral dust and non-dust aerosol components, such as anthropogenic haze and biomass burning smoke.

The MOPSMAP (Gasteiger and Wiegner, 2018) (Modeled Optical Properties of Ensembles of Aerosol Particles) algorithm offers a computationally efficient approach for optical modeling, even with complex aerosols. MOPSMAP considers spheres, spheroids, and a set of irregular particle shapes over a range of sizes and refractive indices.

The PSDs shown in Figures 3.2.2. were used as input in the MOPSMAP tool to derive the extinction-to-volume parameter at the different layers. The MOPSMAP τ/V calculated for different refractive index values is compared to the observed profile, AERONET and the literature range of values. The comparison reveals a good agreement between all the methods except AERONET which overestimates τ/V for both cases. In addition for the Fall Campaign case the literature range doesn't overlap with the calculated values. This must be due to the limited number of studies dealing with dust arriving purely from the Arabian desert.

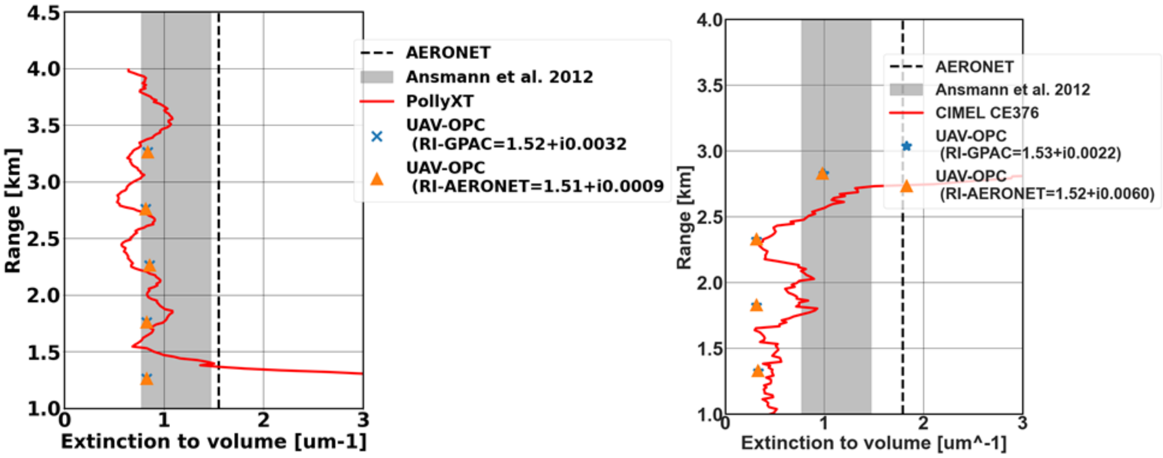

Figure 3.2.4.: Number concentration and effective radius from the combined POPS and UCASS observations on 24/06/2022. for 24/06/2022 (left) and 15/11/2021 (right).

References

Ansmann, A., Mamouri, R.-E., Hofer, J., Baars, H., Althausen, D., and Abdullaev, S. F.: Dust mass, cloud condensation nuclei, and ice-nucleating particle profiling with polarization lidar: updated POLIPHON conversion factors from global AERONET analysis, Atmos. Meas. Tech., 12, 4849–4865, https://doi.org/10.5194/amt-12-4849-2019, 2019.

Gao, R. , Telg, Hagen , Mclaughlin, R. , Ciciora, Steven , Watts, Laurence , Richardson, M. , Schwarz, J. , Perring, A. , Thornberry, T. , Rollins, A. , Markovi, M. , Bates, T. , Johnson, J. and Fahey, D.. A light-weight, high-sensitivity particle spectrometer for PM2.5 aerosol measurements, Aerosol Science and Technology, 50:1, 88-99 https://doi.org/110.1080/02786826.2015.1131809 , 2016.

cost
EUROPEAN COOPERATION IN SCIENCE & TECHNOLOGY
Funded by the European Union

Gasteiger, J. and Wiegner, M.: MOPSMAP v1.0: a versatile tool for the modeling of aerosol optical properties, Geosci. Model Dev., 11, 2739–2762, https://doi.org/10.5194/gmd-11-2739-2018 , 2018.

Kezoudi M, Keleshis C, Antoniou P, Biskos G, Bronz M, Constantinides C, Desservettaz M, Gao R-S, Girdwood J, Harnetiaux J, et al. The Unmanned Systems Research Laboratory (USRL): A New Facility for UAV-Based Atmospheric Observations. Atmosphere.; 12(8):1042. https://doi.org/10.3390/atmos12081042 , 2021a.

Lopatin, A., Dubovik, O., Chaikovsky, A., Goloub, P., Lapyonok, T., Tanré, D., and Litvinov, P.: Enhancement of aerosol characterization using synergy of lidar and sun-photometer coincident observations: the GARRLiC algorithm, Atmos. Meas. Tech., 6, 2065–2088, https://doi.org/10.5194/amt-6-2065-2013 , 2013.

Mamouri, R. E. and Ansmann, A.: Fine and coarse dust separation with polarization lidar, Atmos. Meas. Tech., 7, 3717–3735, https://doi.org/10.5194/amt-7-3717-2014, 2014.

Sinyuk, A., Holben, B. N., Eck, T. F., Giles, D. M., Slutsker, I., Korkin, S., Schafer, J. S., Smirnov, A., Sorokin, M., and Lyapustin, A.: The AERONET Version 3 aerosol retrieval algorithm, associated uncertainties and comparisons to Version 2, Atmos. Meas. Tech., 13, 3375–3411, https://doi.org/10.5194/amt-13-3375-2020 , 2020.

Smith, H., Ulanowski, Z., Kaye, P., Hirst, E., Stanley, W., Kaye, R., Wieser, A., Stopford, C., Kezoudi, M., Girdwood, J., Greenaway, R.,and Mackenzie, R.: The Universal Cloud and Aerosol Sounding System (UCASS): A low-cost miniature optical particle counter for use in dropsonde or balloon-borne sounding systems, Atmospheric Measurement Techniques, https://doi.org/10.5194/amt-12-6579-2019 , 2019.

3.3 Use of aircraft data for the improvement of AERONET and SKYNET ground based measurements

Based on the HARMONIA project #10: "Validation of AERONET and SKYNET columnar size distributions with airborne data in SAVEX-D campaign". Authors: Meritxell Garcia-Suñer, Franco Marenco, Víctor Estellés.

Measurements of aerosol properties by ground based sun photometers are employed as input data in climatological studies, aerosol model verifications and validations of satellite products. Therefore, it is essential to homogenise and validate the retrievals from different networks. Some discrepancies are observed in NASA's AERONET (who base their measurements on Cimel CE318 sun photometers) and University of Tokyo's SKYNET (who use PREDE POM sun photometers in the data collection process) products, in particular in the volume size distributions, that required further investigation.

The 2015 SAVEX-D campaign was set up in order to address this issue. Hence, a Cimel CE318 and a PREDE POM were installed on the island of Praia (Cape Verde) and their retrievals were compared with vertically integrated size distributions obtained from in-situ instrumentation in the FAAM Bae-146 atmospheric research aircraft. Two flights were carried out on 16 August 2015 (from 14:45 h to 19:01 h LT) and on 25 August 2015 (from 14:39 h to 18:00 h LT). The particularity of this site is that it is frequently affected by Saharan dust outbreaks, so that the AOD during the measurement process was between 0.4 and 0.6 thus allowing good conditions for inter-comparison in conditions of desert dust.

This study aims to validate the size distributions obtained by different versions of AERONET's (Versions 2 and 3) and SKYNET's (Skyrad 4.2, 5 and MRI v2) inversion algorithms against the airborne in-situ retrievals. For this purpose, the summary presented here focuses on the flight performed on 16 August over Praia. Prior to the inter-comparison between retrieval algorithms, their performance is briefly analysed based on the variation of the input parameters.

The in-situ size distribution is obtained from the PCASP, CDP and 2DS measurements, which were on board during the flight. The columnar size distribution is computed from the sum of the size distributions recorded in every layer along single level runs (SLR) multiplied by the height of the corresponding layer. For the identification of the layers, information from lidar onboard and nephelometer measurements was used.

The main conclusions drawn from the study of the characteristics of each inversion algorithm are summarised as follows:

- AERONET

When the SAVEX-D campaign was carried out in 2015, AERONET's Version 2 of the inversions were available. This data set has been recomputed and the results that are currently available in AERONET's website correspond to Version 3, so a comparison between versions can still be performed, as shown in Figure 3.3.1. According to Sinyuk et al. (2020), V3 is based on the same inversion algorithm as V2 but with some improvements, so little difference has been observed between both version's retrievals.

When compared to in-situ, discrepancies in the VSDs are found at the extreme radii: for the smallest radii, these could be related to higher uncertainty in the retrievals; whereas for larger r, there is an underestimation in the volume of coarse mode particles.

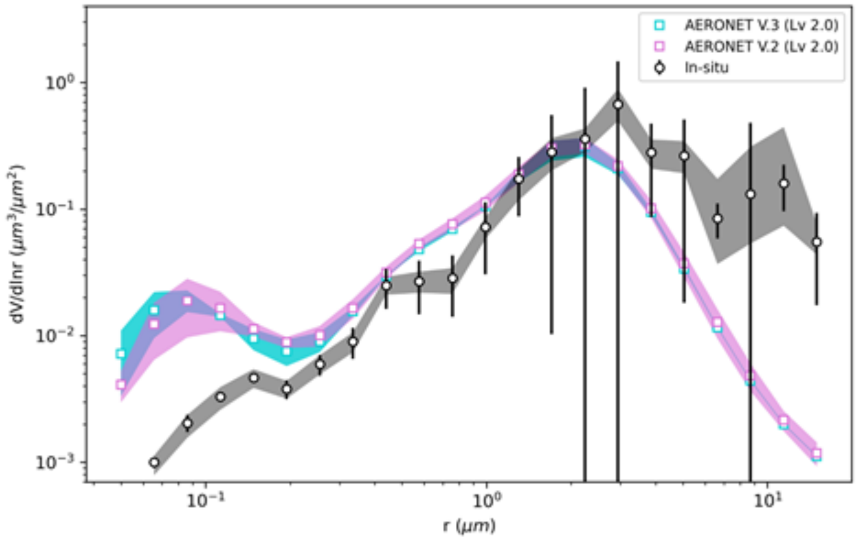

Figure 3.3.1: Comparison of $dV/dlnr$ *corresponding to V2 and V3 AERONET Lv 2.0 retrievals (pink and blue points, respectively), with the in-situ size distribution (in black). The shadows represent the standard deviation of the averaged data points. For this plot, it is not possible to select only those measurements corresponding to the time of the flight, since V3 Lv 2.0 only provides data from the morning, and in the case of V2, only one measurement would be available. In any case, the corresponding change in AERONET's V2 curve would not be significant.*

- Skyrad 4.2

In the case of Skyrad 4.2 and Skyrad 5 algorithms, a sensitivity study concerning the effect of the input parameters for the inversion process was carried out. Particularly, the effect on changes in the initial refractive index (real and imaginary parts) and the ground albedo was examined. The reference case for the sensitivity analysis is the standard configuration employed in the International SKYNET Data Center (ISDC).

Figures 3.3.2a and 3.3.2b illustrate the variability of the retrievals on the real and the imaginary part of the refractive index, respectively. It can be observed that the extreme values of the distribution are more sensitive to the changes in the input parameters. Indeed, the variability is especially noticeable at smaller radii (see Figure 3.3.2a). On the other hand, variations in the initial values of the ground albedo do not significantly affect retrievals. Nevertheless, these variations are not important overall, since the discrepancies with the reference distribution (nominal) are rather small. Indeed, the colour band corresponding to the points from the sensitivity study, computed based on the standard deviation of the distributions obtained from the different input parameters, is thinner than the colour band corresponding to the nominal retrievals, which is computed from the standard deviation of the volume size distributions measured during the time of flight.

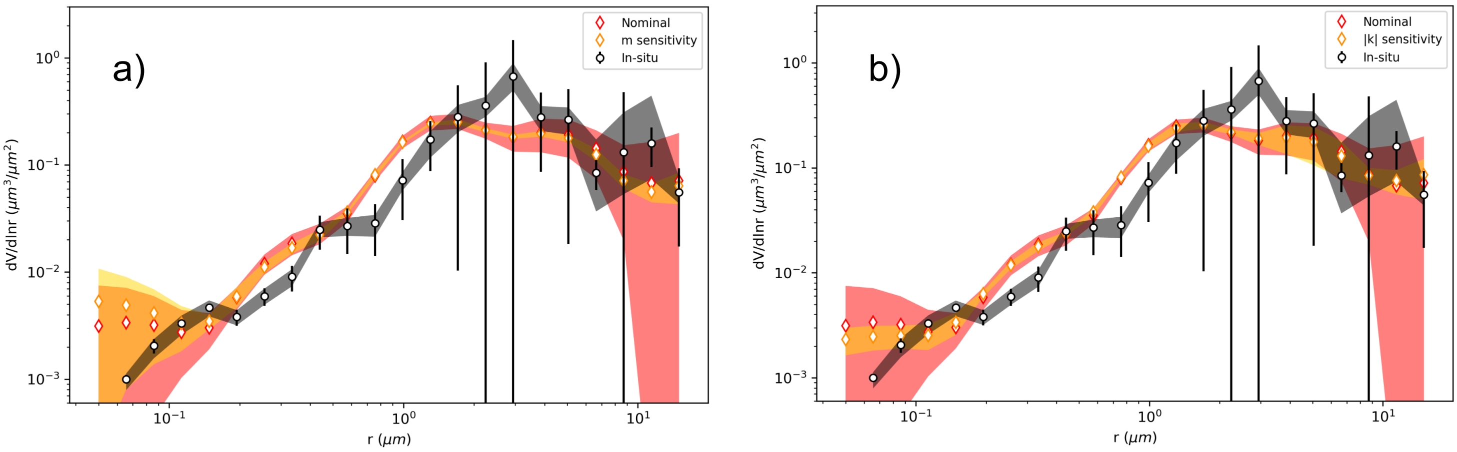

Figure 3.3.2: Comparison of $dV/dlnr$ retrievals obtained from different initial values of a) m and b) $|k|$ (orange) with the in situ (black) and the inversion based on the nominal set of input values (red).

- <u>Skyrad 5</u>

The sensitivity study carried out for Skyrad 5 yielded similar results with respect to its predecessor. As illustrated in Figures 3.3.3a and 3.3.3b, when the initial values of the real and imaginary parts of the refractive index are varied, respectively, it is found that the largest dispersion appears for the smallest radii. In fact, in these points, the colour band associated to the standard deviation of the obtained size distributions is broader than the colour band related to the standard deviation of the volume size distributions measured during the time of flight. Conversely, this large dispersion is not observed when the input ground albedo values are varied.

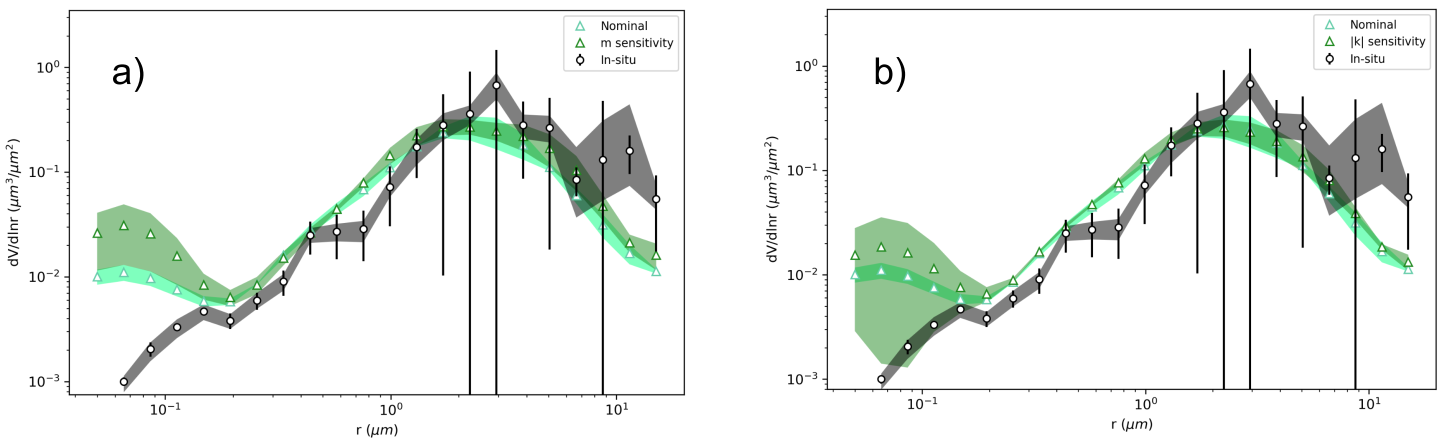

Figure 3.3.3: Comparison of $dV/dlnr$ retrievals obtained from different initial values of a) m and b) $|k|$ (green) with the in situ (black) and the inversion based on the nominal set of input values (aquamarine).

- <u>MRI v2</u>

According to Kudo et al. (2021), the smoothness constraints are optimised in the MRI algorithm, which significantly improves the results over its predecessors. In this case, the performance of the method has been explored by comparing the different outputs that are obtained when varying the type of particle specified. The options available are spheroid, Voronoi and hexahedral. Figure 3.3.4 depicts the results of this analysis. As it can be noticed, Voronoi and hexahedral characterisations provide a better description of the fine mode, which the other algorithms had difficulties to reproduce.

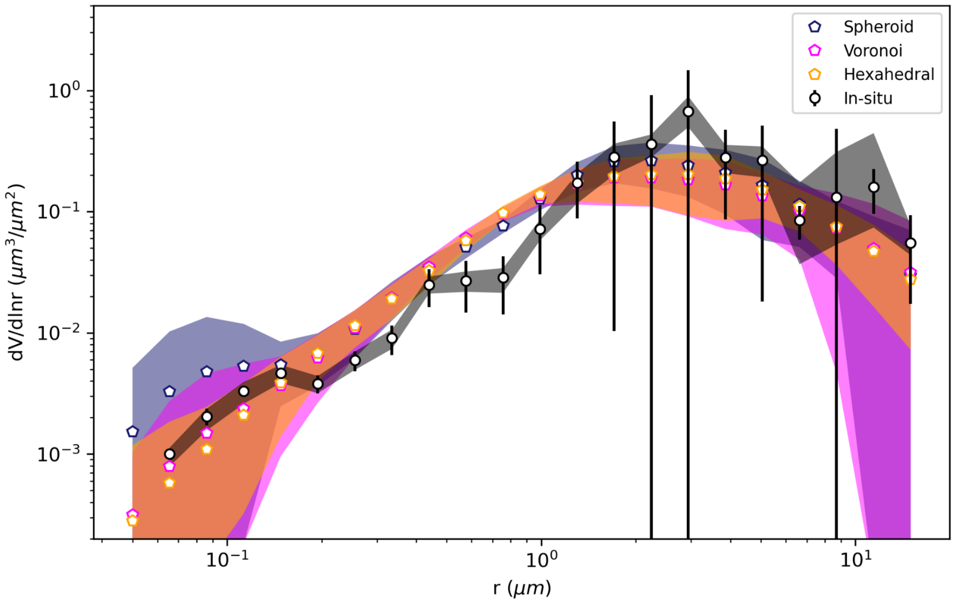

Figure 3.3.4: Comparison of $dV/dlnr$ MRI v2 retrievals for the different particle models available in MRI v2: spheroid (purple), Voronoi (fuchsia), and hexahedral (orange) with the in-situ curve (black).

Finally, the volume size distributions obtained from each inversion algorithm using the nominal set of input values have been plotted, along with the in-situ distribution, in Figure 3.3.5a. In addition, the corresponding relative differences with respect to the in-situ curve are shown in Figure 3.3.5b. Although considerable discrepancies are observed at the extremes of the distribution for any inversion algorithm (indeed, the fine mode was overestimated by all the inversion algorithms), Skyrad 4.2 and MRI provide the best descriptions of the fine and coarse modes.

Unlike Skyrad 4.2, the Skyrad 5 algorithm underestimates the coarse mode. This behaviour was also found in previous studies (Hashimoto et al. 2012), and is attributed to the strong constraints imposed and the use of a too small radius to model the coarse mode.

Regarding AERONET, the corresponding volume size distribution is the most divergent with respect to in situ measurements when considering the extremes of the distribution. However, it is important to remark that, unlike the other algorithms, measurements from the whole day have to be taken into account due to the lack of data passing the established quality filters during the time of flight.

Furthermore, it is important to remark that the in-situ maximum at $r \approx 15\,\mu m$ cannot be detected due to technical limitations of the Prede POM (Kudo et al. 2021) (see Figure 3.3.5b).

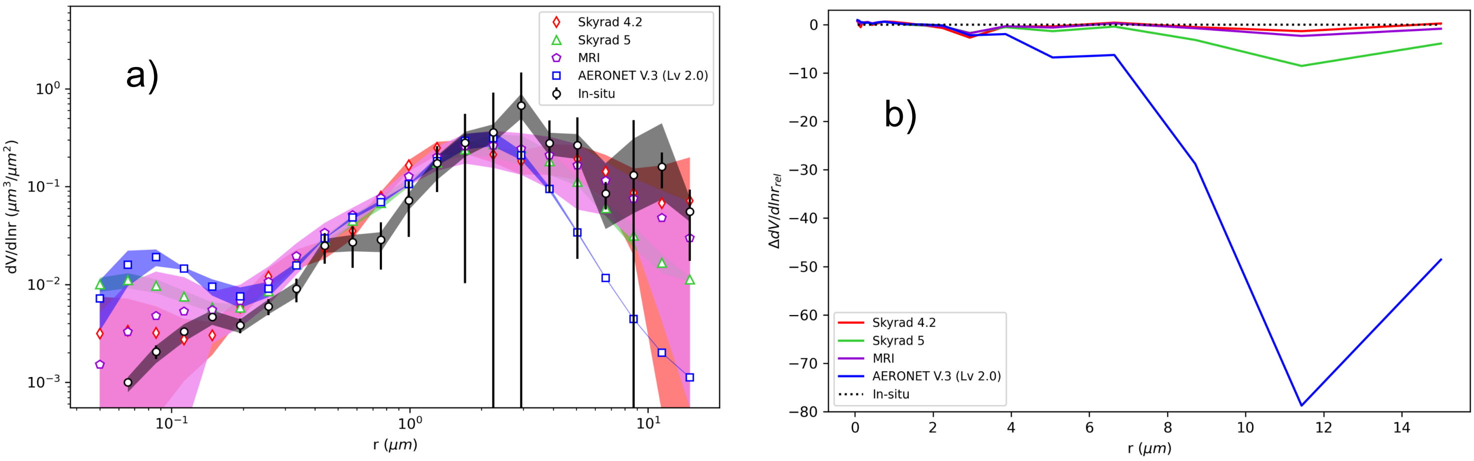

Figure 3.3.5: a) Comparison of the nominal $dV/dlnr$ obtained for each inversion algorithm with in-situ measurements. b) Relative $dV/dlnr$ difference of each inversion algorithm with the in situ curve.

In conclusion, the comparison of different versions of the AERONET and SKYNET inversion algorithms using airborne in situ $dV/dlnr$ measurements as reference show good agreement in the interval $r \in [0.2, 2.2]\,\mu m$. However, the discrepancies at the extremes of the distribution, where uncertainties are higher, are significant. In particular, both versions from AERONET overestimate the fine and underestimate the coarse mode. In addition, strong constraints in the inversion algorithm favour a similar behaviour for Skyrad 5. Conversely, Skyrad 4.2 and MRI v2 show better comparison. Indeed, MRI v2 size distributions for small radii are similar to in situ retrievals when non-sphericity is considered. Hence, the need for improved inversion algorithms has been demonstrated. To this end, other retrieval algorithms such as GRASP should be applied to this data. Furthermore, additional uncertainty estimations will be performed for SKYNET cases.

References:

Hashimoto, M., Nakajima, T., Dubovik , O., Campanelli , M., Che, H., Khatri , P., Takamura , T., and Pandithurai , G . (2012): Development of a new data processing method for SKYNET sky radiometer observations, Atmos. Meas. Tech., 5, 2723 2737. URL: https://amt.copernicus.org/articles/5/2723/2012/

Kudo, R., Diémoz , H., Estellés , V., Campanelli , M., Momoi , M., Marenco , F., Ryder , C. L., Ijima , O., Uchiyama , A., Nakashima , K., Yamazaki , A., Nagasawa , R., Ohkawara , N., and Ishida , H . (2021): Optimal use of the Prede POM sky radiometer for aerosol, water vapor, and ozone retrievals, Atmos. Meas. Tech., 14, 3395 3426. URL: https://amt.copernicus.org/articles/14/3395/2021/

Sinyuk , A., Holben , B. N., Eck , T. F., Giles, D. M., Slutsker , I., Korkin , S., Schafer, J. S., Smirnov , A., Sorokin , M., and Lyapustin , A . (2020): The AERONET Version 3 aerosol retrieval algorithm, associated uncertainties and comparisons to Version 2, Atmos. Meas. Tech., 13, 3375 3411. URL: https://amt.copernicus.org/articles/13/3375/2020/

4. Harmonization with lower-cost techniques

4.1 Current efforts on the validation and harmonization of lower-cost techniques with established networks

4.1.1. Empirical correction of multifilter rotating shadowband radiometer (MFRSR) AODs based on the comparison with AERONET data at Lampedusa island

Based on the HARMONIA project #5: "Main "incompatibilities" and "compatibilities" between the different measurement systems. Understand gaps and improvements". Authors: Daniela Meloni, Sabina Zero, José Balenzategui, Monica Campanelli (Project 5, involving Daniela Meloni, Sabina Zero, José Balenzategui, Monica Campanelli: **in progress**)

The shadowband radiometers derive the direct radiation component as the difference between measurements of the global and diffuse irradiances. The Multifilter rotating shadowband radiometer (MFRSR) model MFR-7, described in details by Harrison et al. (1994), measures global and diffuse irradiances in six narrow bands in the visible/NIR, each with about 10 nm full-width at half-maximum bandwidths. The AOD can be calculated from the direct component, applying the Lambert–Beer law, after the subtraction of the Rayleigh and the gas contributions. The instrumental extraterrestrial constants are derived by applying the Langley plot technique.

Few studies have been dedicated to the intercomparison of AOD measurements made with Sun pointing and shadowband instruments [Schmid et al., 1999; Mitchell and Forgan, 2003; McArthur et al., 2003; Kim et al., 2008; di Sarra et al., 2015; Rosário et al., 2019]. These studies suggest that the agreement of rotating shadowband instruments with direct sunphotometer is of the order of 0.02. However, that the length of the dataset and the AOD values considered in the intercomparison may affect the results. Rosário et al. [2019] found agreement between spectral AOD in the central Amazonia from MFRSR and AERONET Cimel in the years 2012 and 2015. The root mean square differences (RMSDs) at the MFRSR nominal wavelengths of 415, 500, 610, 670 nm are between 0.02 and 0.03, slightly above the assumed 0.02 uncertainty on AERONET AOD (0.02).

The paper by di Sarra et al. [2015] presents the comparison on the AOD at different wavelengths between 415 and 870 nm derived from MFRSR and level 2.0 AERONET Cimel measurements on the island of Lampedusa (35.5°N, 12.6°E) over a period of almost 4 years, encompassing the years from 2003 to 2012. Lampedusa site is strongly influenced by desert dust and marine aerosols and characterized by frequent cases of elevated AOD.

The Cimel and MFRSR wavelengths are not coincident. The AODs at six wavelengths (416, 440.6, 500, 614, 673, and 868 nm) were derived separately from the MFRSR and Cimel measurements; for each instrument, the Ångström relationship was applied using the AOD at the two encompassing wavelengths to derive the optical depth at the fixed wavelengths, when not directly measured.
The comparison shows that MFRSR underestimates the Cimel AOD by less than 0.02 at all wavelengths, with decreasing mean bias for increasing wavelength (see Table 4.1.1.1).

Table 4.1.1.1. Mean bias (MB) and root mean square difference (RMSD) between MFRSR and Cimel, where the MB is calculated as the average of the MFRSR AOD minus AERONET AOD. From di Sarra et al. [2015].

Wavelength (nm)	MB	RMSD	Number of Data Pairs
416	−0.016	0.042	8021
440.6	−0.018	0.042	15481
500	−0.016	0.037	16769
614	−0.011	0.032	16769
672	−0.009	0.030	16769
868	+0.002	0.023	16769

The AOD differences are dependent on the size of the aerosols, that is, the Ångström exponent, and on wavelength. Among the possible causes for the observed differences, only aerosol forward scattering is expected to display such a behavior. In this analysis all cases with Ångström exponent <0.5 based on the MFRSR observations are selected as those in which the contribution of large particles, due to mineral dust or marine aerosol, is significant. Such a classification is based on the paper by Pace et al. [2006]. Figure 4.1.1.1 shows the AERONET and MFRSR AOD scatterplots separately for cases with Ångström exponent ≥0.5 (defined as class 1) and Ångström exponent <0.5 (defined as class 2).

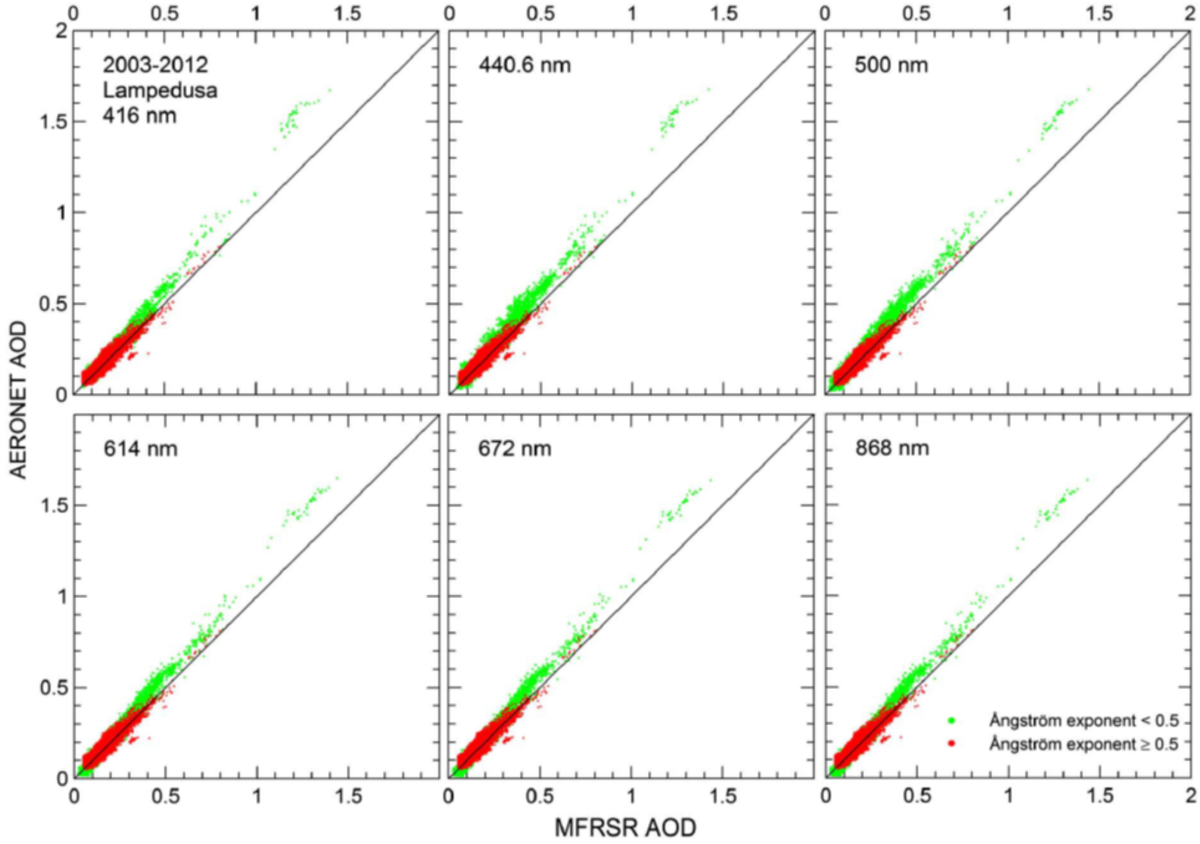

Figure 4.1.1.1. Scatterplot of Cimel versus MFRSR AODs, separately for Ångström exponent ≥0.5 (red dots) and Ångström exponent <0.5 (green dots) cases. From di Sarra et al. [2015].

The MB and RMSD separately for the two classes are reported in Table 2.

Table 4.1.1.2. MB and RMSD between MFRSR and Cimel AOD at each wavelength, for class 1 (Ångström Exponent ≥0.5) and class 2 (Ångström Exponent < 0.5). From di Sarra et al. [2015].

Wavelength (nm)	Class 1 MB	Class 2 MB	Class 1 RMSD	Class 2 RMSD
416	−0.0061	−0.034	0.03	0.057
440.6	−0.0073	−0.032	0.021	0.023
500	−0.0052	−0.030	0.023	0.049
614	−0.0031	−0.022	0.022	0.042
672	−0.0022	−0.018	0.021	0.039
868	+0.006	−0.004	0.020	0.030

The absolute value of the MB is always <0.0075 for class 1 and is smaller than in most of the previous studies. MB is negative at all wavelengths except 868 nm. In general, the RMSD is significantly smaller for class 1 than class 2. As expected, MB for class 2 is relatively large, reaching 0.03 at 416 nm. MB and RMSD show a general decrease with wavelength for both class 1 and 2.

An empirical correction, based on the comparison of MFRSR and Cimel data, was implemented for cases with Ångström exponent <0.5. For AOD =1 the correction to the MFRSR AOD is about 20% at 440.6 nm, 16% at 614 nm, and 12% at 869 nm.

References

A. di Sarra, D. Sferlazzo, D. Meloni, F. Anello, C. Bommarito, S. Corradini, L. De Silvestri, T. Di Iorio, F. Monteleone, G. Pace, S. Piacentino, and S. Pugnaghi, "Empirical correction of multifilter rotating shadowband radiometer (MFRSR) aerosol optical depths for the aerosol forward scattering and development of a long-term integrated MFRSR-Cimel dataset at Lampedusa," Appl. Opt. 54, 2725-2737 (2015).

L. Harrison, J. Michalsky, and J. Berndt, "Automated multifilter rotating shadow-band radiometer: an instrument for optical depth and radiation measurements," Appl. Opt. 33, 5118–5125 (1994).

S. W. Kim, S. C. Yoon, E. G. Dutton, J. Kim, C. Wehrli, and B. N. Holben, "Global surface-based Sun photometer network for long-term observations of column aerosol optical properties: intercomparison of aerosol optical depth," Aerosol Sci. Technol. 42, 1–9 (2008).

L. J. B. McArthur, D. H. Halliwell, O. J. Niebergall, N. T. O'Neill, J. R. Slusser, and C. Wehrli, "Field comparison of network Sun photometers," J. Geophys. Res. 108, 4596 (2003).

R. M. Mitchell and B. W. Forgan, "Aerosol measurement in the Australian outback: intercomparison of Sun photometers," J. Atmos. Ocean. Technol. 20, 54–66 (2003).

G. Pace, A. di Sarra, D. Meloni, S. Piacentino, and P. Chamard, "Aerosol optical properties at Lampedusa (central Mediterranean). 1. Influence of transport and identification of different aerosol types," Atmos. Chem. Phys. 6, 697–713 (2006).

N. E. Rosário, T. Sauini, T. Pauliquevis, H. M. J. Barbosa, M. A. Yamasoe and B. Barja "Aerosol optical depth retrievals in central Amazonia from a multi-filter rotating shadow-band radiometer calibrated on-site," Atmos. Meas. Tech. 12, 921–934, https://doi.org/10.5194/amt-12-921-2019 (2019).

B. Schmid, J. Michalsky, R. Halthore, M. Beauharnois, L. Harrison, J. Livingston, P. Russell, B. Holben, T. Eck, and A. Smirnov, "Comparison of aerosol optical depth from four solar radiometers during the fall 1997 ARM intensive observation period," Geophys. Res. Lett. 26, 2725–2728 (1999).

5. Multi-instrumental analyses of long-term aerosol, clouds and radiation trends

5.1 Long term trends of AOD and total ozone at the Poprad-Gánovce station in Slovakia based on 10 and 30 years of AERONET and Brewer measurements

5.1.1. 30 years of total ozone and AOD measurements using the Brewer spectrophotometer in Poprad-Gánovce, Slovakia

Based on HARMONIA project #5: "AOD long term trends from Brewer and Cimel instruments". Authors: Peter Hrabčák, Meritxell Garcia-Suñer, Violeta Matos, Víctor Estellés, Monica Campanelli.

In this project, AOD and total ozone measurements collected by a Brewer ozone spectrophotometer model MKIV, installed at the Poprad-Gánovce site (Slovakia), have been analysed. The analysis has been extracted from an HARMONIA sponsored presentation at the Quadrennial Ozone Symposium (QOS) conference.

The data set provided consisted of daily averages of total ozone and aerosol optical depths (AOD) determined from the direct sunlight measurements collected by the Brewer ozone spectrophotometer. These data covered the period from 18-08-1993 to 31-05-2024. For each retrieval, the number of data points employed in the computation of the corresponding daily mean has been indicated. A total of 5 channels were available: 306.3 nm, 310 nm, 313.5 nm, 316.8 nm and 320 nm, the last two being the most accurate (since the smaller the wavelength, the higher the uncertainty in the measurement).

In addition, the relationship between total ozone and tropopause height has been explored. For this purpose, a data set containing the values of the tropopause geopotential height for two times of the day (at 0h and at 12h GMT) has been employed.

The study is structured in four parts. The first one consist of a representation of daily, monthly and annual means of total O_3 and AOD. This is followed by an examination of the intra-annual evolution of these magnitudes. Next, the evolution of total O_3 and AOD over the full 30 years of available measurements is assessed. Finally, the last section is devoted to the study of the dependence of total ozone on the height of the tropopause.

1. **Representation and calculation of daily, monthly and annual means of AOD and total O_3.**

In this section, a preliminary study on the evolution of AOD and total ozone over time has been carried out. The aim was to identify any pattern described by these magnitudes that can be explained on the basis of local emissions or atmospheric circulation. For this purpose, the daily means (i.e. the data points provided) of the AOD for each wavelength and of total ozone have been plotted. Figures 5.1.1.1a and 5.1.1.1b show the corresponding results. For the sake of clarity, only the plot for AOD_{320} has been included. As it can be observed, both magnitudes clearly show periodic behaviour.

The evolution of their monthly means over the years of measurements is plotted in Figures 5.1.1.2a and 5.1.1.2b for AOD_{320} and total ozone, respectively. These values are calculated by grouping the data by months and computing the corresponding average for each year. Clear seasonal patterns are identified in both plots. For AOD, two peaks are usually distinguished during the year. The first appears mainly in April, while the second arises between June and September. The annual cycle of total O_3 is much clearer, reaching maximum values in March-April, then decreasing and reaching minimum values in October.

Regarding the AOD, the April maximum may be related to the higher occurrence of dust intrusions from the Sahara, that are more frequent in spring and summer than in autumn and winter. As for the summer maximum, this may be favoured by different factors. For instance, during the warm months, vertical mixing of the air is more efficient than during the cold season, which increases the thickness of the boundary layer. As a consequence, aerosols can reach higher altitudes and can thus

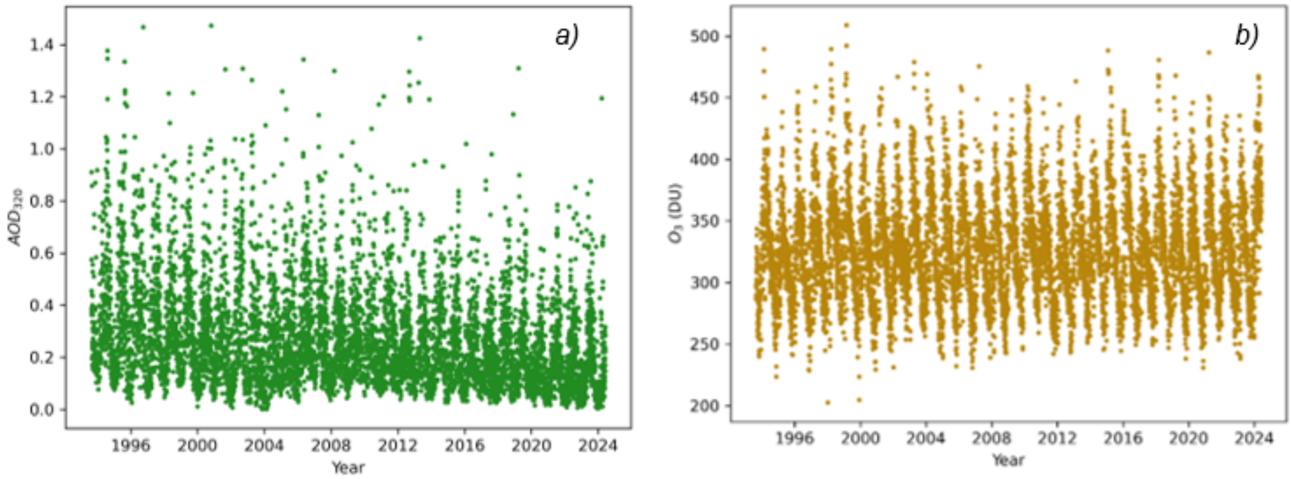

Figure 5.1.1.1: Daily AOD_{320} (a) and total O_3 (b) means computed based on the measurements of the Brewer ozone spectrophotometer from 18-08-1993 to 31-05-2024.

be detected by the instruments at the Poprad-Gánovce station (situated at 706 m a.s.l.). Moreover, due to higher summer irradiance and, consequently, higher evaporation, the CWV increases, which favours the growth of hygroscopic particles, thus increasing the AOD. In addition, it is important to take into account that the influence of local aerosol sources (natural or anthropogenic) is significant

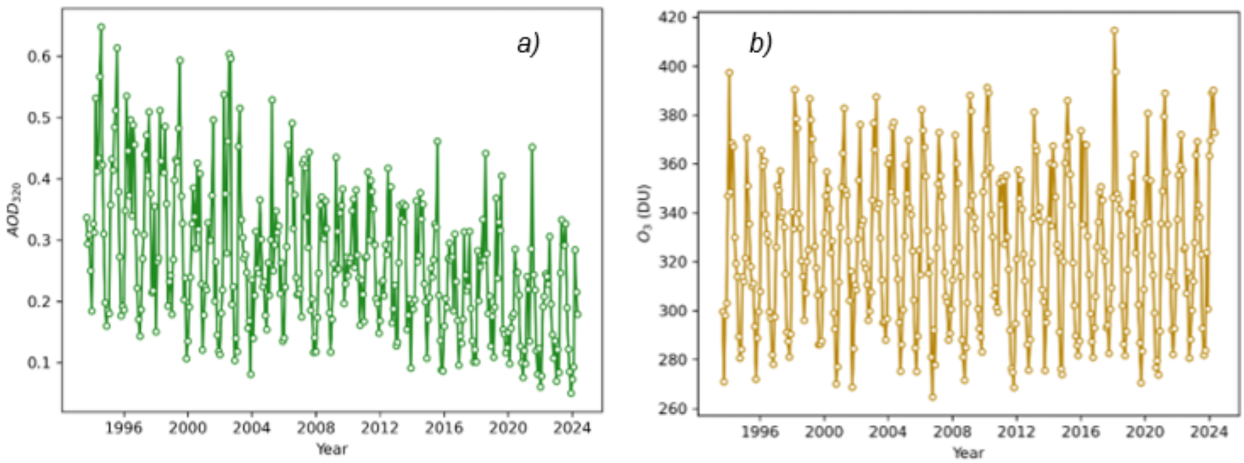

Figure 5.1.1.2: Monthly AOD_{320} (a) and total O_3 (b) means computed based on the measurements of the Brewer ozone spectrophotometer from September 1993 to May 2024.

during the warm season, when agricultural activities take place, biomass burning occurs and pollen levels in the air increase.

The lower aerosol loading measured during the cold season can be associated with different factors. On the one hand, during the cold half of the year, the predominance of a westerly flow from the Atlantic Ocean is detected, which is related to clean marine air masses. In addition, the fact that the station is located at a high altitude in an area frequently hit by strong winds, prevents the accumulation of anthropogenic aerosols. Furthermore, the terrain surrounding the station is usually wet and/or snow-covered during cold seasons, which rules out the possibility of local dust sources.

As for total O_3, the photochemical processes involved in the total daily ozone cycle are favoured by high irradiances (Schanz et al. 2014). Thus, one would think that the smaller solar zenith angle and longer days, resulting in higher irradiances, would completely explain the annual ozone cycle. However, as it will be discussed in the next section, ozone transport is almost completely determined by the Brewer-Dobson circulation.

Finally, the evolution of the annual means of the AOD and total ozone, obtained by grouping the daily mean data points by year and computing the corresponding average, is shown in Figures 5.1.1.3a and 5.1.1.3b, respectively. In the case of the AOD, all available channels have been plotted in order to show that their behaviour is similar. It is important to take into account that, since the database starts in August 1993 and ends in May 2024, the first and the last years are not complete. In fact, in the first case, data are only available for the cold half of the year, hence lower AOD and total ozone averages are obtained. Conversely, measurements in 2024 include mostly warm months, so the increase in total ozone is considerable for this year. Therefore, these two years have not been considered for the plot in Figures 5.1.1.3a and 5.1.1.3b. As shown in 5.1.1.3a, a decreasing trend in AOD for each channel can be easily identified. This trend is in agreement with the analysis performed by Li et al. (2014), who detected a decreasing AOD trend in European countries. This behaviour is mainly attributed to the introduction of governmental policies to reduce the emission of anthropogenic pollutants. With respect to total ozone (Figure 5.1.1.3b), no clear trend can be visually identified, although a fluctuating pattern which alternates maxima and minima can be visualised.

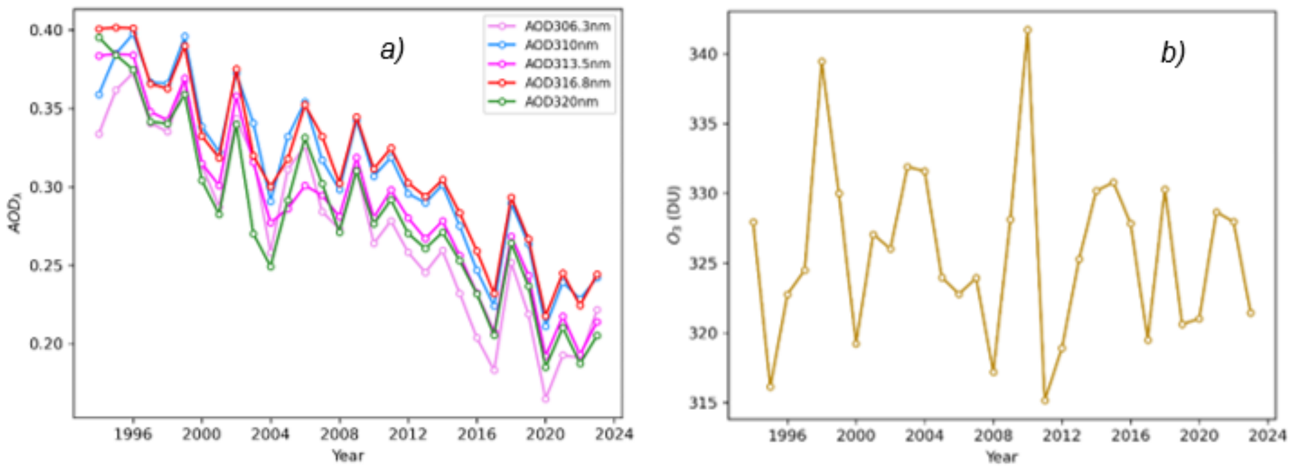

Figure 5.1.1.3: Annual AOD_{λ} (a) and total O_3 (b) means computed based on the measurements of the Brewer ozone spectrophotometer from 1994 to 2023.

2. Intra-annual variation of AOD and total ozone.

In this section, the evolution of the AOD and total ozone over the year has been analysed. For this purpose, some statistical magnitudes have been determined, including the median, the mean, the standard deviation and the first and third quartiles for each month of the year. The results are summarised in the boxplots in Figures 5.1.1.4a and 5.1.1.4b for AOD and total ozone, respectively. In addition, these statistics have been collected in Tables 5.1.1.1a and 5.1.1.1b. These results are calculated from monthly means (i.e. the statistics of a magnitude for a given month are computed based on the monthly means from September 1993 to May 2024 for that month).

The behaviour observed in Figures 5.1.1.2a and 5.1.1.2b is clearly seen in Figures 5.1.1.4a and 5.1.1.4b. The AOD shows two peaks: one in April, probably related to the increased presence of dust intrusions from North Africa; and another in August. The higher AOD values during the summer months may be related to the characteristic stable atmospheric conditions that favour the stagnation of aerosols and a more effective vertical mixing, as well as to hygroscopic particle growth processes enhanced by higher CWV concentrations or to the formation of secondary aerosols, favoured by higher irradiances. In addition to this, dust outbreaks are also common in *summer. Indeed, greater dispersion can be identified in Figure 5.1.1.4a and Table 5.1.1.1a for spring and summer months, which could be explained by the higher AOD values associated with these events.*

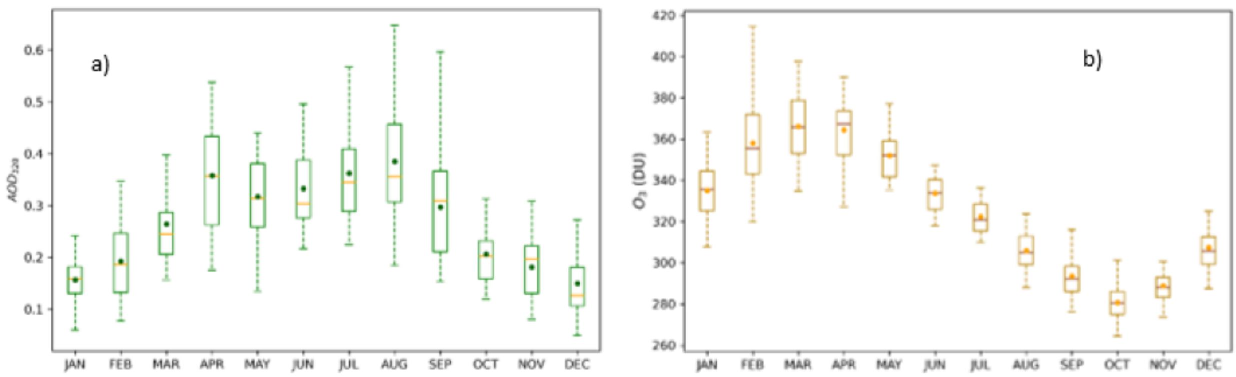

Figure 5.1.1.4: Boxplots showing AOD_{320} (a) and total O_3 (b) means (solid points) for each month computed using the Brewer ozone spectrophotometer from September 1993 to May 2024. The horizontal lines inside the boxes represent the medians. The boxes expand from the U25 and U75 percentiles. In addition, the lower and upper whiskers account for U25–1.5IQR and U75+1.5IQR, respectively, being IQR the interquartile range, i.e. the distance between U75 and U25.

As for O_3, there is a well-defined maximum in April and a minimum in October, when the irradiance time is shorter and the solar zenith angle is large. However, this does not explain the April maximum (based on irradiances alone, one would expect it in summer). Indeed, atmospheric circulation has to be taken into account. Natural atmospheric cycles (e.g. quasi-biennial oscillation, ENSO, Arctic and Antarctic oscillations, solar cycle, etc.) have been found to affect the levels of the total ozone in the atmospheric column (Coldewey-Egbers et al. 2022). Since these cycles have different periods, it is rather difficult to assess the influence of each of them on total O_3.

However, it seems clear that the Brewer-Dobson circulation has a key role in the global distribution of total ozone (Rosenlof 1995; Plumb and Eluszkiewicz 1999; Butchart et al. 2006). Total O_3 varies strongly with latitude over the globe, with the largest values occurring at middle and high latitudes during most of the year. This distribution is the result of the large-scale circulation of air in the stratosphere that slowly transports ozone-rich air from high altitudes in the tropics, where ozone production from solar ultraviolet radiation is largest, towards the poles. Ozone accumulates at middle and high latitudes, increasing the vertical extent of the ozone layer and, at the same time, total ozone. The total column of O_3 is generally smallest in the tropics for all seasons (Ross et al., 2023).

Total ozone also varies with season. During spring, it exhibits maxima at latitudes poleward of about 45º N in the Northern Hemisphere and between 45º and 60º S in the Southern Hemisphere. These spring maxima are a result of increased transport of ozone from its source region in the tropics toward high latitudes during late autumn and winter. This poleward ozone transport is much weaker during the summer and early autumn periods and is weaker overall in the Southern

Table 5.1.1.1: Statistic parameters that quantify the inter-annual behaviour of AOD_{320} (a) and total O_3 (b). x represents the mean, $\sigma(x)$ the corresponding standard deviation, $< x >$ the median, U25 and U75 the 25th and 75th percentiles, respectively, N the number of days and M the number of months with available data. The Total row represents the averages for the whole year for these magnitudes.

a)

	AOD_{320}	$\sigma(AOD_{320})$	$< AOD_{320} >$	$U25$	$U75$	N	M
JAN	0.16	0.05	0.16	0.13	0.18	456	31
FEB	0.19	0.07	0.19	0.13	0.25	474	31
MAR	0.26	0.09	0.25	0.21	0.29	608	31
APR	0.36	0.11	0.36	0.26	0.43	628	31
MAY	0.32	0.08	0.31	0.26	0.38	669	31
JUN	0.33	0.08	0.30	0.28	0.39	682	30
JUL	0.36	0.09	0.35	0.29	0.41	728	30
AUG	0.39	0.11	0.36	0.31	0.46	733	31
SEP	0.30	0.10	0.31	0.21	0.37	642	31
OCT	0.21	0.07	0.20	0.16	0.23	606	31
NOV	0.18	0.06	0.20	0.13	0.22	461	31
DEC	0.15	0.07	0.13	0.11	0.18	387	31
TOTAL	0.27	0.08	0.26	0.21	0.32	7074	370

b)

	$O_3\,(DU)$	$\sigma(O_3)(DU)$	$< O_3 > (DU)$	$U25\,(DU)$	$U75\,(DU)$	N	M
JAN	335	17	336	325	344	665	31
FEB	358	20	355	343	372	673	31
MAR	366	16	366	353	379	801	31
APR	364	16	367	352	374	808	31
MAY	352	12	352	342	359	831	31
JUN	334	8	334	326	340	819	30
JUL	322	8	321	315	328	873	30
AUG	306	9	305	299	313	853	31
SEP	294	11	292	286	298	784	31
OCT	281	9	281	275	286	763	31
NOV	289	11	288	283	293	647	31
DEC	307	15	306	299	313	572	31
TOTAL	326	13	325	317	333	9089	370

Hemisphere (Ross et al., 2023). This natural seasonal cycle can be clearly observed in Figure *5.1.1.4b.*

Furthermore, it has been reported that the Dobson circulation seems to have accelerated during the last years due to the increased presence of greenhouse gases in the atmosphere (Braesicke et al., 2003; Butchart et al., 2006). In any case, the results in Figure *5.1.1.4b* are in agreement with the plots provided by Environmental Canada based on 1978-1988 mean level estimates of total O_3 from the Total Ozone Mapping Spectrometer (TOMS).

3. Analysis of the trends in AOD and total O_3.

In this section, the series of the AOD and total ozone over the years has been studied in order to find out the time evolution of these magnitudes. Firstly, a preliminary study has been carried out based on the representation of the annual means of the magnitudes, so as to identify the possible increasing or decreasing trend. The data points have been fitted using the linear regression method, which has been used in order to draw conclusions about their behaviour. The next step was to apply a more sophisticated analysis, the Mann-Kendall test (Mann 1945, Kendall 1976, Gilbert 1987), which serves as an indicator of the significance of the trend; and Sen's slope (Sen, 1968), which quantifies the value of the increasing or decreasing trend.

Figures 5.1.1.5a and 5.1.1.5b represent the corresponding linear fits, and Table 5.1.1.2 summarises the value of the parameters obtained in the fit for AOD_{320} and total O_3. When carefully reviewing the data set, one can observe a considerable lack of records from November to February. Therefore, in order to account equally for the contribution of each month, weighted means have been employed. The weight for the month X has been assigned by taking into account the number of days in this month, n_X, and the total number of days in a year, 365. Then, $w_X = n_X/365$. Thus, for the annual fit, the contribution of each month to each magnitude has been determined by multiplying the monthly means of the magnitudes by the corresponding weight. Then, these contributions are summed for each year, obtaining the weighted mean. Note that for this analysis the medians for the years 1993 and 2024, which were incomplete and therefore not representative, have been removed.

Based on the behaviour previously observed for AOD and total O_3, the data have been classified by meteorological seasons, in order to detect any seasonal trends. This way, Spring considers data from March to May; Summer from June to August; Autumn from September to November; and Winter from December to February. Hence, an analysis of the time evolution of the magnitudes based on the meteorological seasons is also performed. In this case, the weight for the season Y, which covers 3 months X_i, each with n_{X_i} days ($i = 1, 2, 3$), is defined as the vector $w_Y = n_{X_i}/\sum_i n_{X_i}$. Then, the mean AOD and total O_3 of each month is multiplied by their corresponding weight in w_Y. The annual seasonal weighted mean is finally obtained by summing the contribution of the three corresponding months for each year. Focusing on Figure 5.1.1.5a, AOD_{320} clearly shows a decreasing trend, in agreement with Figure 5.1.1.3a. Indeed, the decrease in AOD is observed throughout the year (Table 5.1.1.2), so it may be significant. As previously mentioned, the main cause of this decrease could be the establishment of regulation policies for the emission of anthropogenic aerosols. Statistically significant AOD decreasing trends were also reported by Garcia-Suñer et al. (2024) in Burjassot and Aras de los Olmos (Eastern Spain) (see also Section 5.3). On the other hand, total O_3 does not seem to follow any clear trend (Figure 5.1.1.5b).

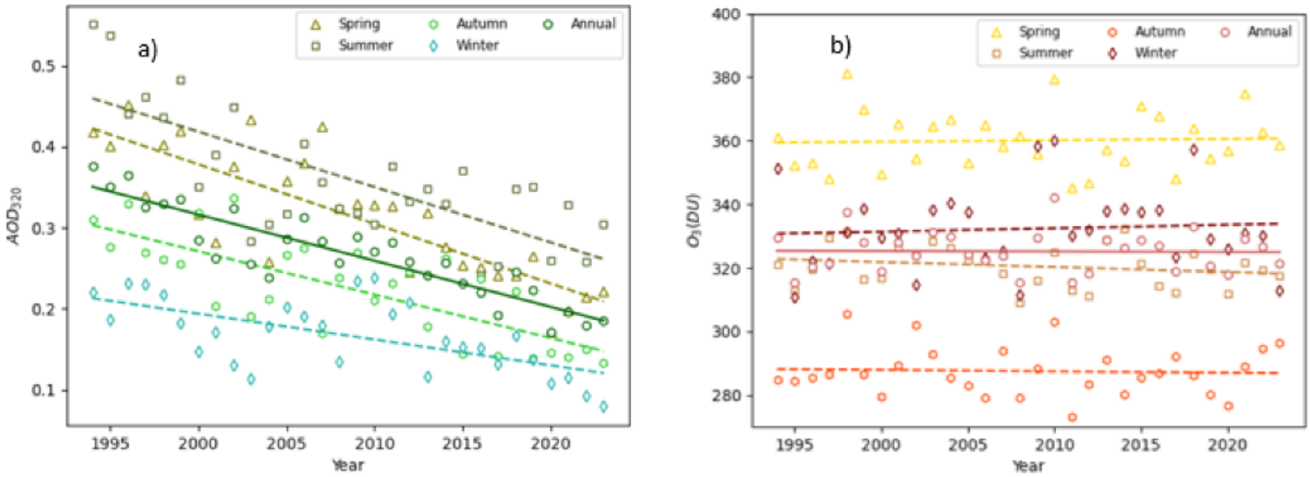

Figure 5.1.1.5: Study of AOD_{320} (a) and total O_3 (b) seasonal trends using linear regressions, represented by dashed lines. Triangles indicate spring, squares summer, hexagons autumn and diamonds winter means. The circles and the solid line illustrate the annual data points and trend, respectively. Since the dataset corresponding to years 1993 and 2024 is incomplete, the corresponding weighted means are removed from this analysis.

Table 5.1.1.2: Parameters resulting from the linear regression analysis (y = a x + b) of the annual and seasonal AOD_{320} and total O_3.

	AOD_{320}		O_3	
Seas	**a (decade^{-1})**	**R^2**	**a (DU/decade)**	**R^2**
SPR	-0.07	0.69	0.4	0.002
SUM	-0.07	0.57	--1.6	0.05
AUT	-0.05	0.58	-0.4	0.002
WIN	-0.03	0.39	1.1	0.005
TOT	-0.06	0.82	-0.13	0.0003

Therefore, it seems that these results correspond to natural fluctuations and are not significant enough to be associated with a trend in the behaviour of the magnitude, as shown in Figure 5.1.1.3b. As can be seen in Table 5.1.1.2, the R^2 values, which are an indicator of the goodness of the fit, are quite small for O_3. Conversely, in the case of AOD_{320}, these values are closer to 1, as the corresponding means follow a clear decreasing trend.

Table 5.1.1.3: Parameters resulting from the linear regression analysis (y = a x + b) of the AOD_{320} for each month of the year. In addition, results from the Mann-Kendall test have also been included. In particular, Z is the statistic of the Mann-Kendall test, and S stands for Sen's slope. Every Z value has been highlighted in bold, as they represent statistical significant trends at least at 95% confidence level ($|Z| > 1.960$).

Month	a (decade^{-1})	R^2	Z	S (decade^{-1})
JAN	-0.02	0.16	**-2.2**	-0.02
FEB	-0.04	0.30	**-2.8**	-0.04
MAR	-0.07	0.42	**-4.2**	-0.06
APR	-0.09	0.49	**-3.8**	-0.09
MAY	-0.07	0.57	**-4.6**	-0.07
JUN	-0.06	0.42	**-3.2**	-0.05
JUL	-0.06	0.33	**-3.1**	-0.06
AUG	-0.08	0.42	**-3.4**	-0.08
SEP	-0.07	0.36	**-3.6**	-0.07
OCT	-0.05	0.51	**-4.2**	-0.05
NOV	-0.04	0.41	**-3.1**	-0.04
DEC	-0.03	0.19	**-2.1**	-0.02

Finally, Table 5.1.1.3 summarises the results obtained when fitting the time evolution of AOD_{320} annual means for each month of the year through the linear regression method. As expected, the trend is decreasing for all months. Furthermore, the slopes corresponding to spring and latter summer months are steeper than for the rest of the year, although the corresponding R^2 in summer are smaller when compared to R^2 values for spring and autumn. The results from the Mann-Kendall test and the corresponding values of Sen's slope have been also included in Table *5.1.1.3*. Notice that all months exhibit statistical significant AOD decreasing trends at least at 95% confidence level. Therefore, it can be stated that the AOD significantly decreases over the years. It is important to remark on the agreement found between Sen's slope values and the slopes obtained for each month based on the linear regression analysis.

4. ***Analysis of the dependence of total O_3 with the tropopause height.***

Several studies have focused on assessing to which extent changes in total O_3 depend on variations in tropopause height (Steinbrecht et al. 1998, Varotsos et al. 2004, Coldewey-Egbers et al. 2022). In all of them, increasing trends have been found for the tropopause height, while trends on total O_3 in the atmosphere show the opposite behaviour. In this section, the methodology followed in Steinbrecht et al. (1998) and Varotsos et al. (2004) has been applied to the data collected in Poprad-Gánovce. The previous studies focused on locations from the Northern Hemisphere (Steinbrecht et al. 1998 in Hohenpeißenberg (Germany) and Varotsos et al. 2004 in Athens (Greece)), so similar results can be expected for Poprad-Gánovce. However, the main difference between them and this study is that measurements at Poprad-Gánovce cover from 1993 to 2024; whereas Steinbrecht et al. (1998) studied data from 1967 to 1997 and Varotsos et al. (2004) from 1984 to 2002. Therefore, some differences are to be expected especially in the trends of tropopause height and total O_3.

Figure 5.1.1.6 shows the frequency distribution of the measured values of tropopause height. The occurrence frequency has been computed by dividing the number of data points in each bin by the total number of data points. To take into account the seasonality of the magnitude, data corresponding to May/June/July and November/December/January have been plotted separately. Thus, it can be seen that the distribution for Nov/Dec/Jan is slightly wider than that for

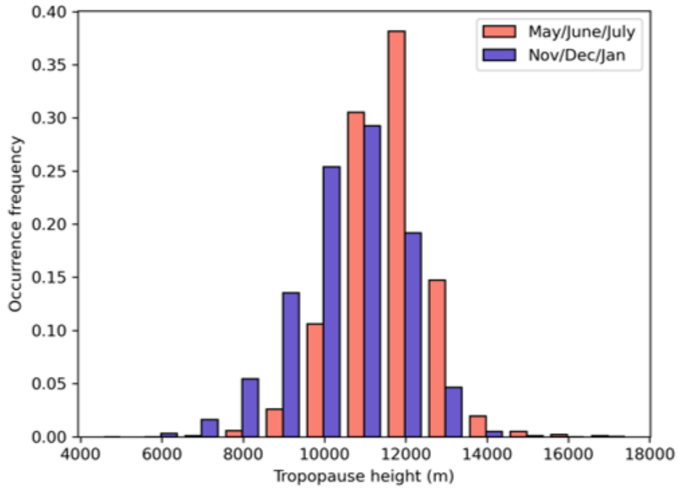

Figure 5.1.1.6: Occurrence frequency of tropopause heights for the May/June/July (red) and November/December/January (purple) periods.

May/June/July. This was also reported by Steinbrecht et al. (1998), who attributed this to more variable weather conditions in winter, which would also be the case for Poprad-Gánovce. Furthermore, as observed in these studies, the May/June/July distribution is shifted toward higher altitudes. Indeed, the corresponding maximum is at 12000 m, while for the Nov/Dec/Jan data, the maximum is at 11000 m. The same results were found in Athens by Varotsos et al. (2004), although they detected a secondary maximum, perhaps due to the influence of tropical air in summer.

Next, daily means of total O_3 and tropopause height values for the first half of 2015 have been jointly plotted in Figure 5.1.1.7. This plot serves as a preliminary study in order to visually compare the correspondence between both magnitudes. Hence, one can easily intuit the anti-correlation of both parameters: local minima in total O_3 correspond to maxima in the tropopause height and vice versa. This is indeed the expected behaviour for Eastern Europe (Coldewey-Egbers et al. 2022).

To further investigate the relationship between total O_3 and tropopause height, mean values of total O_3 have been plotted as a function of different levels of the tropopause height. The points were then fitted based on linear regression analysis, in order to parametrise their relationship. The levels have been defined in such a way that, for instance, the tropopause height values at 8 km consider the mean of the total O_3 values measured for tropopause heights in the interval [8,9) km,

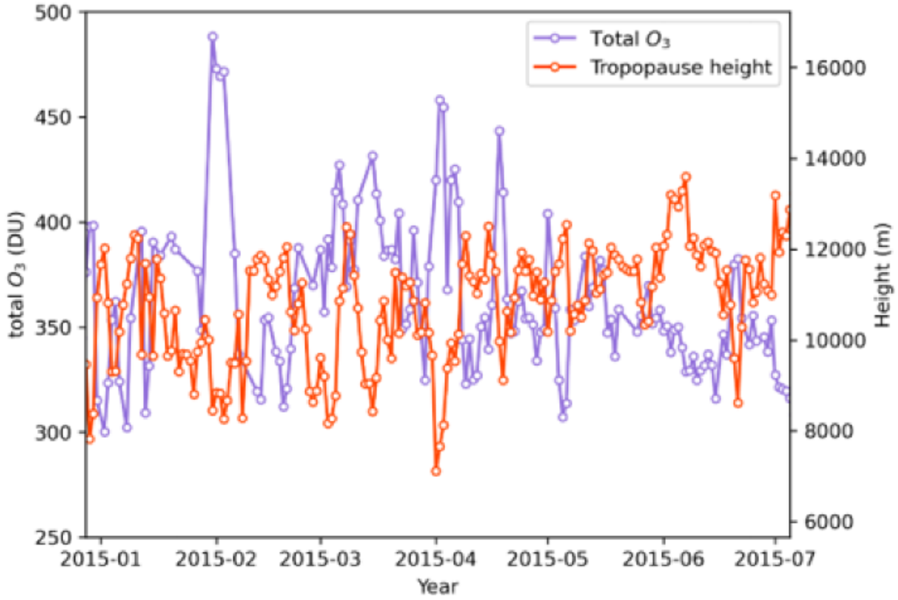

Figure 5.1.1.7: Evolution of total O_3 (violet, left y axis) and the tropopause heights (orange, right y axis) over the first half of 2015.

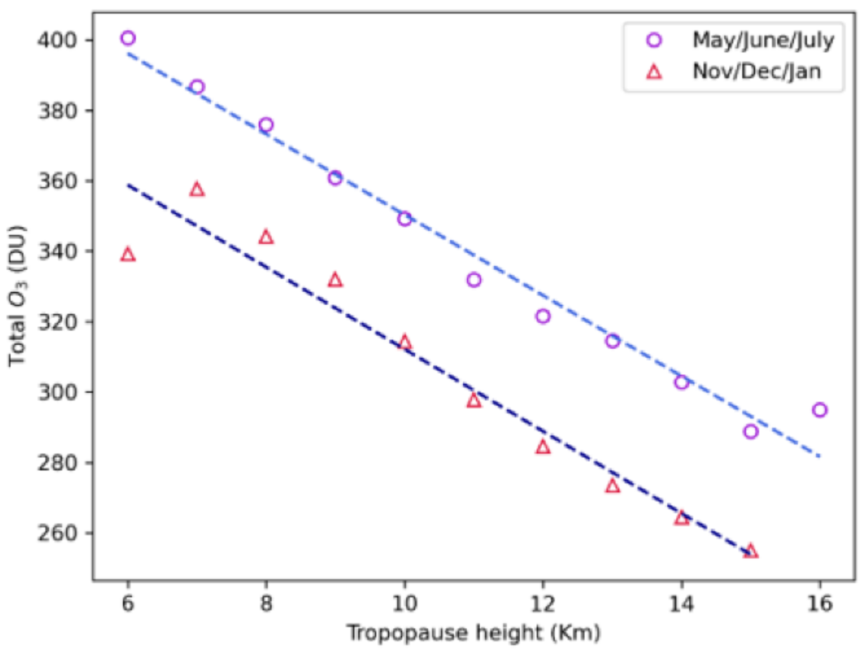

Figure 5.1.1.8: Linear fit of total O_3 means obtained for different ranges of the tropopause height, for the May/June/July (purple) and November/December/January (red) periods.

Table 5.1.1.4: Parameters resulting from the linear regression analysis (y = a x + b) of total O_3 means computed for different ranges of the tropopause height.

Months	a (DU/km)	R^2
MAY/JUNE/JULY	-11.5	0.98
NOV/DEC/JAN	-11.7	0.94

and so on. The results obtained (distinguishing between May/June/July and Nov/Dec/Jan periods) are shown in Figure 5.1.8**.** Furthermore, the slope and the R^2 parameters have been given in Table *5.1.1.4*. The slopes are of the same order as these computed employing data from Hohenpeißenberg and Athens. In fact, for the May/June/July period, Steinbrecht et al. (1998) obtained a decrease in total O_3 of 16.3 DU/km in Hohenpeißenberg, while Varotsos et al. (2004) concluded that total O_3 decreases by 8.5 $\pm$ 0.7 DU/km in Athens. In Poprad-Gánovce, the decrease is 11.5 DU/km. On the other hand, the decrease is slightly steeper in Nov/Dec/Jan (11.7 DU/km). The magnitude of the May/June/July-Nov/Dec/Jan difference of the total O_3-tropopause height in Poprad-Gánovce is similar to that in Hohenpeißenberg, where a decrease of 15.7 DU/km was found in Nov/Dec/Jan. Conversely, this difference is more significant in Athens, where the reported rate is -11.2 $\pm$ 0.5 DU/km in Nov/Dec/Jan. In any case, the slope is always negative, i.e., total O_3 decreases with the height of the tropopause.

The temporal evolution of total O_3 and the tropopause height over the full 30 years of measurement (1994-2023) has been analysed in Figures 5.1.1.9a and 5.1.1.9b, respectively. In particular, deseasonalised monthly means of these magnitudes have been plotted. These result from the difference between the monthly means and their corresponding running average value, computed taking into account a time window of 13 months (i.e. for a given month, the corresponding running mean value is given by the average of the monthly means for the previous 13 months. Thus, note that the year 1994 cannot be deseasonalised and then it has not been plotted). Then, the points are fitted based on the linear regression method. For the total O_3, the slope is -0.0068 DU/month, i.e. -0.82 DU/decade; while for the tropopause height, it is 0.15 m/month, i.e. 18 m/decade. These results differ significantly from those obtained by Steinbrecht et al. 1998 (ΔO_3 = -10 DU/decade and Δh = 150 m/decade) and Varotsos et al. 2004 (ΔO_3 = -7.5 $\pm$ 1.0 DU/decade and Δh =167 $\pm$ 30 m/decade). However, while Steinbrecht et al. (1998) worked with data from 1967 to 1997 and Varotsos et al. (2004) from 1984 to 2002, the measurements in Poprad-Gánovce reach more recent years (1994-2023). It is well known that various measures have been imposed in order to restore

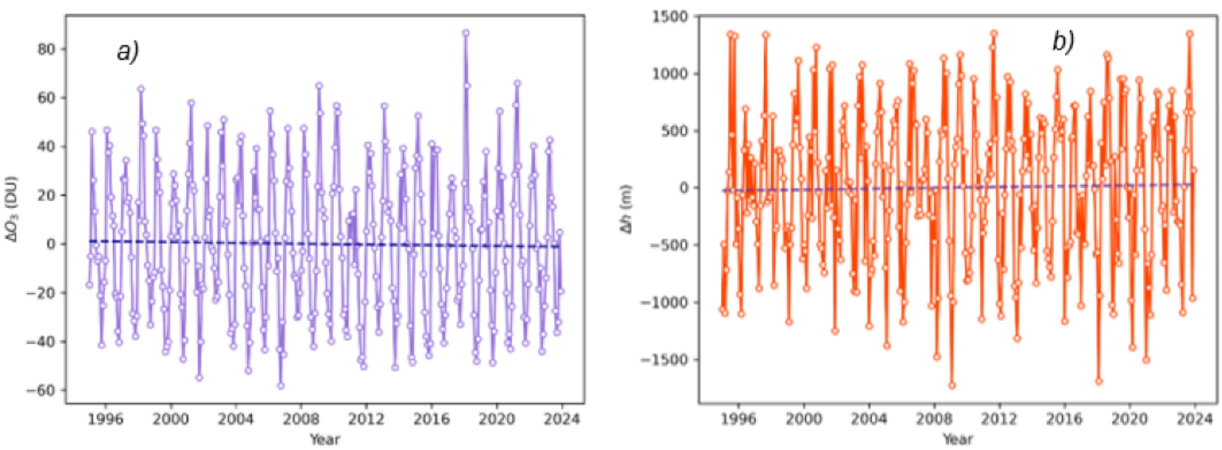

Figure 5.1.1.9: Representation of the evolution and linear fit of deseasonalised monthly means for total O_3 (a) and the height of the tropopause (b) over the years.

the ozone layer, so it might be possible that the consequences of these actions are currently noticeable as a decrease in the rate at which the total O_3 decreases and the tropopause height increases.

Following the reasoning in Steinbrecht et al. (1998) and Varotsos et al. (2004), we have assumed that the relationship between total O_3 and tropopause height (~ -12 DU/km) remains constant, so it can be applied to long time periods. Hence, if the tropopause increases by 18 m/decade, that will imply a decrease in total O_3 of 0.22 DU/decade, while it tends to decrease at a rate of 0.82 DU/decade. Therefore, the 27% of the decrease in total O_3 can be attributed to its dependence on tropopause height. This amount is similar to that found by Steinbrecht et al. 1998 (25 %) and Varotsos et al. 2004 (22%). According to these studies, the increase in the tropopause height may be due to an increase in temperature (which is favoured by the presence of greenhouse gases). This causes ozone to reach higher altitudes, triggering photochemical processes (which are favoured by increasing altitude, Brasseur and Solomon, 1984) that consume it, with the result in a decrease in total O_3 (Steinbrecht et al. 1998).

To conclude this analysis, the evolution of the means of total O_3 and the tropopause height for each month of the year over time have been briefly analysed based on the linear regression method. The corresponding results are summarised in Table 5.1.1.5, similar to Table 5.1.1.3 with AOD_{320}. Although not all months show the expected behaviour (e.g. January and May for tropopause height; and January, March, May, October and November for total O_3), it is important to notice that for the best fits (i.e. those with higher associated values of R^2) the expected trend is found. The Mann-Kendall test has also been applied to these cases. Significant increasing trends at least at 90% confidence level for the tropopause height have been found in June, July, August, September and November. However, it would not be accurate to affirm that the annual trend is significantly increasing. As for the total O_3, significant decreasing trends at least at 90% confidence level were identified in June and August. Therefore, it cannot be stated that annual trends in total O_3 are significant. These results are in agreement with the less steeped trends, in comparison to Steinbrecht et al. 1998 and Varotsos et al. 2004, found in Figures 5.1.1.9a and 5.1.1.9b. It is interesting to notice that the slopes from the linear fit are of the same magnitude as Sen's slopes, thus validating the consistency of both methods.

Table 5.1.1.5: Parameters resulting from the linear regression analysis (y = a·x + b) of the tropopause height and total O_3 for each month of the year. In addition, results from the Mann-Kendall test have also been included. In particular, Z is the statistic of the Mann-Kendall test, and S stands for Sen's slope. Those Z values indicating statistically significant trends at least at 90% confidence level ($|Z|$ > 1.645) have been highlighted in bold.

	Tropopause height				Total O_3			
Month	**a (m/decade)**	**R^2**	**Z**	**S (m/decade)**	**a (DU/decade)**	**R^2**	**Z**	**S (DU/decade)**
JAN	-60	0.02	-1.0	-112	4.6	0.06	1.2	4.1
FEB	67	0.01	0.8	105	-1.6	0.004	-0.5	-2.9
MAR	92	0.04	1.0	93	2.4	0.02	0.6	2.4
APR	78	0.03	0.8	108	-2.6	0.02	-0.9	-2.7
MAY	-31	0.005	-0.4	-24	1.4	0.01	1.2	2.8
JUN	130	0.14	**2.2**	152	-0.4	0.002	-0.5	-0.7
JUL	120	0.08	**1.6**	146	-0.7	0.007	-0.5	-1.1
AUG	200	0.23	**2.9**	219	-3.5	0.12	**-1.8**	-4.0
SEP	210	0.14	**2.1**	251	-2.8	0.05	-1.4	-3.2
OCT	130	0.06	1.5	198	-0.7	0.005	0.1	0.3
NOV	150	0.09	**1.9**	188	2.3	0.03	1.0	1.9
DEC	90	0.02	0.7	68	0.03	$3 \cdot 10^{-6}$	-0.07	-0.3

References:

Braesicke, P., and J. A. Pyle. Changing ozone and changing circulation in northern mid-latitudes (2003): Possible feedbacks? Geophys. Res. Lett., 30, 1059, doi:10.1029/2002GL015973, 2.

Brasseur, G. P. and Solomon, S. “Aeronomy of the Middle Atmosphere: Chemistry and Physics of the Stratosphere and Mesosphere.”, 441 pp., D. Reidel, Norwell, Mass., 1984.

Butchart, N., Scaife, A.A., Bourqui, M. et al. Simulations of anthropogenic change in the strength of the Brewer–Dobson circulation (2006). Clim Dyn 27, 727–741. https://doi.org/10.1007/s00382-006-0162-4

Coldewey-Egbers, M., Loyola, D. G., Lerot, C., and Van Roozendael, M.: Global, regional and seasonal analysis of total ozone trends derived from the 1995–2020 GTO-ECV climate data record (2022). Atmos. Chem. Phys., 22, 6861–6878, https://doi.org/10.5194/acp-22-6861-2022

Environmental Canada: https://exp-studies.tor.ec.gc.ca/e/ozone/normalozone.htm#nh. Last visited: 07/10/2024.

Gilbert, R.O., February 1987. Statistical Methods for Environmental Pollution Monitoring. Wiley, https://www.osti.gov/biblio/7037501

Kendall, M.G., 1975. Rank Correlation Methods. Griffin, London, https://academic.oup.com/ej/article-abstract/59/236/575/5260284

Li, J., Carlson, B. E., Dubovik, O., and Lacis, A. A.: Recent trends in aerosol optical properties derived from AERONET measurements (2014), Atmos. Chem. Phys., 14, 12271–12289, https://doi.org/10.5194/acp-14-12271-2014

Mann, H.B., 1945. Nonparametric tests against trend. Econometrica 13, 245, https://www.jstor.org/stable/1907187

Plumb RA, Eluszkiewicz J. The Brewer–Dobson circulation: dynamics of the tropical upwelling (1999). J Atmos Sci 56:868–890

Rosenlof KH. Seasonal cycle of the residual mean meridional circulation in the stratosphere (1995). J Geophys Res 100:5173–5191

Ross J. S., Laura A. McB., Chelsea R. T., Eric L. F., Richard L. McK., Karen H. R., Sarah J. D., David W. F., Twenty Questions and Answers About the Ozone Layer: 2022 Update (2023), Scientific Assessment of Ozone Depletion: 2022, 75 pp., World Meteorological Organization, Geneva, Switzerland.

Schanz, A., Hocke, K., and Kämpfer, N.: Daily ozone cycle in the stratosphere: global, regional and seasonal behaviour modelled with the Whole Atmosphere Community Climate Model (2014), Atmos. Chem. Phys., 14, 7645–7663, https://doi.org/10.5194/acp-14-7645-2014

Sen, P.K. Estimates of the regression coefficient based on Kendall's Tau (1968). J. Am. Stat. Assoc. 63 (324), 1379–1389, https://doi.org/10.1080/01621459.1968.10480934

Steinbrecht, W., Claude, H., Köhler, U., Hoinka, K.P. Correlations Between Tropopause Height and Total Ozone: Implications for Long-Term Changes. Journal of Geophysical Research (1998). 103. 19183-19192. 10.1029/98JD01929

Varotsos, C., C. Cartalis, A. Vlamakis, C. Tzanis, and I. Keramitsoglou. The Long-Term Coupling between Column Ozone and Tropopause Properties (2004). J. Climate, 17, 3843–3854, https://doi.org/10.1175/1520-0442

5.1.2. AOD and aerosol classification analyses at the Poprad-Gánovce AERONET's site (Slovakia) [Preliminary results].

Authors: Peter Hrabčák, Meritxell Garcia-Suñer, Violeta Matos, Víctor Estellés, Monica Campanelli.

In this study, AOD measurements from the Poprad-Gánovce AERONET's site (Slovakia) have been examined, following a methodology identical to Garcia-Suñer et al. 2024, summarised in section 5.3 from this report. To this end, their inter-annual and intra-annual evolution have been analysed. Then, correlations between AOD, α and CWV have been tested. Next, two methods of aerosol classification based on AOD and α parameters have been applied: Gobbi et al. (2007)'s diagram and the plot based on the limits used in Filonchyk et al. (2021). Finally, annual mean AOD_{440} trends based on the four meteorological seasons have been analysed in order to draw conclusions about the temporal evolution of this parameter. AERONET Version 3 daily averages Level 2.0 data, ranging from 12/12/2014 to 7/11/2023, have been employed.

1. Location

The research for this work specifically focuses on the location of Poprad-Gánovce (Slovakia), where a Cimel sun photometer is installed. Its coordinates are 49.03 °N, 20.32 °E, and it has an altitude of 706 m above sea level. The site is located in the Podtatranská basin, which is part of a larger geomorphological unit called the Carpathians. There are mountain units of different heights around. Gerlachovský štít (2654 m above sea level), the highest peak of the Carpathians, is located only 20 km from the station. In the presence of a larger pressure gradient, the location is relatively windy. Among the prevailing wind directions we can include west, north and south-east.

Westerly flow often brings a marine air mass originating from the Atlantic ocean, which is mostly characterised by a lower aerosol content. The flow of southern directions sometimes brings dust from the Sahara desert. In the case of the Poprad-Gánovce area, in the period 2015 – 2020, the average annual number of days with the occurrence of Saharan dust was equal to 42 (Hrabčák, 2022). More extensive forest fires have not occurred in the given location in recent years. However, in rare cases, smoke can reach the location from very distant large-scale fires. In 2016 and 2017, smoke from Canadian fires was recorded using lidar over Poprad-Gánovce, while in 2017 it was also detected in the lower stratosphere, i.e. above the tropopause. A remarkable case of long-distance transmission also occurred in 2019, and this time aerosol particles originating from the eruption of the Raikoke volcano, located in the Kuril Islands region, were detected (Hrabčák, 2019).

Among the more important local aerosol sources are the products of burning solid fuel, mainly wood in the surrounding villages and agriculture. Bare dry soil or plant products are sometimes blown away by the wind, as the location is relatively windy. The proximity of the city of Poprad (approx. 1.5 km) with approx. 50 000 inhabitants and various industrial activities also plays a role. In spite of the proximity of the mentioned city, the area can, in general, be deemed rural with respect to the anthropogenic impact.

2. Inter-annual evolution of AOD

In this section, the evolution of daily, monthly and annual AOD_{440} means over the years has been examined. These are illustrated in Figures 5.1.2.1a, b and c, respectively. A clear pattern can be identified in Figures 5.1.2.1a and 5.1.2.1b: AOD_{440} increases over the first half of the year, reaching its maximum in summer months (although some important maxima can also be detected in spring for some years, namely 2016 and 2019). Then, during the second half of the year, AOD_{440} decreases, in such a way that minima values are found in January and December months.

On the other hand, Figure 5.1.2.1c does not provide enough information in order to draw concise conclusions: annual AOD_{440} means show certain dispersion, and no clear trend can be visually identified. That is why AOD trends have been thoroughly examined in a further section. Notice, however, that the small value of AOD_{440} in 2014 is related to the fact that only data from December (when AOD levels are smaller in comparison to the rest of the year) are available, so this data point is not a valid representation of the year. Thus, in Figure 5.1.2.1d, it has been removed.

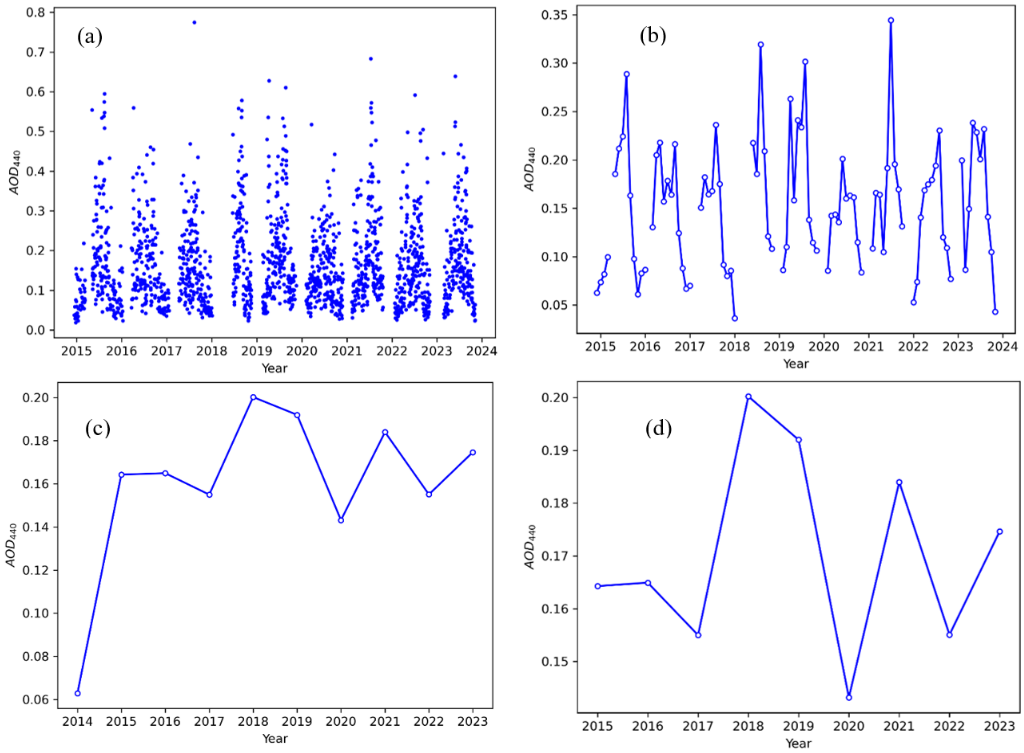

Figure 5.1.2.1: Daily (a), monthly (b) and annual (c, d) AOD_{440} means obtained using a sky sun-photometer at the Poprad-Gánovce AERONET's site (Slovakia), during the period 12/12/2014 (a, b, c) -01/01/2015 (d)- to 7/11/2023.

3. Intra-annual evolution of AOD

The evolution of AOD_{440} over the year has also been analysed. To this end, statistical parameters such as means, medians and the first and third quartiles (represented by U25 and U75, respectively), have been computed for each month taking into account the values from the whole data set corresponding to such month. Thus, Figures 5.1.2.2a and 5.1.2.2b show the results of this study, whereas Tables 5.1.2.1a and 5.1.2.1b summarise the main statistical parameters that have been calculated. In particular, the study has been based both on daily and monthly means, corresponding to Figures and Tables 'a' and 'b', respectively. Hence, both studies provide analogous results, although slightly larger values for the statistical parameters are obtained from the daily means. This is an expected result, since monthly means will smooth daily means' variations. Indeed, when comparing the standard deviations computed for both datasets (Tables 5.1.2.1a and 5.1.2.1b), it can be clearly seen that these values are larger when daily means are employed.

The seasonal patterns described in the previous section can be clearly identified in Figures 5.1.2.2a and 5.1.2.2b. Mean AOD_{440} is larger in spring and summer months: it tends to increase over the year up to August, where the maximum is reached. Furthermore, it is important to remark on the relatively large mean AOD_{440} differences between March and April months (when a secondary maximum can be distinguished). Then, a steeper decrease is observed from September to December, when the mean AOD_{440} is similar to the value in January.

This seasonal pattern could be related to the different sources of aerosols near the measurement site (especially anthropogenic particles originated in the villages of Gánovce and Poprad) in combination with other factors that favour transport, stagnation, secondary aerosol formation and/or growth; such as air masses, solar irradiance, orography, atmospheric dynamics, temperature or precipitation. In addition, according to Gammoudi et al. (2024), spring is the time of the year when the greatest number of dust intrusion cases are usually reported in Central Europe, followed by summer. This could explain the presence of the secondary AOD peak in April (Figures 5.1.2.2a and 5.1.2.2b). In addition, it can be noticed that mean and median AOD_{440} values are not coincident in February, April and July (in this case, we are referring to the study performed using monthly means, since given its characteristic dispersion, it is not unusual for this behaviour to be observed in daily means). Hence, it could be hypothesised that these occasional dust outbreaks occurring in relatively short periods of these months could have yielded unusually larger values of

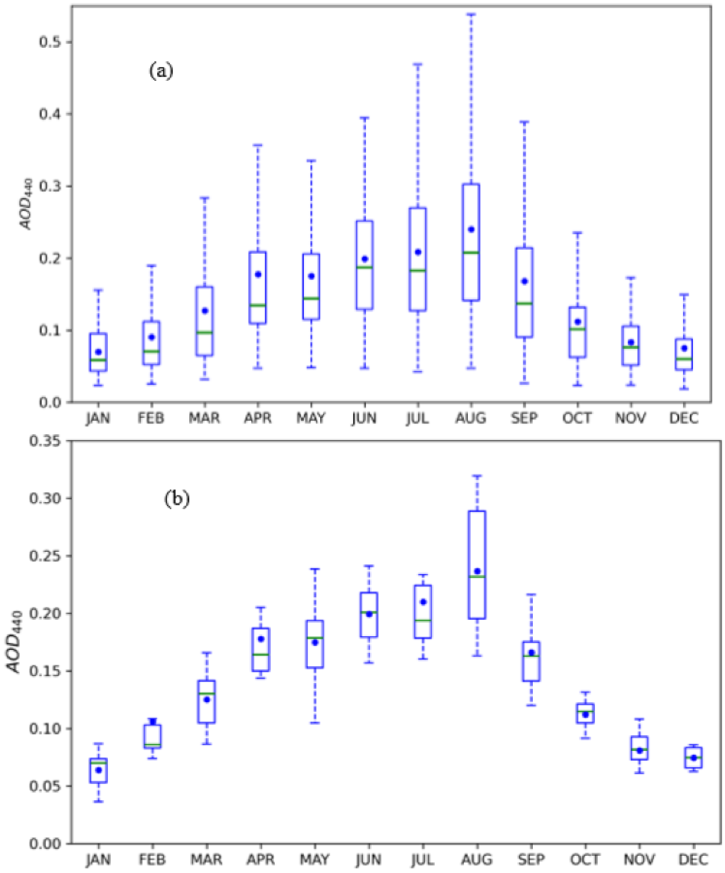

Figure 5.1.2.2: Boxplot showing the intra-annual evolution of AOD_{440} at the Poprad-Gánovce AERONET's site (Slovakia), obtained from daily (a) and monthly (b) means. Solid points represent mean values, meanwhile the horizontal lines indicate the medians. Lower and upper limits of the boxes portray the first (U25) and third (U75) quartiles, respectively. In addition, the lower and upper whiskers account for U25-1.5IQR and U75+1.5IQR, respectively, where IQR stands for the interquartile range, i.e. the distance between the third and the first quartiles.

AOD_{440}, thus increasing the corresponding mean AOD_{440}. This seasonal behaviour is similar to the ones found in other sites we have analysed in Europe. With respect to the winter season, it is more humid, cold and thus cloudy than summer, so it seems consistent that fewer days of data were available in comparison with summer.

Table 5.1.2.1: AOD_{440} means (AOD), standard deviation (σ), medians (<AOD>), first and third quartiles (U25 and U75, respectively), and number of days and months with data (N and M, respectively) from the retrievals at Poprad-Gánovce AERONET's site (Slovakia), for the 12/12/2014 to 7/11/2023 period, computed using daily (a) and monthly (b) means. TOTAL refers to the mean annual value for each parameter (for instance, mean annual AOD_{440} is 0.14 ± 0.03); except in the cases of N and M, where it is the sum.

(a) Month	AOD	σ	<AOD>	U25	U75	N	M
JAN	0.07	0.04	0.06	0.04	0.10	28	5
FEB	0.09	0.07	0.07	0.05	0.11	74	6
MAR	0.13	0.09	0.10	0.06	0.16	137	7
APR	0.18	0.11	0.13	0.11	0.21	134	7
MAY	0.18	0.10	0.14	0.12	0.21	180	8
JUN	0.20	0.09	0.19	0.13	0.25	203	9
JUL	0.21	0.12	0.18	0.13	0.27	249	9
AUG	0.24	0.13	0.21	0.14	0.30	238	9
SEP	0.17	0.10	0.14	0.09	0.21	194	9
OCT	0.11	0.07	0.10	0.06	0.13	161	9
NOV	0.08	0.04	0.08	0.05	0.11	92	8
DEC	0.08	0.04	0.06	0.05	0.09	54	4
TOTAL	0.14	0.08	0.12	0.09	0.18	1744	90

(b) Month	AOD	σ	<AOD>	U25	U75	N	M
JAN	0.06	0.02	0.07	0.05	0.07	28	5
FEB	0.11	0.05	0.09	0.08	0.10	74	6
MAR	0.13	0.03	0.13	0.10	0.14	137	7
APR	0.18	0.04	0.16	0.15	0.19	134	7
MAY	0.17	0.04	0.18	0.15	0.19	180	8
JUN	0.20	0.03	0.20	0.18	0.22	203	9
JUL	0.21	0.06	0.19	0.18	0.22	249	9
AUG	0.24	0.06	0.23	0.20	0.29	238	9
SEP	0.17	0.03	0.16	0.14	0.18	194	9
OCT	0.11	0.01	0.11	0.10	0.12	161	9
NOV	0.08	0.02	0.08	0.07	0.09	92	8
DEC	0.07	0.01	0.07	0.07	0.08	54	4
TOTAL	0.14	0.03	0.14	0.12	0.16	1744	90

4. Correlation among the aerosol retrieved parameters: AOD, α and CWV

Figures 5.1.2.3a, 5.1.2.3b and 5.1.2.3c depict the scatter plots obtained when representing $\alpha_{440-870}$ versus AOD_{440}, AOD_{440} vs CWV, and $\alpha_{440-870}$ vs CWV daily means, respectively. The aim of these plots is to serve as a first approach for visually identifying correlations between these parameters. Then, from Figure 5.1.2.3a, it can be observed that the aerosol burden over this site is composed mainly of fine particles ($\alpha_{440-870}$ ≥ 1) mostly related to low turbidity (AOD_{440} ≤ 0.3). However, some of these fine particles are associated with high AOD values (0.3 <AOD_{440} ≤ 0.8). In turn, coarse particles ($\alpha_{440-870}$ < 1) are generally related to lower AOD values (0 < AOD_{440} ≤ 0.5).

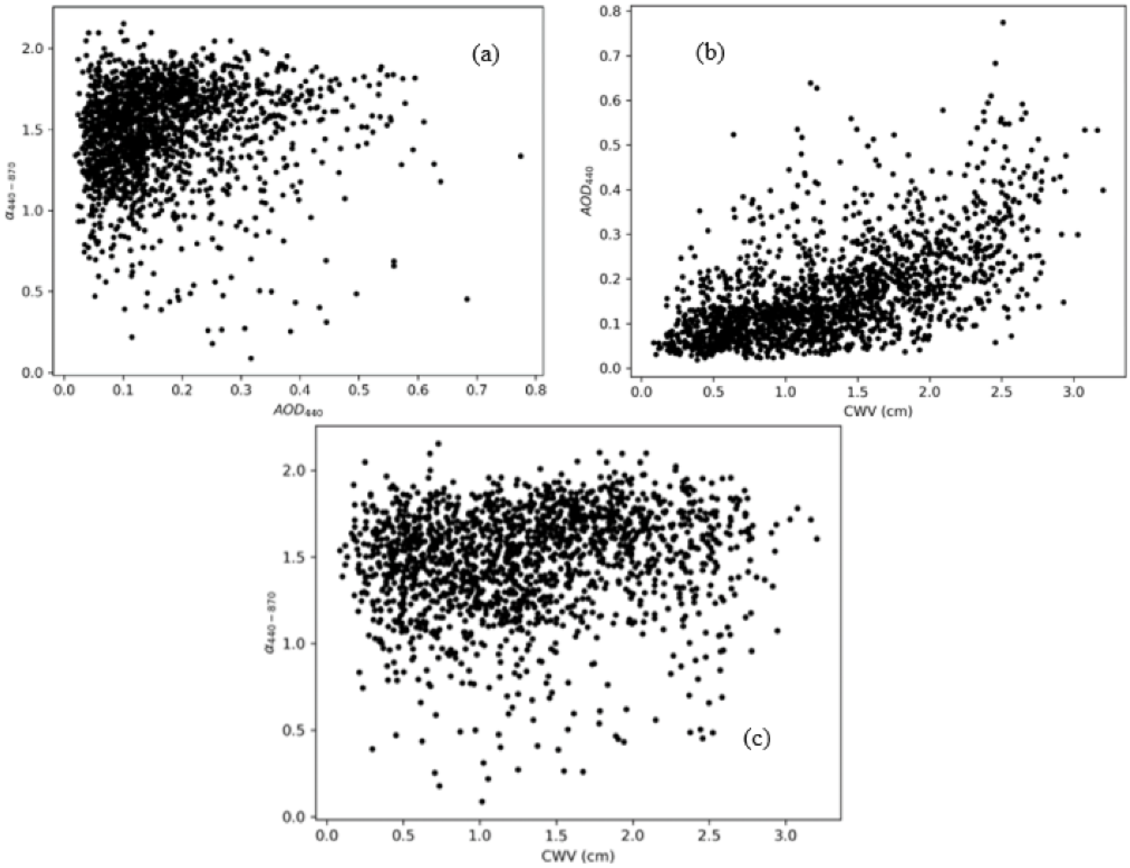

Figure 5.1.2.3: Scatter plots drawn to study correlations between $\alpha_{440-870}$ and AOD_{440} (a), AOD_{440} and CWV (b); and $\alpha_{440-870}$ and CWV (c).

A clear correlation can be identified between AOD and CWV. Indeed, from Figure 5.1.2.3b, it can be concluded that the larger the content of water vapour in the atmospheric column, the larger the turbidity. This result could constitute an indicator of the presence of hygroscopic aerosols, since these would tend to absorb this water, increasing their size (thus lowering $\alpha_{440-870}$) and then dispersing solar radiation more efficiently. Contrary to the previous plots, no definite conclusion can be drawn from Figure 5.1.2.3c. As previously mentioned, it seems that fine particles are the majority, but they are not associated with particular values of CWV. Furthermore, it can be suggested that hygroscopic particles do not usually experience a significant growth when absorbing water, since this would imply that the lower the $\alpha_{440-870}$, the larger the CWV, but this is not the case.

5. Aerosol classification

In this section, two aerosol classification methods will be applied in order to distinguish among different aerosol types: Gobbi's method and the limits in $\alpha_{440-870}$ and AOD_{440}set in Filonchyk et al. (2021).

Gobbi's diagram

This graphical method, developed by Gobbi et al. (2007), allows a clear distinction between fine and coarse particles, as well as identification of particle growth and cloud contamination cases. Figure

5.1.2.4a illustrates Gobbi's diagram drawn using the Poprad-Gánovce site's data, mostly associated with low AOD values (0.15 < AOD_{675} < 0.3). A cluster of data points can be distinguished at 70% < η < 90%, 0.1 > δα > -0.5, 1.25 < $\alpha_{440-870}$ < 2. These points seem to draw a curve towards larger R_f values (with some isolated points even reaching $R_f \approx$ 0.25 μm) while increasing η from 70 to 95%. In addition, some of them show larger AOD values (AOD_{675} up to 0.7). This behaviour could be an indicator of aerosol growth by coagulation-ageing or hydration processes. In fact, the latter hypothesis is particularly appealing taking into account the conclusions drawn in the previous section about the presence of hygroscopic particles. When reproducing Figures 5.1.2.3 for AOD_{675}, it can be seen that for most of the points, AOD_{675} < 0.3, in agreement with Figure 5.1.2.4a.
Another group of points which are worth mentioning are spread over the region 0.3 > δα > -0.25, 0 < $\alpha_{440-870}$ < 0.75, 10% < η < 30%, and 0.10 μm < R_f < 0.20 μm. These are associated with the largest values of turbidity retrieved at the measurement site (0.15 < AOD_{675} < 0.7), and would probably represent coarse particles with notable extinction power (such as dust). Indeed, slightly negative or positive δα indicate the predominance of coarse mode aerosols (Kaufman, 1993).
Finally, it will be interesting to focus some attention on the region defined by 30% < η < 70%, 0 < δα < 0.8, 0.75 < $\alpha_{440-870}$ < 1.7, and 0.15 μm < R_f < 0.05 μm. Points in this area (which are related to low turbidity: 0.15 < AOD_{675} < 0.3) represent a mix of coarse and fine mode particles, with apparent predominance of the latter, since most of them are concentrated around values of $\alpha_{440-870}$ greater than 1. These fine mode particles may probably be anthropogenic aerosols originated either in urban nuclei near the measurement site, or having been transported there by air masses.

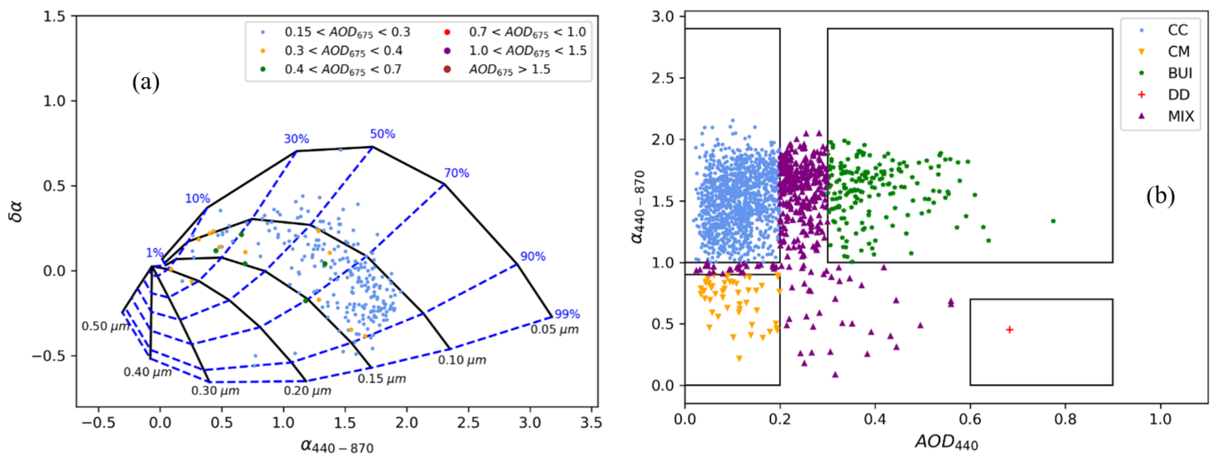

Figure 5.1.2.4: Aerosol classification: (a) Gobbi diagram for the Poprad-Ganovce site, obtained by plotting AOD_{675} retrievals in the AdA space, constituted by δα = $\alpha_{440-675}$ - $\alpha_{675-870}$ values as a function of $\alpha_{440-870}$. Solid black lines indicate constant values of the fine modal radius, R_f; whereas dashed blue lines represent constant values of the ratios of the fine mode to total AOD at 675 nm, η. (b) Distinction between aerosol types according to the values of AOD_{440} and $\alpha_{440-870}$, based on the limits in Filonchyk et al. (2021): continental clean (CC, blue points), clean marine (CM, yellow inverted triangles), biomass burning/urban/industrial (BUI, green stars), desert dust (DD, red pluses) and mixed aerosols (MIX, purple triangles).

Classification based on Filonchyk et al. (2021)

There exist a considerable number of aerosol classification techniques based on the different optical and physical parameters that characterise them, as well as on different methodologies. In this subsection, a simple yet effective classification focused on establishing thresholds for $\alpha_{440-870}$ and AOD_{440} is applied in order to distinguish among the following aerosol types: continental clean (CC), clean marine (CM), biomass burning/urban industrial (BUI), desert dust (DD) and mixed (MIX) (Filonchyk et al. (2021)). Results from this analysis are depicted in Figure 5.1.2.4b.

Thus, CC would be the most abundant aerosol type (66.23 %), which is an expected result taking into account the rural character of the area. The contribution of MIX aerosols (20.24%), as well as BUI (10.61%) is also important. The former type refers to the presence of particles from different sources yielding (AOD_{440},$\alpha_{440-870}$) pairs which are not enclosed by set limits. On the other hand, BUI particles mostly originate from anthropogenic sources which, according to the site characteristics, could probably be products of household heating systems or industrial activities.

Coarse aerosols constitute the minority types: 2.87% of data points were classified as CM, while only 0.06% of them were considered as DD. Regarding CM particles, although Slovakia is located far from the ocean, air masses coming from the Atlantic could have reached the measurement site, conveying traces of marine aerosols with them. However, coarse particles yielding low extinction (namely dust from agricultural and quarrying activities) would also be classified into this particle type, so their identification is uncertain. Similarly, air masses coming from Africa could have transported dust to the measurement site. Nevertheless, unless the burden of local aerosols was low, these particles would not have been classified as DD, but likely as MIX.

6. Aerosol AOD trends

Whenever several years of data are available from a particular site, it becomes rather interesting to analyse the temporal trends for the different variables. Indeed, studying their evolution is an essential task taking into account the important yet still undetermined role of aerosols in the Earth's radiative budget. This section constitutes a first approach so as to study the evolution of AOD_{440} over the measurement years: annual AOD_{440} weighted means will be fit through the linear regression method, so the corresponding increasing/decreasing slopes will be regarded as a rough indicator of this parameter's evolution. In particular, AOD_{440} seasonal (as well as annual) evolution will be studied. The use of weighted means is motivated by the existence of numerous gaps in the data. The weights are set according to the number of days in each month, analogous to subsection 3 of the Brewer ozone spectrophotometer study (section 5.1.1 in this report).

The results of this analysis are shown in Figure 5.1.2.5. In addition, the parameters of the fitted lines are summarised in Table 5.1.2.2. As it can be observed, AOD_{440} tends to decrease in summer and autumn, being the diminution in autumn slightly steeper than in summer. However, it tends to increase in spring and especially in winter. In fact, the overall trend is slightly positive. These results seem to contradict the latest findings in Europe (e.g. Li et al. (2014)). Nevertheless, it is important to take into account that these are preliminary findings. In addition, the scarceness of data points

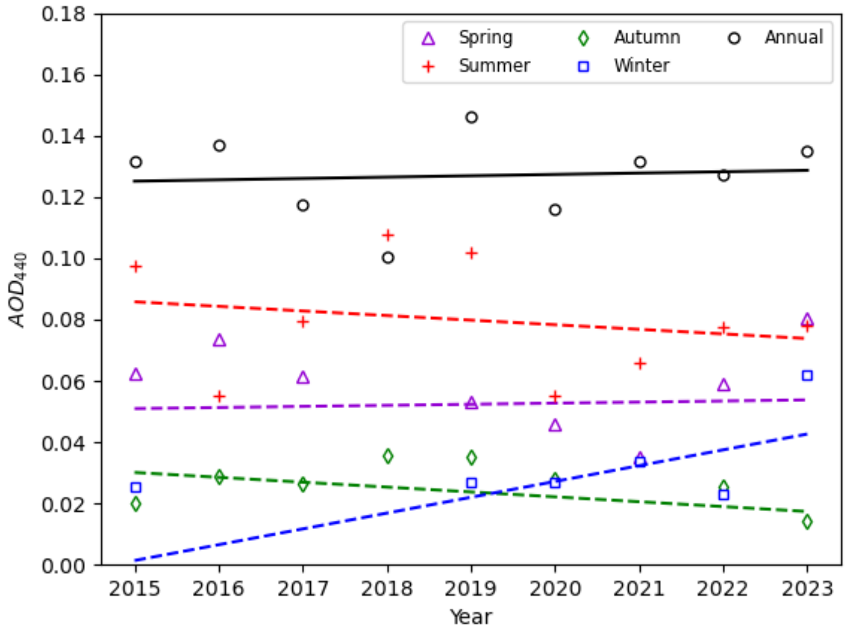

Figure 5.1.2.5: Study of seasonal AOD_{440} trends using linear regressions. Note that the year 2014 has been ruled out because there is only one available month of data.

significantly determines AOD_{440} trends. Therefore, the winter increasing trend might be related to the fact that there are only 6 available annual means, determined based on few data points. The spring and autumn series also have 1 whole month with no available data. Hence, these results are not considered definite and require further research in order to clarify this question. In particular, expanding the data set period and contrasting the findings with measurements from other instruments (for instance, Brewer spectrophotometer), would be a good starting point. In any case, it is important to take into account that the increasing annual AOD_{440} that has been reported at this site is not significant in comparison with the seasonal trends.
On the other hand, as can be observed in Table 5.1.2.2, the obtained R^2 values are rather far from 1. Hence, in order to shed light on the previous issues, these require to be thoroughly investigated. In addition, more sophisticated techniques, such as the Mann-Kendall test and Sen's slope, could be applied, with the aim to draw more concise conclusions about the data.

Table 5.1.2.2 Parameters of the fitted AOD_{440} weighted annual means using the linear regression model. The study has been carried out so as to analyse seasonal trends. Taking into account that the general linear equation is y = a·x + b, a represents the fitted values of the slope. The R^2 parameter has been included as an indicator of the quality of the fit.

	Spring	Summer	Autumn	Winter	Annual
$a \times 10^3$ ($year^{-1}$)	0.4	-1.5	-1.6	5	0.4
R^2	0.002	0.05	0.15	0.5	0.008

cost
EUROPEAN COOPERATION IN SCIENCE & TECHNOLOGY
Funded by the European Union

References

M. Filonchyk, M. Peterson, H. Yan, S. Yang, A. Chaikovsky, 2021. Columnar optical characteristics and radiative properties of aerosols of the AERONET site in Minsk, Belarus. Atmos. Environ., 249, 118237. 10.1016/j.atmosenv.2021.118237. ISSN 1352-2310. https://www.sciencedirect.com/science/article/pii/S1352231021000558.

N. Gammoudi, J. Kovács, F. Gresina, G. Varga, 2024. Combined use of HYSPLIT model and MODIS aerosols optical depth to study the spatiotemporal circulation patterns of Saharan dust events over Central Europe. Aeolian Research, Volumes 67–69, 100899, ISSN 1875-9637, https://doi.org/10.1016/j.aeolia.2024.100899

G.P. Gobbi, Y. Kaufman, I. Koren, T. Eck, 2007. Classification of aerosol properties derived from AERONET direct sun data. Atmos. Chem. Phys., 6, p. 01, 10.5194/acpd-6-8713-2006. https://acp.copernicus.org/articles/7/453/2007/.

Y.J. Kaufman, 1993. Aerosol optical thickness and atmospheric path radiance. J. Geophys. Res. Atmos., 98 (D2), pp. 2677-2692, 10.1029/92JD02427

J. Li, B.E. Carlson, O. Dubovik, A.A. Lacis, 2014. Recent trends in aerosol optical properties derived from AERONET measurements. Atmos. Chem. Phys., 14 (22), pp. 12271-12289, 10.5194/acp-14-12271-2014. https://acp.copernicus.org/articles/14/12271/2014/

Hrabčák, P.: Saharan dust over Slovakia in the years 2015 – 2020, Meteorological journal, volume 25, number 1, 3 – 15, ISSN 1335-339X, https://www.shmu.sk/File/ExtraFiles/MET_CASOPIS/1658950036_MC_2022-1.pdf, 2022.

Hrabčák, P.: Two remarkable cases of stratospheric aerosols over Slovakia, unreviewed contribution, Meteorological journal, volume 22, number 2, 118 – 121, ISSN 1335-339X, http://www.shmu.sk/File/ExtraFiles/MET_CASOPIS/MC_2019-2.pdf, 2019.

5.2 Comparison of AERONET and Skynet retrievals under different anemological conditions in Rome (Italy)

Based on: "Comparison of AERONET and Skynet retrievals under different anemological conditions in the urban site of Rome (Italy)" presented at the European Meteorological Society Annual Meeting, Barcelona 8-12 September 2024. Authors: Annalisa Di Bernardino, Monica Campanelli, Annamaria Iannarelli, and Stefano Casadio.

Introduction

Anemological data and aerosol optical properties in the Rome area, Italy, (Figure 5.2.1) are jointly examined in the period 01/01/2018-31/12/2022. Specifically, wind measurements collected from seven meteorological stations of the Regional Agency for the Development and Innovation of Agriculture of Lazio (ARSIAL, http://www.arsial.it/arsial/) homogeneously distributed in the region, and aerosol optical properties, AOD and SSA, measured by the two co-located Cimel CE318/AERONET and Prede POM02/SKYNET sun-sky photometers, are considered. The latter instruments are hosted at the Boundary-layer Air Quality-analysis Using Network of Instruments (BAQUNIN, https://www.baqunin.eu/, Iannarelli et al., 2022) supersite, in the urban area of Rome (41.90° N, 12.52° E).

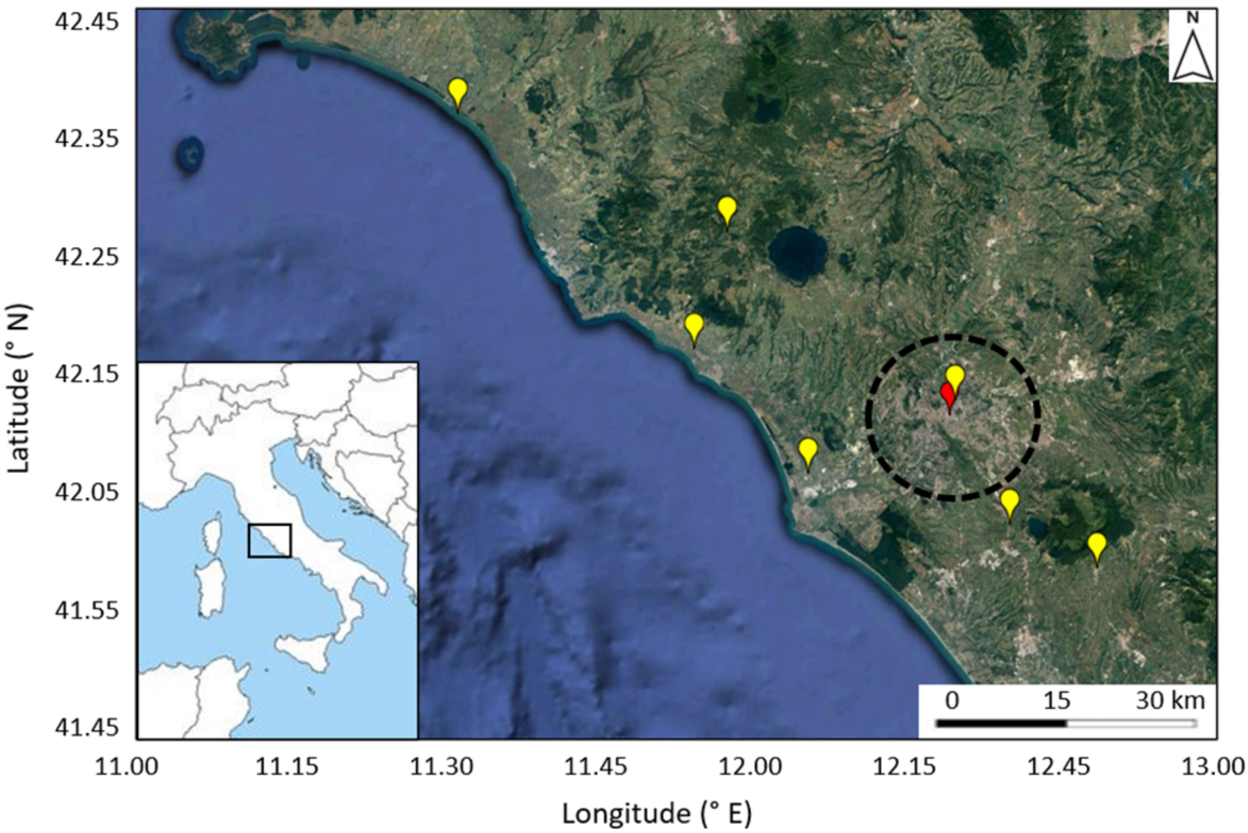

Figure 5.2.1 Geographical map of the area. The black dotted circle depicts the urban center of Rome. Yellow and red markers denote the location of weather stations and the BAQUNIN supersite, respectively

The identification of the peculiar anemological patterns was carried out by applying the k-means clustering algorithm (Hartigan and Wong, 1979) to the hourly-averaged measurements of wind intensity and direction, collected by seven surface meteorological stations affected by the sea/land breeze regime and, therefore, allowing the characterization of the atmospheric circulation on both local and synoptic scales. The method identified 4 clusters (Figure 5.2.2): i) Cluster 1: sea breeze blowing from SW; ii) Cluster 2: sea breeze blowing from S; iii) Cluster 3 persistent NE synoptic wind; iv) Cluster 4: SE wind throughout the day. It is to taken into account that generally in Rome a sea/land breeze regime of circulation is very often observed, with the sea breeze developing on average between 10:00 and 17:00 UTC (Di Bernardino et al., 2021; Di Bernardino et al., 2022) and the land breeze blowing from the NE.

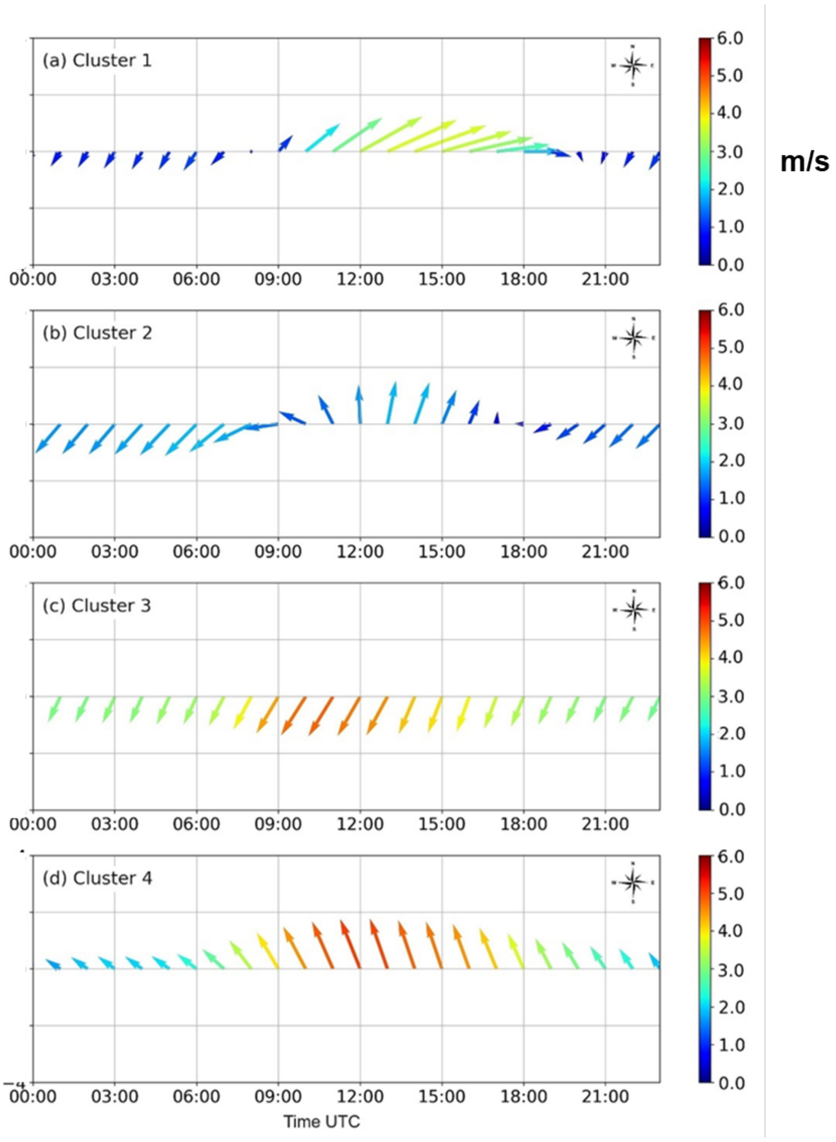

Figure 5.2.2 Daily evolution of average wind intensity; colors: m/s; Wind blowing direction: vector orientation; The distribution is obtained by averaging the hourly values of all days belonging to the same cluster.

AOD and SSA from the AERONET v3, and the Skynet Sunrad/Skrad_MRI algorithms Level 2 products were compared for each wind cluster, by selecting the days responding to the selection criteria shown in Table 5.2.1. For AOD, measurements taken within +/- 1 min from the two equipment were selected. The same threshold was not possible for SSA, because the entire 5 year dataset would be reduced to 11 points. The choice of dividing the daily AOD datasets in three time slots is related to the typical time behavior of the wind (Figure 5.2,1) and of the AOD in Rome, generally characterized by an increase in the morning after 8 UTC, due to the enhancement of the traffic activity and the growth of the mixing layer, and a decreasing one in the afternoon. The same time slot division was not possible for SSA, due to the poor number of remaining points. A second criterion, selecting only days having at least 3 values, without any threshold in time difference or time slots, for both AOD and SSA, was chosen in order to have an estimation of the AERONET and SKYNET difference but considering as the two instruments were not co-located.
Daily averages, and then monthly averages were separately calculated after the section performed with the below criteria.

AOD	SSA
1. Days having at least 3 values within +-1 min in 3 time slots: morning [<=8 UTC], noon [9-13 UTC], afternoon [>=14 UTC]	1a. Days having at least 3 values available in each day within +-1 hour
2. Days having at least 3 values in each day	2a. Days having at least 3 values in each day

Table 5.2.1: days selection criteria for Skynet and Aeronet AOD and SSA.

Scatter plot of the entire AOD dataset, without daily average and wind cluster division but selected with criterion 1, is shown in Figure 5.2.3 for the five common wavelengths of the AERONET-Cimel and SKYNET-Prede/POM02 Instruments. Mean bias deviation (MBD), Standard deviation (STD) and Root mean square deviation (RMSD) (Eqs. 5.2.1) are calculated, where τ0i and τi are AOD from the reference (AERONET) and the secondary (SKYNET) equipment, respectively, and N the number of points.

$$\mathrm{MBD} = \overline{\Delta} = \frac{1}{N}\sum_{i=1}^{N}(\tau_{0i} - \tau_i) = \frac{1}{N}\sum_{i=1}^{N}\Delta_i$$

$$\mathrm{STD} = \sqrt{\frac{1}{N}\sum_{i=1}^{N}(\Delta_i - \overline{\Delta})^2}$$

Eqs. 5.2.1

$$\mathrm{RMSD} = \sqrt{\frac{1}{N}\sum_{i=1}^{N}(\tau_{0i} - \tau_i)^2} = \sqrt{\frac{1}{N}\sum_{i=1}^{N}\Delta_i^2}$$

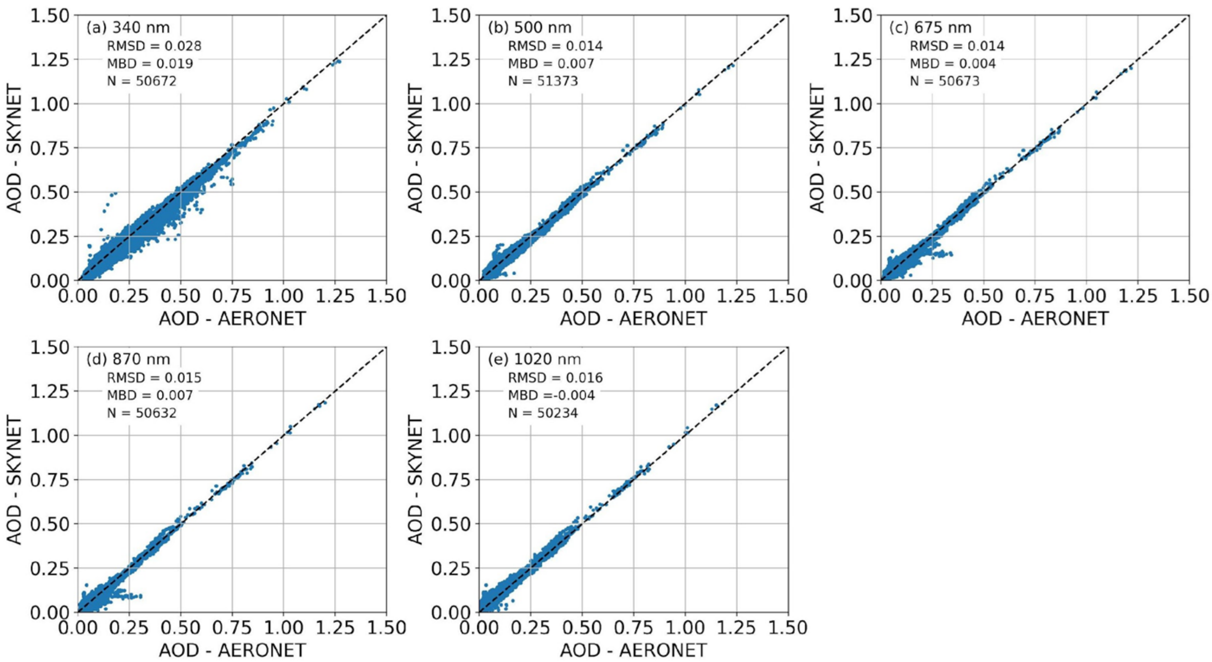

Figure 5.2.3: Scatter plot of the entire AOD dataset, screened with criterion n.1 but without any wind cluster division.N is the total number of points.

RMSD ranging from 0.028 to 0.014, and MBS from -0.004 to 0.019 are observed, assuming the highest value at 340 nm. Then, the selection criterion 1 and the cluster division was applied and the wavelength dependence of the RMSD and MBD for all the cases (Figure 5.2.4) were recalculated. RMSD and MBD, without any cluster division, range between slightly lower values (from 0.025 to 0.011 and from -0.003 to 0.017) respectively. Cluster analysis shows the greatest MBD for cluster 1 (sea breeze blowing from SW) and the smallest for cluster 3 (persistent NE synoptic wind). RMSD is very similar for all the wavelengths and cases, with the exception of 340 and 500 nm where cluster 3 has the minimum value. According to Giles et al., 2019, the AERONET field instrument AOD uncertainty is estimated to be from 0.01 to 0.02, with the maximum representing the uncertainty only in the UV channels (340 and 380 nm). These values are greater than the obtained MBD, and therefore there isn't any anemological dependence of the SKYNET-AERONET difference in terms of AOD.

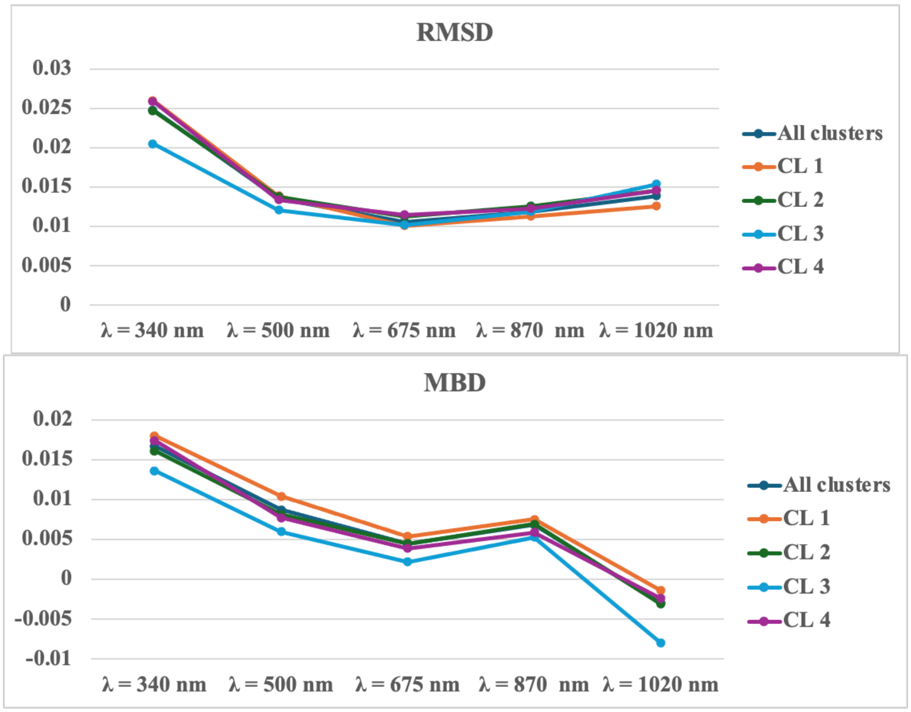

Figure 5.2.4 AOD: RMSD and MBD wavelength dependence for all the cluster and and wind clusters division, selected with the criterion 1.

The same analysis was repeated to compare SSA selecting days with criterion 1a. Only 72 measures remained and 12 days in the 5 years database, therefore the anemological analysis was not possible to be performed. Table 5.2.2a shows the RMSD and MBD for the 3 common wavelengths, and Figure 5.2.5 presents the scatter plot.

	675 nm	870 nm	1020 nm
MBD	0.010	0.003	0.004
RMSD	0.019	0.022	0.027

a)

Aerosol model	Water-soluble		Dust		Biomass burning	
AOD at 500 nm	≤ 0.2	> 0.2	≤ 0.2	> 0.2	≤ 0.2	> 0.2
Single-scattering albedo						
Near-ultraviolet	-0.07 ± 0.13	-0.01 ± 0.02	0.00 ± 0.07	0.00 ± 0.02	-0.03 ± 0.11	0.00 ± 0.02
Visible	-0.08 ± 0.14	-0.01 ± 0.02	0.00 ± 0.07	0.00 ± 0.02	-0.06 ± 0.13	-0.01 ± 0.04
Near-infrared	-0.12 ± 0.18	-0.05 ± 0.08	0.00 ± 0.06	0.00 ± 0.02	-0.13 ± 0.20	-0.05 ± 0.11

b)

Table 5.2.2: a) SSA: RMSD and MBD wavelength dependence for all the days selected with the criterion 1a; b) SSA retrieval errors from Skynet according to Kudo et al., 2021 .

According to Kudo et al., 2021 the maximum uncertainty for Skynet SSA retrieval (Tab 5.2.2b) is in the visible region is 0.08, greater than MBD in Table 5.2.2a, therefore Skynet and AERONET values are comparable.

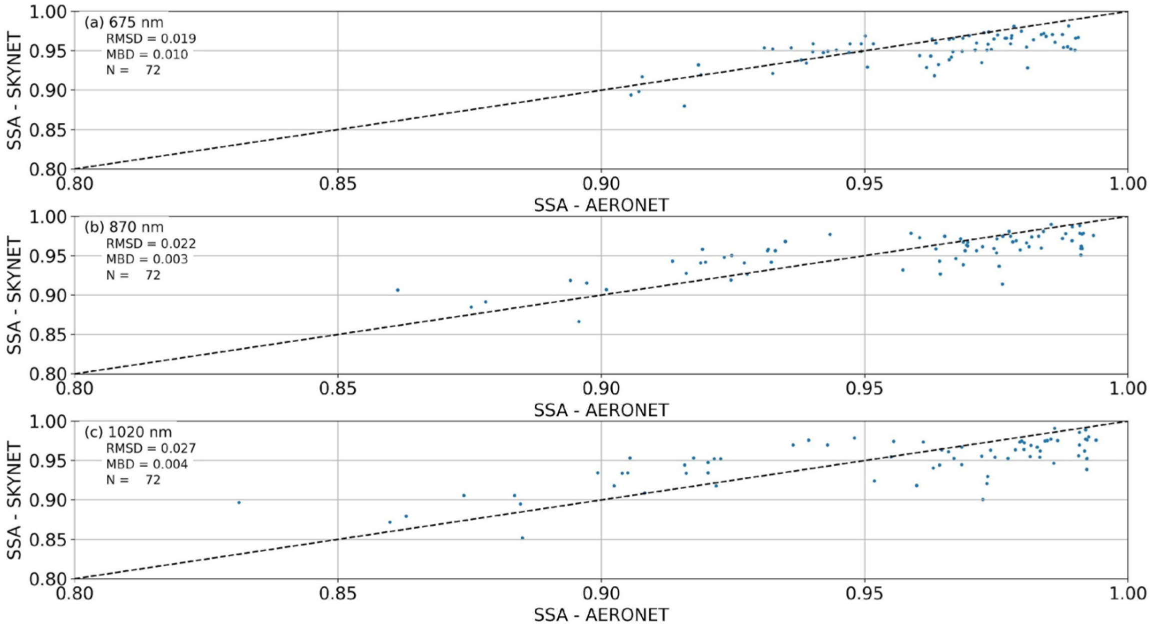

Figure 5.2.5: scatter plot og SKYNET and AERONET SSA selected according to criterion 1a.

Finally in order to understand if the monthly climatology downloadable from the AERONET web page (https://aeronet.gsfc.nasa.gov/new_web/climo_menu_new_v3.html) is comparable with the climatology from SKYNET data in Rome, monthly averages were calculated for both the databases following the 4 criteria shown in tab. 5.2.1. Results are shown in Fig 5.2.6 for AOD. It is clear that monthly average differences are many times greater than 0.02 in both the criteria n. 1 and n. 2, and that the greatest ones are not related to the difference in the number of points used to perform the monthly means. The worst comparison was found at 340 nm, whereas the best one is related to the 675 and 870 nm. The reason of this discrepancies must be investigated.

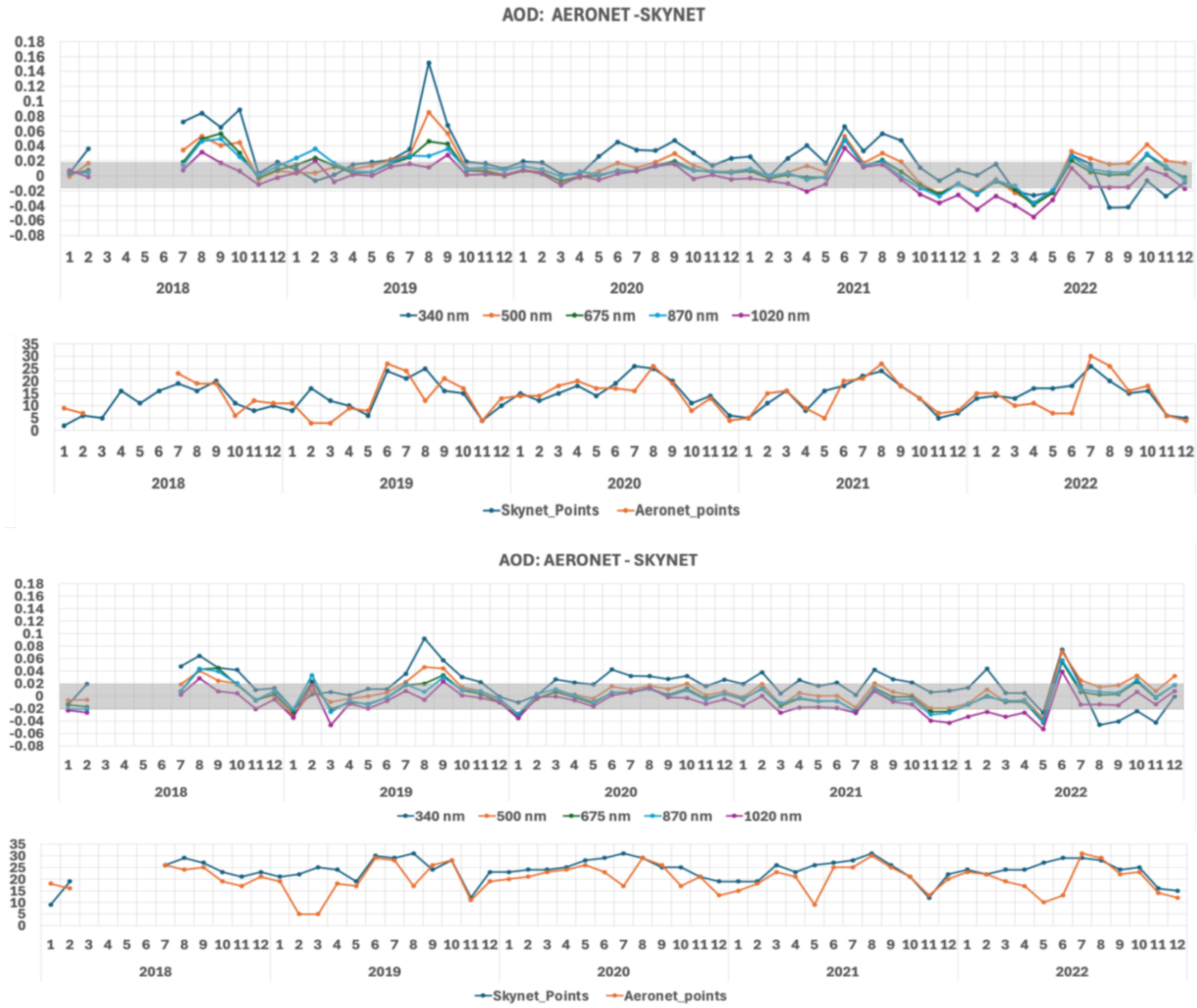

a)

b)

Fig. 5.2.6 Monthly AOD differences between AERONET and SKYNET obtained by daily selection performed with criterion n1 (a) and criterion n2 (b), described in Tab 5.2.1. Gray box represent the maximum uncertainty from Giles et al., 2018. The third and fourth plots are the number of points remaining after the selection criteria for each month.

cost
EUROPEAN COOPERATION IN SCIENCE & TECHNOLOGY
Funded by the European Union

Monthly climatologies of SSA were also compared following the criteria 2 and 2a (Tab. 5.2.1) for the daily selection and results are shown in Figure 5.2.7. Although the differences in both the cases are mostly within the maximum Skynet SSA uncertainties in the visible region (Kudo et al., 2021), the number of comparable months are very few. Moreover, the number of days used for calculating the monthly means for AERONET are very few for a good statistic, even when applying the less restrictive criterion 2a (Fig. 5.2.7, b) and, in fact, AERONET does not provide climatology for SSA, although it is very often calculated and used in climatological studies.

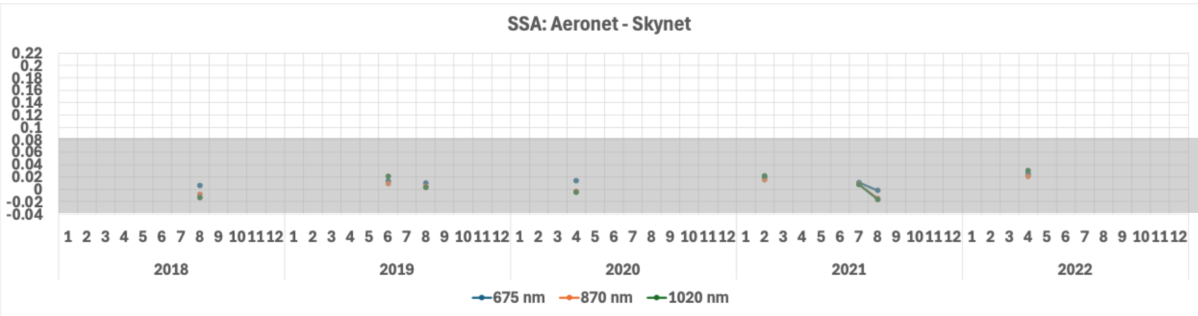

a)

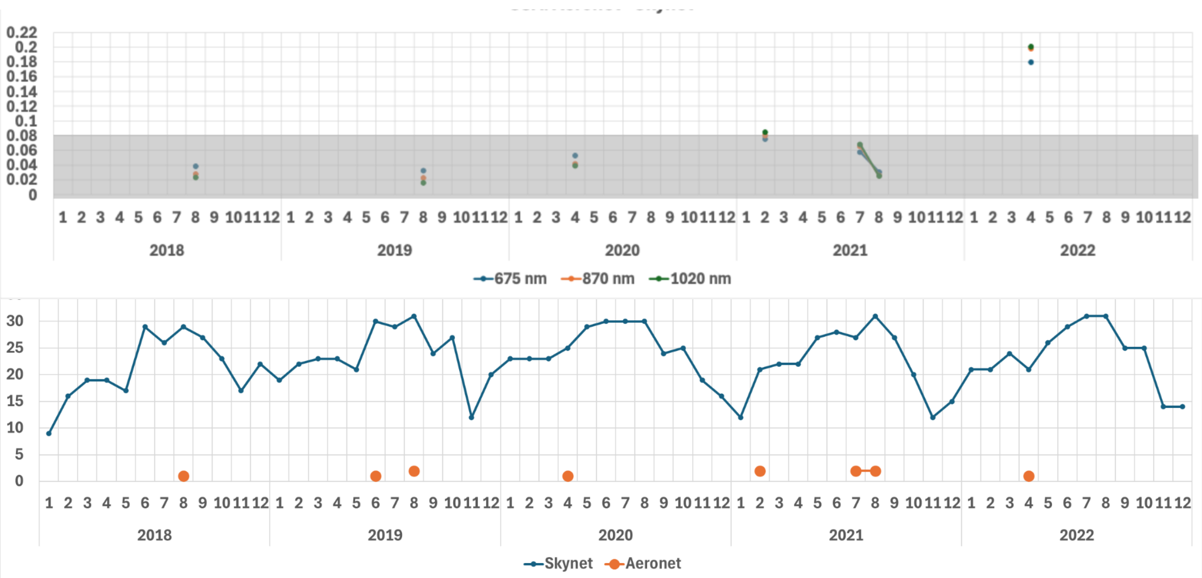

b)

Fig. 5.2.7 Monthly SSA differences between AERONET and SKYNET obtained by daily selection performed with criterion n1a (a) and criterion n2a (b), described in Tab 5.2.1. Gray box represents the maximum uncertainty from Kudo et al., 2021. The lowest panel depicts the number of points remaining after the selection criteria 2a for each month.

In conclusion, this work highlighted that in the urban site of Rome, SKYNET and AERONET AOD are absolutely comparable, because there isn't any anemological dependence in their differences, being their differences always within the AERONET uncertainties. Conversely, the monthly climatology is not always comparable and reasons should be investigated. For SSA, the differences are within the Skynet uncertainty, but an anemological analysis was not possible for the few number of AERONET points. This affects particularly the monthly climatology comparison where a more consistent AERONET number of points is needed.

References

Di Bernardino A. , A.M. Iannarelli, S. Casadio, C. Perrino, F. Barnaba, L. Tofful, M. Campanelli, L. Di Liberto, G. Mevi, A.M. Siani, M. Cacciani: Impact of synoptic meteorological conditions on air quality in three different case studies in Rome, Italy. Atmos. Pollut. Res., 12 (4) (2021), pp. 76-88, 10.1016/j.apr.2021.02.019

Di Bernardino, A.M. Iannarelli, S. Casadio, G. Pisacane, G. Mevi, M. Cacciani. Classification of synoptic and local-scale wind patterns using k-means clustering in a Tyrrhenian coastal area (Italy) Meteorol. Atmos. Phys., 134 (2) (2022), pp. 1-12, 10.1007/s00703-022-00871-z

Giles, D. M., Sinyuk, A., Sorokin, M. G., Schafer, J. S., Smirnov, A., Slutsker, I., Eck, T. F., Holben, B. N., Lewis, J. R., Campbell, J. R., Welton, E. J., Korkin, S. V., and Lyapustin, A. I.: Advancements in the Aerosol Robotic Network (AERONET) Version 3 database – automated near-real-time quality control algorithm with improved cloud screening for Sun photometer aerosol optical depth (AOD) measurements, Atmos. Meas. Tech., 12, 169–209, https://doi.org/10.5194/amt-12-169-2019, 2019.

Hartigan J. A. and Wong M. A., Algorithm AS 136: a k-means clustering algorithm, *Journal of the Royal Statistical Society. Series C (Applied Statistics)*. (1979) 28, 100–108

Iannarelli, A. M., and Coauthors, 2022: The Boundary Layer Air Quality-Analysis Using Network of Instruments (BAQUNIN) Supersite for Atmospheric Research and Satellite Validation over Rome Area. *Bull. Amer. Meteor. Soc.*, 103, E599–E618, https://doi.org/10.1175/BAMS-D-21-0099.1.

Kudo, R., Diémoz, H., Estellés, V., Campanelli, M., Momoi, M., Marenco, F., Ryder, C. L., Ijima, O., Uchiyama, A., Nakashima, K., Yamazaki, A., Nagasawa, R., Ohkawara, N., and Ishida, H.: Optimal use of the Prede POM sky radiometer for aerosol, water vapor, and ozone retrievals, Atmos. Meas. Tech., 14, 3395–3426, https://doi.org/10.5194/amt-14-3395-2021, 2021.

5.3 Long term trends of columnar aerosol properties at Valencia area (Eastern Spain) based on 15 and 20 years of SKYNET and AERONET measurements

Based on paper: "20 years of columnar aerosol properties at Valencia area (Eastern Spain) by ground-based sun-photometry", published at Atmospheric Research 300 (2024). Authors: Meritxell Garcia-Suñer, Violeta Matos, Gaurav Kumar, Víctor Estellés , María Pilar Utrillas.

This work is extracted from the recent publication from Garcia-Suñer et al., 2024, and it is focused on the study of atmospheric aerosols over two locations in Eastern Spain with different characteristics: Burjassot (which is situated in the metropolitan area of Valencia city, so it is considered an urban site) and Aras de los Olmos (which can be considered a remote rural station, since it is an unpopulated area). As both sites have Cimel CE-318 sun-photometers belonging to AERONET network, the retrieval products processed by them, which can be downloaded from their official website, were employed.

The results of this study are summarised hereafter. The analyses can be divided into three parts: first, a general research on the microphysical and optical properties of aerosols was carried out. Then, different aerosol classifications based on their properties were attempted: a distinction among aerosol types was performed based on the limits on AOD_{440} and $\alpha_{440-870}$ proposed in Filonchyk et al. (2021); then Gobbi's diagrams (Gobbi et al. 2007) were employed to identify particle growth and cloud contamination; and finally the origin of aerosols were analysed based on the origin of arriving air masses. The last part of the study was devoted to the examination of temporal trends for AOD_{440}, $\alpha_{440-870}$, columnar water vapor (w) and SSA_{440}. Two methodologies were employed. First, a preliminary analysis based on the linear regression method was carried out. Then, the Mann-Kendall test and Sen's slope (Mann 1945, Kendall 1975, Gilbert 1987; Sen, 1968) were applied in order to assess the significance of the trends and quantify them, respectively.

1.1 Climatological study of atmospheric aerosol properties.

In this section, the evolution of monthly means over the measurement years and the intra-annual variation for each magnitude were studied. The intra-annual variation is characterised by computing, for each month of the year, a set of statistical parameters that represent the behaviour for this month: mean, median, standard deviation and the 5th and 95th percentiles. These parameters were calculated based on monthly means for each year. In the cases of the asymmetry parameter g_{440}, the single scattering albedo SSA_{440} and the real and imaginary parts of the refractive index, m_{440} and $|k_{440}|$, respectively, their dependence with the wavelength was also analysed.

For Burjassot, measurements at Level 2.0 were available from January 2002 to March 2022. Data collected during the period ranging from January 2002 to March 2007 cannot be found in AERONET's website, since the instrument did not belong to the network at that time. Hence, these measurements were not processed based on AERONET's algorithm. Therefore, in order to justify their joint use, it was necessary to previously assess the agreement between both processing algorithms. To this end, a validation study was performed by employing data points corresponding to a period in 2007 from where data processed by both algorithms were available, obtaining that both data sets are in good agreement.

Regarding Aras de los Olmos, the available data set at Level 2.0 ranges from October 2015 to September 2020.

Figures 5.3.1a and 5.3.1b depict the monthly means over the years and the boxplots describing the intra-annual evolution of AOD_{440}, respectively, for Burjassot and Aras de los Olmos. It can be observed for both sites that the largest AOD_{440} values are found in summer months. This is related to the presence of both anthropogenic aerosols and mineral particles conveyed by dust intrusions from the North of Africa.

Although there are no important local emission sources near Aras de los Olmos (apart from dust outbreaks that are also common in summer at this location), higher AOD_{440} there may be favoured by particle stagnation, characteristic in summer due to stable atmospheric conditions. This, along with higher irradiances and humidity during this time of the year, could have led to secondary aerosol formation and hygroscopic particle growth.

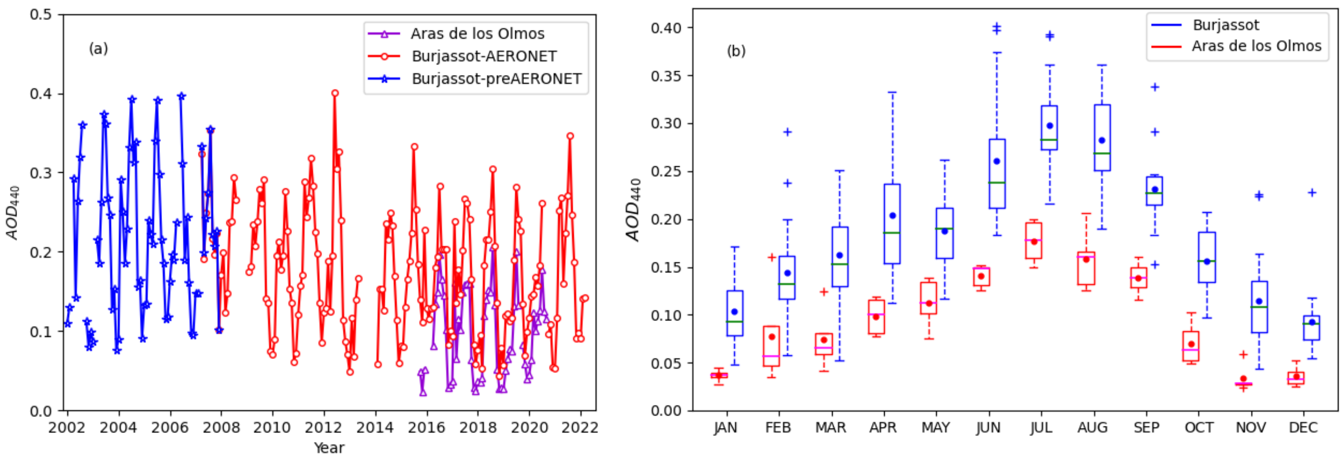

Figure 5.3.1: a) Monthly means of AOD_{440} in Aras de los Olmos (purple) and Burjassot (the blue line represents the 2002-2007 period, whereas the red line, data from 2007-2022). (b) Boxplots for AOD_{440} in Burjassot (blue) and Aras de los Olmos (red). Solid points indicate monthly means, and horizontal

lines monthly medians. The lower and upper limits of the boxes represent the first (U5) and third (U95) quartiles, respectively. Moreover, the lower and upper whiskers are determined by U5-1.5IQR and U95+1.5IQR, respectively, being IQR the interquartile range, i.e. the distance between the U95 and U5. The plus marks represent outliers.

The intra-annual evolution of columnar water vapor described the same pattern as the AOD_{440} (i.e. higher values in summer months and minimums in winter). This was an expected result, since the higher the irradiance, the higher the evaporation, resulting in an increase in the content of atmospheric water vapour.

Conversely, $\alpha_{440-870}$ did not describe any clear trend. This was attributed to the relevant presence of both fine and coarse particles in the atmospheric column, that are associated to large and small values of $\alpha_{440-870}$, respectively.

Taking into account the exceptional nature of the situation, a brief study was conducted focused on analysing the changes in AOD_{440} related to the COVID-19 lockdown period from March–June 2020. Hence, even though this topic requires further investigation, it was hypothesised that strong dust intrusions could have been responsible for the expected decrease in AOD_{440} in March not being observed. Conversely, a diminution in AOD_{440} could be noticed in June 2020 at both Burjassot and Aras de los Olmos sites.

The analysis of the inversion data products presented some difficulties, mainly related to the fact that the corresponding estimated uncertainties increase at small AOD (Sinyuk et al. 2020). Indeed, very little data were available at Level 2.0 for the SSA and the refractive index. Therefore, it was resolved to work with Level 1.5 retrievals, but taking into account that higher uncertainties would be associated with these magnitudes.

As for the volume size distribution, shown in Figure 5.3.2., clearly developed fine and coarse modes were identified at both locations, whereas the shape of these modes was less defined in winter months.

In the case of the asymmetry parameter g, its spectral dependence was characterised by a decrease at the smaller wavelengths followed by a slight increase for larger wavelengths, related to the presence of dust particles.

As for the SSA, it was larger in spring and summer, probably as a consequence of the scattering effect of dust particles. Its spectral dependence described a decrease in the range 670-1020 nm that can be related to the absorbing power of fine anthropogenic particles in this wavelength range.

The annual means and the corresponding standard deviation for the analysed magnitudes at both Burjassot and Aras de los Olmos have been summarised in Table 5.3.1.

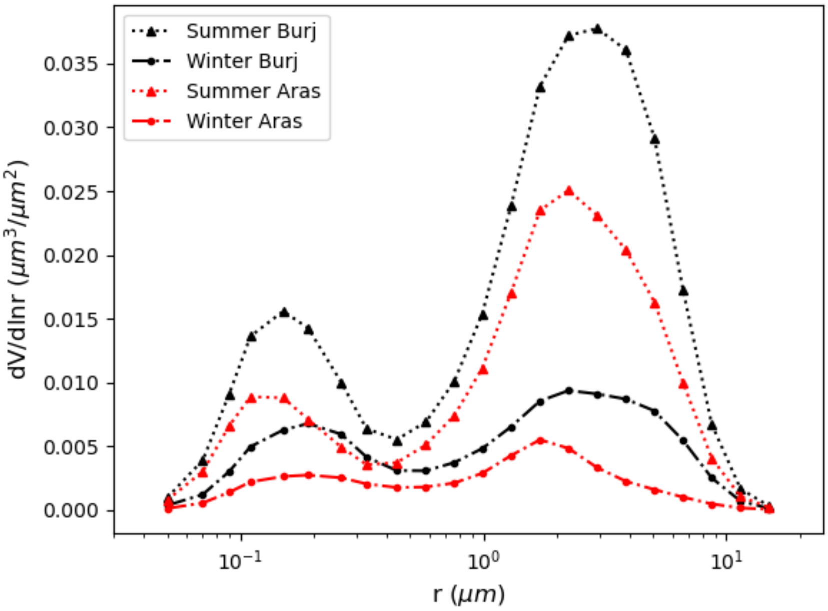

Figure 5.3.2: Aerosol volume size distribution in winter (semi-continuous lines with points) and summer (dotted curves with triangles), over Burjassot (black) and Aras de los Olmos (red).

Table 5.3.1: Mean values and the corresponding standard deviations for the parameters describing atmospheric aerosol properties analysed in this study.

	AOD_{440}	$\alpha_{440-870}$	**w (cm)**	SSA_{440}	g_{440}	m_{440}	$\|k_{440}\|$
Burjassot	0.19 ± 0.08	1.21 ± 0.16	1.87 ± 0.68	0.94 ± 0.03	0.700 ± 0.013	1.50 ± 0.03	0.007 ± 0.004
Aras de los Olmos	0.10 ± 0.02	1.18 ± 0.25	0.94 ± 0.10	0.95 ± 0.03	0.709 ± 0.016	1.49 ± 0.03	0.004 ± 0.004

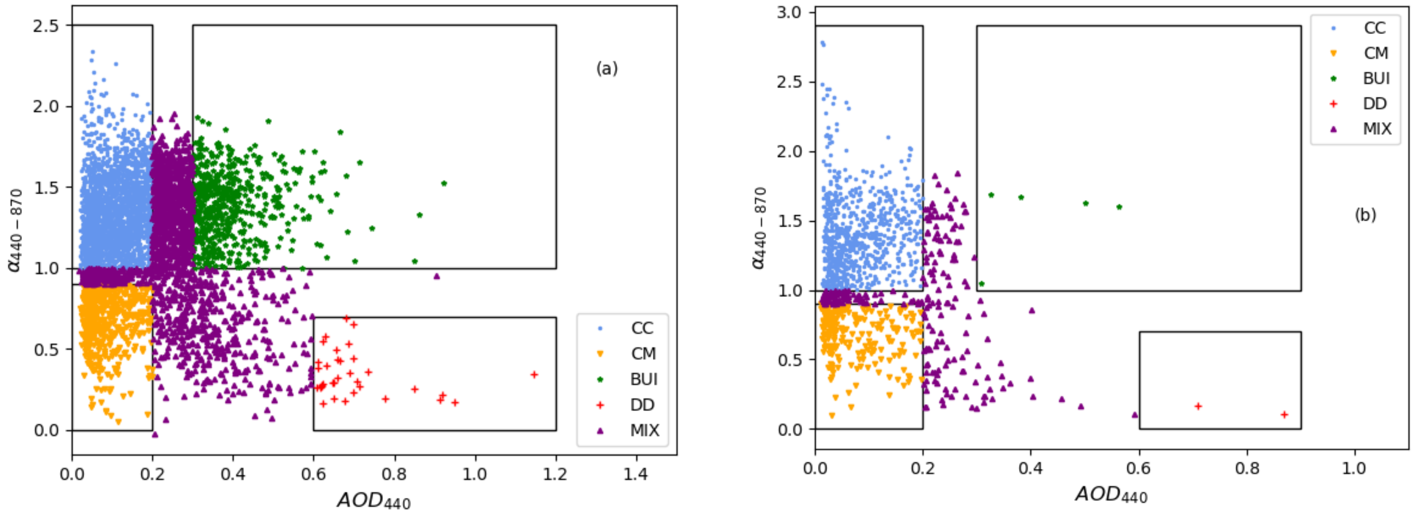

Figure 5.3.3: Distinction between aerosol types according to the values of AOD and α: continental clean (CC, blue points), clean marine (CM, yellow inverted triangles), biomass burning/urban/industrial (BUI, green stars), desert dust (DD, red pluses) and mixed aerosols (MIX, purple triangles); for (a) Burjassot and (b) Aras de los Olmos.

1.2. Aerosol classification.

- <u>Based on AOD_{440} and $\alpha_{440-870}$ limits:</u>

An aerosol classification based on imposed limits for AOD_{440} and $\alpha_{440-870}$ was carried out, following the works by several other authors (Sharma et al. 2014; Tiwari et al. 2016; Boiyo et al. 2019 and Filonchyk et al. 2021). Results are illustrated in Figures 5.3.3a and 5.3.3b for Burjassot and Aras de los Olmos, respectively. The most relevant conclusions are that continental clean aerosols constitute the most abundant aerosol type (~ 47% and ~ 63% in Burjassot and Aras de los Olmos, respectively), followed by mixed aerosols (~ 31% and ~ 18%). On the contrary, desert dust particles are the least abundant aerosol type. This is a reasonable result taking into account that dust intrusion outbreaks are only significant in spring and summer months, and they can arrive mixed with other types of aerosols.

- <u>Based on Gobbi's diagram:</u>

Figures 5.3.4a and 5.3.4b depict the Gobbi diagrams obtained for Burjassot and Aras de los Olmos, respectively. These plots permit identifying several characteristics about aerosols. Indeed, they can be used to differentiate between fine and coarse aerosols

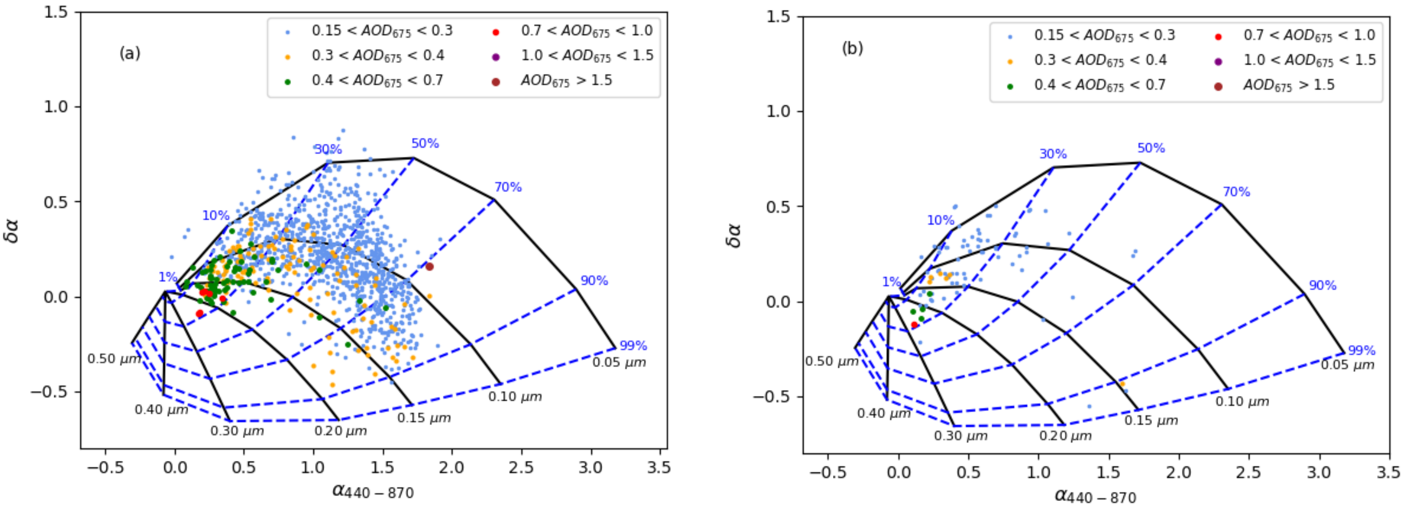

Figure 5.3.4: Gobbi diagram for Burjassot (a) and Aras de los Olmos (b). These are drawn by plotting AOD_{675} measurements in the AdA space (constituted by δα = α(440, 675) - α(675, 870) values as a function of α(440, 870)). Solid black lines indicate constant values of the fine modal radius, R_f, and dashed blue lines represent constant values of the ratios of the fine mode to total AOD at 675 nm, η.

and to identify cases of particle aggregation and hygroscopic growth. In addition, these plots can also be used in order to detect cloud contamination (Basart et al. 2009).

In Burjassot (Figure 5.3.4a), a clustered region of coarse mode particles, that could represent dust aerosols, was found around η < 30%, $\delta\alpha$ ~ 0 and α < 0.5. Conversely, the presence of fine particles could be noticed based on the area where η ~ 80%, $\delta\alpha$ < 0, α > 1 and 0.10 < R_f < 0.15 μm. From this region, a trace of particle growth perpendicularly to R_f could be observed, that was related either to hygroscopic growth or to the presence of fine mode particles. Finally, the region with η < 40%, $\delta\alpha$ > 0, α < 1 and R_f ~ 0.075 μm was suggested to represent a mixture of both fine and coarse mode aerosols.

In the case of Aras de los Olmos (Figure 5.3.4b), very few data points achieved to pass the AOD_{675} > 0.15 filter. Despite this, two clustered regions could be identified. It was reasoned that the one at η ~ 15%, $\delta\alpha$ ~ 0 and α < 0.5 is related to coarse particle, whereas the region at η < 30%, $\delta\alpha$ > 0, α < 0.5 and R_f ~ 0.075 μm, would indicate the mixing of coarse and fine mode aerosols.

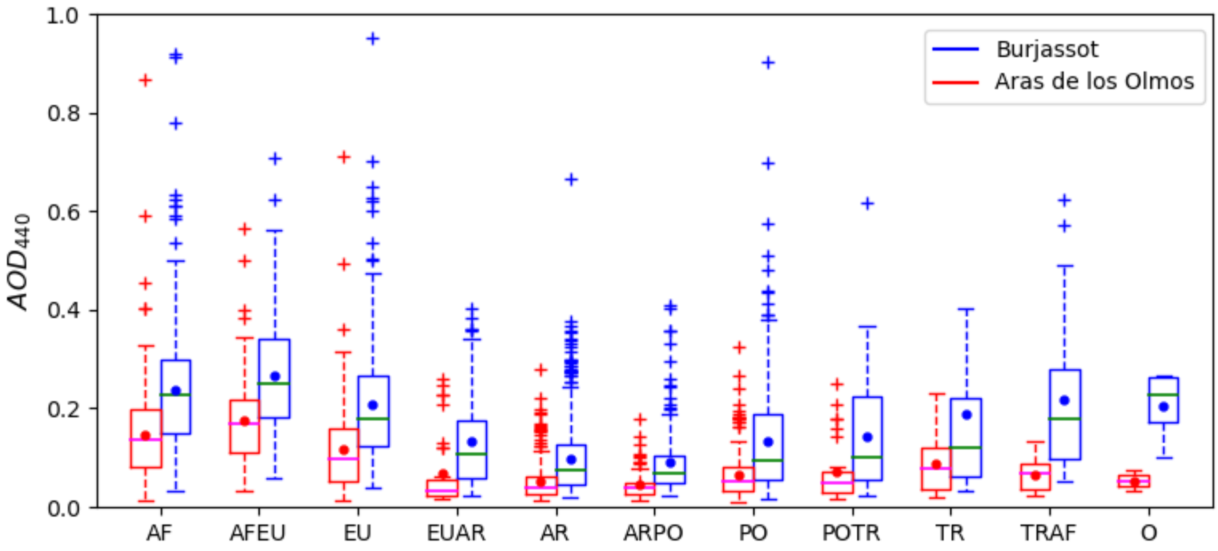

Figure 5.3.5: Air masses statistics AOD_{440} box diagram for Burjassot (blue) and Aras de los Olmos (red). AF: African; AFEU: African-European mix; EU: European; EUAR: European-Arctic mix; AR: Arctic; ARPO: Arctic-Polar mix; PO: Polar; POTR: Polar-Tropical mix; TR: Tropical; TRAF: Tropical-African mix; O: local stationary air mass.

- Air masses:

Figure 5.3.5 represents the AOD associated with the air masses that arrive at the measurement sites. It can be concluded that the cleanest air masses are the Arctic (AR), the Polar (PO), and their combinations. On the contrary, African (AF) and European (EU) air masses correspond to higher values of AOD_{440}. These results were not unexpected, since AF air masses usually transport dust aerosols, and EU air masses convey anthropogenic aerosols from the industrialised zones in Europe. On the other hand, Tropical (TR) masses were related to marine salt and dust particles. These air masses enhance the growth of hygroscopic particles due to the associated high humidity. As for the stationary air masses (O), the corresponding values of AOD_{440} were found to be higher in Burjassot than in Aras de los Olmos. Indeed, Burjassot is quite a more polluted area than Aras de los Olmos.

1.3. Time evolution.

Finally, the analysis of the time evolution revealed a statistically significant (> 80%) decreasing trend in AOD for most months. This result was in agreement with the preliminary study of AOD_{440} trends based on the linear regression method, that is shown in Figure 5.3.6. In this case, it can be noticed that the decrease is steeper in spring (-0.06 units/decade, with R^2 = 0.516) and summer (-0.04 units/decade, with R^2 = 0.375) than in autumn and winter.

On the contrary, no significant trends for *α*, *w* and SSA were obtained. Nevertheless, more years of data are needed, especially for Aras de los Olmos (where only 6 years of data are available). The problem lies in the fact that due to the higher uncertainties associated with the inversion products, very few data points remain after applying the data-quality assurance filters (Dubovik and King 2000, Dubovik et al. 2000, Holben et al. 2006). In the case of Burjassot, more than 20 years of AOD data are available, so this study could be regarded as a first approach to the site's climatology. Indeed, according to WMO (2017), the minimum time range necessary to study the climatology of a given site is 30 years of recorded measurements.

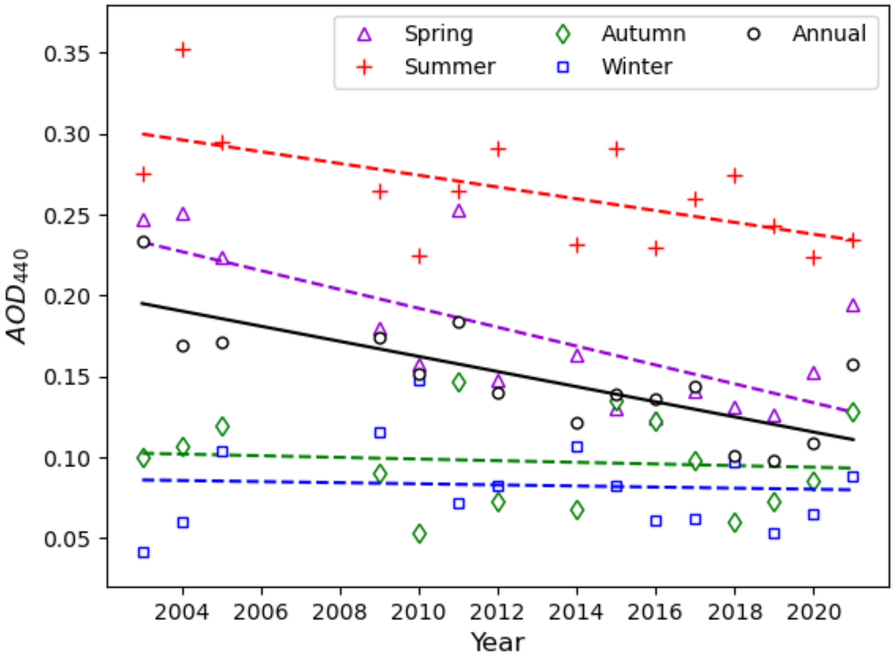

Figure 5.3.6: Study of AOD_{440} seasonal trends based on linear regressions, represented by dashed lines. Purple triangles indicate spring, red pluses summer, green diamonds autumn and blue squares winter medians. Black circles and lines represent the annual data points and trend, respectively.

References:

Basart, S., Pérez, C., Cuevas, E., Baldasano, J.M., Gobbi, G.P. Aerosol characterization in Northern Africa, Northeastern Atlantic, Mediterranean Basin and Middle East from direct-sun AERONET observations (2009). Atmos. Chem. Phys. 9 (21), 8265–8282. https://doi.org/10.5194/acp-9-8265-2009;

Boiyo, R., Kumar, K.R., Zhao, T., Guo, J. A 10-year record of aerosol optical properties and radiative forcing over three environmentally distinct AERONET sites in Kenya, East Africa (2019). J. Geophys. Res. Atmos. 124 (3), 1596–1617. https://doi.org/10.1029/2018JD029461

Dubovik, O., King, M.D. A flexible inversion algorithm for retrieval of aerosol optical properties from Sun and sky radiance measurements (2000). J. Geophys. Res. Atmos. 105 (D16), 20673–20696. https://doi.org/10.1029/2000JD900282.

Dubovik, O., Smirnov, A., Holben, B.N., King, M.D., Kaufman, Y.J., Eck, T.F., Slutsker, I. Accuracy assessments of aerosol optical properties retrieved from Aerosol Robotic Network (AERONET) Sun and sky radiance measurements (2000). J. Geophys. Res. Atmos. 105 (D8), 9791–9806. https://doi.org/10.1029/2000JD900040.

Filonchyk, M., Peterson, M., Yan, H., Yang, S., Chaikovsky, A. Columnar optical characteristics and radiative properties of aerosols of the AERONET site in Minsk, Belarus (2021). Atmos. Environ. 249, 118237. https://doi.org/10.1016/j.atmosenv.2021.118237. ISSN 1352-2310. URL. https://www.sciencedirect.com/science/article/pii/S1352231021000558

Gilbert, R.O. Statistical Methods for Environmental Pollution Monitoring (February 1987). Wiley. URL. https://www.osti.gov/biblio/7037501.

Gobbi, G.P., Kaufman, Y., Koren, I., Eck, T.. Classification of aerosol properties derived from AERONET direct sun data (2007). Atmos. Chem. Phys. 6, 01. https://doi.org/10.5

Holben, B., Eck, T., Slutsker, I., Smirnov, A., Sinyuk, A., Schafer, J., Giles, D., Dubovik, O. AERONET's version 2.0 quality assurance criteria (2006). Remote Sens. Atmosph. Clouds 6408, 12. https://doi.org/10.1117/12.706524

Kendall, M.G., 1975. Rank Correlation Methods. Griffin, London, https://academic.oup.com/ej/article-abstract/59/236/575/5260284

Mann, H.B., 1945. Nonparametric tests against trend. Econometrica 13, 245, https://www.jstor.org/stable/1907187

Sen, P.K. Estimates of the regression coefficient based on Kendall's Tau (1968). J. Am. Stat. Assoc. 63 (324), 1379–1389, https://doi.org/10.1080/01621459.1968.10480934

Sharma, M., Kaskaoutis, D.G., Singh, R.P., Singh, S.. Seasonal variability of atmospheric aerosol parameters over greater noida using ground sunphotometer observations (2014). Aerosol Air Qual. Res. 14 (3), 608–622. https://doi.org/10.4209/aaqr.2013.06.0219

Sinyuk , A., Holben , B. N., Eck , T. F., Giles, D. M., Slutsker , I., Korkin , S., Schafer, J. S., Smirnov , A., Sorokin , M., and Lyapustin , A . (2020): The AERONET Version 3 aerosol retrieval algorithm, associated uncertainties and comparisons to Version 2, Atmos. Meas. Tech., 13, 3375 3411. URL: https://amt.copernicus.org/articles/13/3375/2020/

Tiwari, S., Tiwari, S., Hopke, P., Attri, S.D., Soni, V., Singh, A. Variability in optical properties of atmospheric aerosols and their frequency distribution over a mega city "New Delhi" India (2016).

Environ. Sci. Pollut. Res. 23, 05. https://doi.org/10.1007/s11356-016-6060-3. URL. https://link.springer.com/article/10.1007/s11356-016-6060-3.

WMO. WMO Guidelines on the Calculation of Climate Normals. Technical report (2017). World Meteorological Organization. URL. https://library.wmo.int/doc_num.php?explnum_id=4166

5.4 Temporal trends of global UV solar irradiation over the last 20 years at Valencia (Spain)

Based on: "Temporal trends of global UV solar irradiation over the last 20 years in Valencia (eastern Spain)" presented at the European Meteorological Society Annual Meeting, Barcelona 8-12 September 2024. Authors: Violeta Matos, María José Marín, Jose Luis Gómez-Amo, Víctor Estellés, and María Pilar Utrillas.

The amount of solar ultraviolet radiation (UV) is a crucial parameter due to its relation to health effects, being associated with more than 90% of melanomas (Armstrong and Kricker, 1993). But it also has significant influence on ecosystems, environments and the Earth's atmospheric processes. In this work, we analyse the temporal variations exhibited by the daily values of UV erythemal irradiation (UVER) and the ultraviolet Index (UVI) at noon and the daily maximum, covering a 20 year (2003-2023) measurement period. The seasonal Mann-Kendall test was applied to identify the long-term trends and the Sen's slope estimator to quantify the annual variation rate. This analysis constitutes a preliminary step towards the combined long term analysis of different aerosol and radiation components in the Burjassot site at Valencia (Spain).

In this work we have used a 20-year database (2003–2023) of minute measurements of UVER (W/m2) with a Yankee UVB-1 radiometer (Yankee Environmental Systems, Turner Falls, MA, USA). The daily values UVER (KJ/m2) were obtained by daily integration of the 1-minute values. On the other hand, we have calculated the UV Index at noon and the daily maximum. UV Index was quantitatively obtained by multiplying the UVER value (expressed in W/m2) by 40. The seasonal behaviour of these parameters have been characterised previously by Marín et al. (2023).

Measurements of UVER were taken at Burjassot AtmoSpheric Station (BASS; 39.51N, 0.41W) with a broadband YES UVB-1 radiometer, located on the roof of the Faculty of Physics building (Figure 5.4.1). The measurement site is in the suburbs of Valencia, with a population of about 1 million in the metropolitan area. The site is mainly affected by anthropogenic aerosols originated by traffic and regional agricultural or forest fires, but also by natural aerosols from the Mediterranean Sea and Sahara desert.

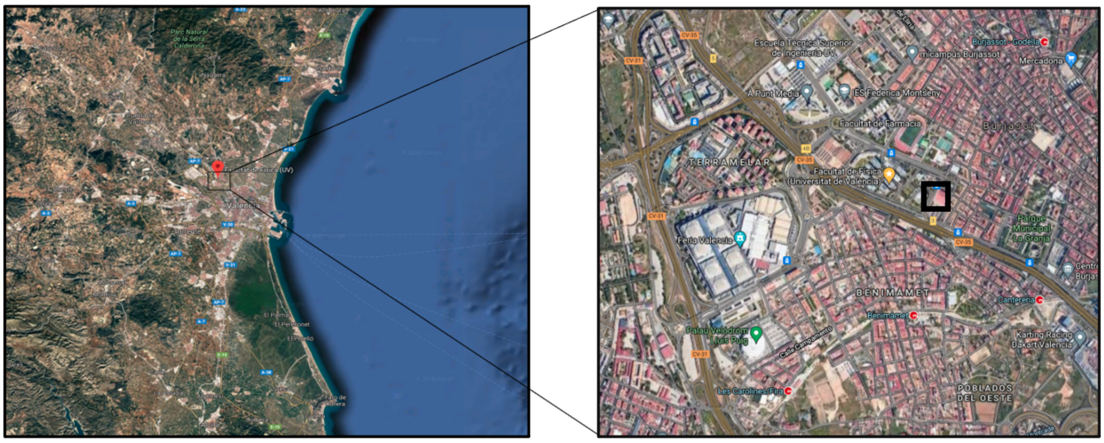

Figure 5.4.1. Location of the measurement site, in the East coast of Spain

Mann-Kendall (MK) test is one of the most widely applied non-parametric tests. This is a randomization vs. trend test, based on ranges. Due to the seasonality of the variables, the seasonal extension of the test was applied, using the monthly medians instead of annual values.

Table 5.4.1 shows the statistics of the seasonal MK test applied to monthly medians of UVER data. The UVER exhibits statistically significant increasing trends in most of the year, except in January, March and April. Generally, the significance of the test is higher in summer values, but it does not follow a regular annual distribution.

Table 5.4.1. Seasonal MK test statistics of UVER: number of monthly data (N), test statistics (Z), Sen's slope (Sen), Confidence Intervals of the slope at 90% confidence level (CI), interpretation of the trend (Trend): ↑ (increasing), ↓ (decreasing) and ⊗ (no trend); and the significance of the test (Sig.): α = 0.001 (****), 0.05 (***), 0.1 (**) and 0.2 (*).

Month	N	Z	Sen (kJ/m^2)/yr	CI (kJ/m^2)	Trend	Sig.
1	20	0.62	2.73	-	⊗	-
2	19	2.59	11.23	(4.23, 22.95)	↑	****
3	20	0.81	19.03	-	⊗	-
4	20	0.75	11.63	-	⊗	-
5	20	2.24	24.75	(5.68, 43.04)	↑	***
6	21	2.69	35.62	(16.04, 51.18)	↑	****
7	21	2.51	26.34	(12.76, 40.13)	↑	***
8	20	1.33	13.91	(-7.51, 34.71)	↑	*
9	21	1.66	17.64	(0.13, 30.75)	↑	**
10	21	1.36	15.13	(-1.13, 26.88)	↑	*
11	21	1.48	6.79	(-0.91, 15.87)	↑	*
12	21	2.57	7.13	(3.66, 12.72)	↑	***

Table 5.4.2. Seasonal MK test statistics of the UVI at noon: number of monthly data (N), test statistics (Z), Sen's slope (Sen), Confidence Intervals of the slope at 90% confidence level (CI), interpretation of the trend (Trend): ↑ (increasing), ↓ (decreasing) and ⊗ (no trend); and the significance of the test (Sig.): α = 0.001 (****), 0.05 (***), 0.1 (**) and 0.2 (*).

Month	N	Z	Sen (kJ/m²)/yr	CI (kJ/m²)	Trend	Sig.
1	20	0.03	0	-	⊗	-
2	19	2.40	0.03	(0.01, 0.05)	↑	***
3	20	1.27	0.05	-	⊗	-
4	20	0.81	0.02	-	⊗	-
5	20	3.43	0.08	(0.05, 0.09)	↑	****
6	21	3.93	0.08	(0.06, 0.09)	↑	****
7	21	2.36	0.05	(0.03, 0.08)	↑	***
8	20	1.69	0.03	(0.01, 0.06)	↑	**
9	21	2.54	0.05	(0.02, 0.07)	↑	***
10	21	0.91	0.02	-	⊗	-
11	21	1.12	0.02	-	⊗	-
12	21	2.44	0.02	(0.01, 0.03)	↑	***

On the other hand, Table 5.4.2 presents the MK statistics for the UVI at noon. This parameter shows increasing trends from April to September. Then, a homogeneous increasing trend is found for spring-summer period. Separately, UVI at noon also shows increasing trends in two winter months, February and December. Lastly, the temporal trends exhibited by the daily maximum UVI are shown in Table 5.4.3. For this case, the temporal trends are very similar to those observed for the UVER: the monthly medians increase in most of the year. Similar results have been reported by Marson et al. (2021) at United States, attributing the increased US melanoma incidence to ground-level UV radiation intensity trends; and by Fountoulakis et al. (2021) for several months (especially in April and summer months) in three sites of Italy.

Table 5.4.3. Seasonal MK test statistics of daily maximum UVI: number of monthly data (N), test statistics (Z), Sen's slope (Sen), Confidence Intervals of the slope at 90% confidence level (CI), interpretation of the trend (Trend): ↑ (increasing), ↓ (decreasing) and ⊗ (no trend); and the significance of the test (Sig.): α = 0.001 (****), 0.05 (***), 0.1 (**) and 0.2 (*).

Month	N	Z	Sen (kJ/m²)/yr	CI (kJ/m²)	Trend	Sig.
1	20	0.61	0	-	⊗	-
2	19	2.42	0.03	(0.02, 0.05)	↑	***
3	20	1.14	0.05	-	⊗	-
4	20	1.92	0.05	(0.02, 0.08)	↑	**
5	20	3.06	0.05	(0.04, 0.07)	↑	****
6	21	3.21	0.07	(0.04, 0.09)	↑	****
7	21	1.64	0.04	(0.01, 0.06)	↑	*

Conclusions

Characterization of temporal trends exhibited by the monthly global UV erythemal irradiance and the UV Index over the last 20 years shows that statistically significant increasing trends are inhibited in most of the year, excepting February and March. Therefore, the two variables have increased unequivocally over the last years.

Further analysis will make use of simultaneous atmospheric composition and meteorology datasets at Valencia site to clarify the main causes for such short and long-term trends, by the use of regression analysis. It will be studied whether factors such as the decrease in total aerosol extinction and absorbing species could influence the trends, apart from changes on total columnar ozone content.

References

Armstrong, B.K, and Kricker, A. How much melanoma is caused by sun exposure? *Melanoma Res*., 3, 395-40, 1993. DOI: 10.1097/00008390-199311000-00002.

Fountoulakis, I., Diémoz, H., Siani, A.M., di Sarra, A., Meloni, D., and Sferlazzo, D.M. Variability and trends in surface solar spectral ultraviolet irradiance in Italy: on the influence of geopotential height and lower-stratospheric ozone. *Atmos. Chem. Phys*., 21, 18689-18705, 2021. DOI: 10.5194/acp-21-18689-2021.

Marín, M.J., Estellés, V., Gómez-Amo, J.L., and Utrillas, M.P. Diffuse and Direct UV Index Experimental Values. *Atmosphere*, 14, 1221, 2023. DOI: 10.3390/atmos14081221.

Marson, J.W., Litchman, G.H., and Rigel, D.S. The magnitude of increased United States melanoma incidence attributable to ground-level ultraviolet radiation intensity trends. *J. Am. Ac. Dermatol*., 84, 6, 1734-1735, 2021. DOI: 10.1016/j.jaad.2020.08.100.